Reconciling the conflicting extent of overriding plate deformation before and during megathrust earthquakes in South America, Sunda, and northeast Japan

Mario D'Acquisto[1], Taco Broerse[1], Celine P. Marsman[1], Rob Govers[1]

[1]Tectonophysics Group, Department of Earth Sciences, Utrecht University, Netherlands

Corresponding author: Mario D'Acquisto (m.dacquisto@uu.nl)

Mario D'Acquisto (ORCID https://orcid.org/0000-0001-6321-1954)
Taco Broerse (ORCID https://orcid.org/0000-0002-3235-0844)
Celine P. Marsman (ORCID https://orcid.org/0000-0001-5691-6753)
Rob Govers (ORCID https://orcid.org/0000-0001-7148-8857)

Abstract

We aim to better understand the overriding plate deformation during the megathrust earthquake cycle. We estimate the spatial patterns of interseismic GNSS velocities in South America, Southeast Asia, and northern Japan and the associated uncertainties due to data gaps and velocity uncertainties. The interseismic velocities with respect to the overriding plate generally decrease with distance from the trench with a steep gradient up to a "hurdle", beyond which the gradient is distinctly lower and velocities are small. The hurdle is located 500–1000 km away from the trench, for the trench-perpendicular velocity component, and either at the same distance or closer for the trench-parallel component. Significant coseismic displacements were observed beyond these hurdles during the 2010 Maule, 2004 Sumatra-Andaman, and 2011 Tohoku earthquakes. We hypothesize that both the interseismic hurdle and the coseismic response result from a mechanical contrast in the overriding plate. We test our hypothesis using physically consistent, generic, three-dimensional finite element models of the earthquake cycle. Our models show a response similar to the interseismic and coseismic observations for a compliant near-trench overriding plate and an at least 5 times stiffer overriding plate beyond the contrast. The model results suggest that hurdles are more prominently expressed in observations near strongly locked megathrusts. Previous studies inferred major tectonic or geological boundaries and seismological contrasts located close to the observed hurdles in the studied overriding plates. The compliance contrast probably results from thermal, compositional and thickness contrasts and might cause the observed focusing of smaller-scale deformation like backthrusting.

Key words

Satellite geodesy, Subduction zone processes, Seismic cycle, Rheology: crust and lithosphere, Continental margins: convergent

1 Introduction

The great megathrust earthquakes of the previous decades happened after or during the deployment of continuous geodetic networks. After these earthquakes, many studies focused on constraining the coseismic fault slip by combining geodetic with seismological observations (e.g., Simons et al., 2011; Vigny et al., 2011). Postseismic processes like relocking, afterslip and viscoelastic flow started to become apparent in the geodetic measurements shortly after these events and continue today, spawning a rich variety of studies that cast new light on processes and rheological properties.

The first earthquake during the period of modern geodesy that revealed the widespread extent of coseismic deformation was the M_w 9.2 2004 Sumatra-Andaman earthquake. Remarkably, coseismic displacements were recorded at GNSS stations up to more than 3,000 km away from the megathrust (Vigny et al., 2005). Similarly, in 2010, GNSS stations far into the South American continent, which has a denser and more continuous distribution of GNSS sites than the surroundings of Sumatra, recorded displacement due to the M_w 8.8 Maule (Chile) earthquake as far as 1,700 km from the trench (Fig. 1; Pollitz et al., 2010). Likewise, Wang et al., 2011 observed significant coseismic static offsets up to 2,500 km away from the epicenter following the M_w 9.0 2011 Tohoku earthquake.

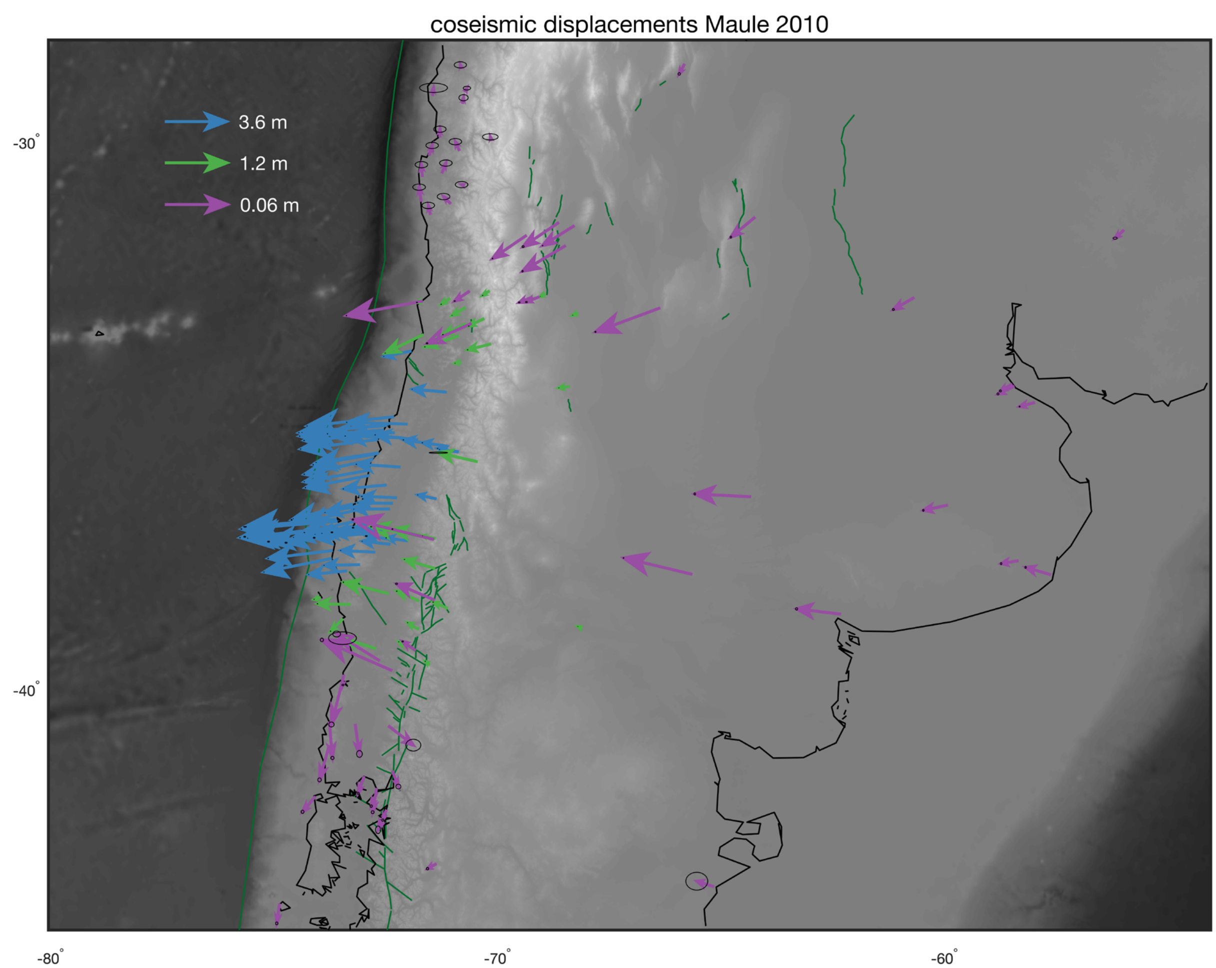

Figure 1. *Horizontal coseismic displacements observed at GNSS sites during the 2010 Maule earthquake. Observations are sourced from Delouis et al. (2010), Lin et al. (2013) Moreno et al. (2012) Tong et al. (2010) and Vigny et al. (2011).*

Strain that has accumulated during interseismic periods (mostly) recovers coseismically and postseismically, after all interseismic slip deficit has been released by large earthquakes. Studies that compare coseismic deformation to interseismic deformation have mostly focused on correlating the megathrust locking pattern to the coseismic slip pattern (e.g., Loveless and Meade, 2011; Moreno et al., 2010; Nocquet et al., 2017). Generally, observed interseismic velocities (relative to a stable overriding plate reference) are directed landward and decrease with distance from the trench. However, compared to the large extent of deformation due to the largest megathrust earthquakes, interseismic strain buildup seems to focus much closer to the margin of the overriding plate, within several hundreds of kilometers from the trench (e.g. Drewes and Heidbach, 2012; Kreemer et al., 2014; McKenzie and Furlong, 2021; Simons et al., 2007). In many locations where the full interseismic velocity profile with distance from the trench can be observed, a distinct break in the slope of the interseismic velocity gradient is observed; from a high velocity gradient near the trench to a small velocity gradient farther away (Brooks et al., 2003; Khazaradze & Klotz, 2003; Nocquet et al., 2014; McFarland et al., 2017). This observation fits well to the popular notion of separability of geodetic velocities due to either rotation of a rigid plate or to plate interactions in finite areas along plate margins (e.g. Altamimi et al., 2012; Kreemer et al., 2014).

The decrease in interseismic velocities, as a function of trench distance, can often be reproduced by locking of (a part of) the megathrust fault (modelled by backslip) in an elastic halfspace (Chlieh et al., 2008; Ruegg et al., 2009; Liu et al., 2010a; Métois et al., 2012). For parts of the South American plate, Norabuena et al. (1998) were the first to point out interseismic strain accumulation further inland that is higher than could be explained by megathrust locking alone. In the latter and in subsequent studies on the Central Andes (Norabuena et al., 1998; Bevis et al., 2001; Brooks et al., 2003; McFarland et al., 2017; Shi et al., 2020) a seismically active backthrust is adopted to explain the observed interseismic strain accumulation up to the backthrust, and a stable interior beyond that. In other cases, a somewhat looser definition of decoupling of the near-trench region from the rest of the plate is used by defining slivers that allow for a wholesale rotation with respect to the remainder of the overring plate (Métois et al., 2014; Nocquet et al., 2014). Both explanations rely on faults or shear zones that decouple the base of the lithosphere up to some depth, often interpreted as deep, active backthrusts of ~200 km wide (Weiss et al., 2016; McFarland et al., 2017).

Interpretations of interseismic strain accumulation are commonly based on fully elastic models. Overriding plate velocities decrease rapidly with distance from the trench in these models. Postseismic stress relaxation demonstrates however that the mantle wedge and sub-slab asthenosphere behave viscoelastically. Models with a viscoelastic upper mantle predict interseismic velocities that decrease more slowly with distance from the trench compared to elastic models (Wang et al., 2012). For increasingly higher asthenosphere viscosities model results converge to elastic-like behavior with strain accumulation that is more concentrated in the near-trench region (Trubienko et al., 2013; Li et al., 2015, 2020; Shi et al., 2020). Lower model viscosities result in interseismic velocities that remain significant up to thousands of kilometers into the overriding plate. To match the observed interseismic velocities with their viscoelastic models, Trubienko et al. (2013) and Li et al. (2015) use long-term (Maxwell) viscosities effectively in the range of $4.0–5.1\cdot10^{19}$ Pa·s when accounting for the use of plane-strain two-dimensional (2D) models on the relaxation timescale (Melosh & Raefsky, 1983). However, these viscosities are beyond the high end of the range of estimates of asthenospheric wedge viscosities ($4.0–10\cdot10^{18}$ Pa·s) from recent studies of postseismic viscous relaxation (see Section 4.9).

The South American margin has played a significant role in the development of ideas about interseismic strain accumulation because of the presence of a continuous region not interrupted by sea parallel to the margin. There are several other subduction zones with a continental overriding plate where the gradient of interseismic velocities is observable over a wide distance. Landward velocities in northern Honshu (Japan) and Hokkaido, recorded by GEONET before the 2003 Tokachi and 2011 Tohoku earthquakes (Sagiya et al., 2000a), show a fast decrease with trench distance. Likewise, interseismic velocities on Sumatra and Sunda before the 2004 earthquake show a decrease with distance from the trench (Prawirodirdjo et al., 1997; Simons et al., 2007), even though the trench-parallel motions are strongly affected by the Sumatran Fault (Genrich et al., 2000a). More significant difficulties in observing the interseismic velocity gradient arise in other subduction margins like Cascadia, where other tectonic processes overprint the interseismic locking signal, like the Mendocino Crustal Conveyor (Furlong & Govers, 1999) and the northward migration of the Sierra Nevada-Great Valley block (Williams et al., 2006). In southern Honshu and Shikoku strain rates due to convergence on the Japan trench and Nankai trench are superimposed, which makes it difficult to isolate the far-field interseismic velocity pattern. As discussed in Govers et al. (2018), continental Alaska shows continuing postseismic relaxation following the 1964 Prince William Sound earthquake. For these reasons, we focus on margins with only moderate tectonic complexity: South America, Sunda, and the Japan Trench.

In the present study we address the apparently contrasting geodetic observation that interseismic deformation of the overriding plate focusses within several hundreds of kilometers from the trench, whereas coseismic strain release extends over much greater distances. We observe a break in the slope of trench-parallel and trench-perpendicular velocity components as a function of trench distance, which we refer to as a hurdle. Long-lived subduction tectonically accretes blocks and rejuvenates the overriding plate, by an amount that is preconditioned by lithospheric compliance contrasts (Mouthereau et al., 2013; Pearson et al., 2013). These compliance contrasts remain visible today as significant contrasts in the effective elastic thickness of the lithosphere (Watts, 2015) that correlate with tectonic boundaries between blocks of vastly different ages (Watts et al., 1995; Stewart & Watts, 1997). Convergent deformation, including backthrusts, likely localizes at these naturally occurring contrasts. Here we consider the possibility that these lateral contrasts cause the hurdle-like behavior of the overring plate. Because of our context of the earthquake cycle we consider contrasts in elastic properties.

Our study consists of two main elements: mapping the patterns of interseismic velocities and secondly the interpretation of interseismic velocity gradients in terms of mechanical contrasts. We characterize the spatial pattern of horizontal interseismic surface motion along the South America Trench, the Sunda Trench and Japan Trench based on available observations (Section 2). Near-trench regions are typically (much) more densely instrumented than intermediate and far-field regions, and interseismic velocities of benchmarks have variable uncertainties. We pay particular attention to assessing how these factors propagate into uncertainties in the interpolated velocity fields. We estimate the approximate location of the hurdle, the dominant break in the slope of interseismic velocities, and discuss its significance.

To test our hypothesis that hurdle-like behavior is related to elastic contrasts in the overriding plate, we construct a three-dimensional viscoelastic numerical model (Section 3), analyze our model results and their robustness (Section 4). Next we discuss their significance and possible interpretations in the context of other proposed causes (Section 5). We conclude (Section 6) that a mechanical contrast in the overriding plate, with a more compliant near-trench region and a less compliant far-field region, is a likely candidate for explaining both the interseismic and coseismic observations in the three analyzed subduction zones.

2 Analysis of interseismic velocity observations

2.1 Data selection

We compile previously published horizontal velocities along three convergent margins with abundant interseismic GNSS observations: the Peru-Chile Trench (South America) (Kendrick et al., 2001; Klotz et al., 2001; Brooks et al., 2003, 2011; Chlieh et al., 2004; Gagnon et al., 2005a; Ruegg et al., 2009; Seemüller et al., 2010a; Drewes & Heidbach, 2012a; Métois et al., 2012, 2013, 2014; Alvarado et al., 2014a; Nocquet et al., 2014, 2014; Blewitt et al., 2016; Weiss et al., 2016; McFarland et al., 2017; Klein et al., 2018a), the Sunda Trench (Sumatra and Java, Indonesia) (Genrich et al., 2000a; Bock et al., 2003; Simons et al., 2007; Chlieh et al., 2008; Prawirodirdjo et al., 2010; Kreemer et al., 2014; Koulali et al., 2017), and the Japan Trench (Sagiya et al., 2000a; Apel et al., 2006a; Jin & Park, 2006a; Liu et al., 2010a; Nishimura, 2011a; Ohzono et al., 2011b; Shestakov et al., 2011a; Yoshioka, 2013; Kreemer et al., 2014; Freed et al., 2017). To prevent contamination by postseismic transient signals, we exclude velocities computed using postseismic observations in the trench-perpendicular sector of the overriding plate where significant ($M_w \geq 7.5$) earthquakes affected the observations (see Fig. 2). We use velocities expressed in the global reference frame ITRF (Altamimi et al., 2011). For the majority of our data sources we make use of the velocity tables from Kreemer et al. (2014), who have estimated a translation rate and rotation rate for each published set of velocities to express velocities in the same IGS08 reference frame (the IGS realization of ITRF). We feature velocities expressed in ITRF2005, ITRF2008, and ITRF2014; differences resulting from these different realizations are well below the 1 mm/yr level (Métivier et al., 2020). We also include velocities from Weiss et al. (2016), which are only provided in a self-determined, non-explicit South America reference frame. However, biases because of different reference frames are small: the mean difference in velocities between those of Weiss and the South America far-field velocities of Blewitt et al., 2016) is below 0.2 mm/yr.

Subsequently, we transform ITRF-expressed velocities to the overriding plate reference. For the sites in South America and Japan we apply the South America and Okhotsk Euler poles, respectively, of Kreemer et al. (2014). For Sumatra we make use of the Sunda Euler pole of Simons et al. (2007), who identify Sundaland as a coherent block moving independently of the South China block farther north. More information about data sources is available in Text S1 and Tables S1, S2 and S3. The resultant interseismic velocities, described in a consistent reference frame throughout each studied region, show a clear contrast between high near-trench velocities and a stable interior (Fig. 1).

2.2 Velocity decomposition into trench-perpendicular and -parallel components

Along many subduction zones, the deformation due to oblique interplate convergence is partitioned into distinct trench-perpendicular and trench-parallel fault slip and strain (Fitch, 1972; McCaffrey, 1992, 1996). Strain partitioning not only implies that margin-parallel shear is accommodated on different faults than the convergent motion, but also that margin-parallel and margin-perpendicular interseismic deformation may be distributed differently in the overriding plate. Using straight lines from the trench to identify margin-perpendicular and -parallel directions at each observation point can lead to sharp contrasts in each direction between nearby observation locations, depending on the trench geometry, and produces ambiguity in the case of a convex plate margin. Therefore, we define a conformal (i.e., angle-preserving) projection, specifically a Schwarz-Christoffel map (Driscoll, 2002), to identify trench-perpendicular and -parallel directions throughout each of the three study areas. This leads to a coordinate system that is locally trench-perpendicular at the trench, and that smoothly grades into a regional/plate-wide trench-perpendicular orientation with increasing distance from the trench. The derivatives in transformed coordinates express the angles between the local east and north-directions and the local trench-perpendicular and -parallel directions, allowing us to compute the relevant, orthogonal, trench-perpendicular and trench-parallel components of each velocity vector at any location, see Fig. 1.

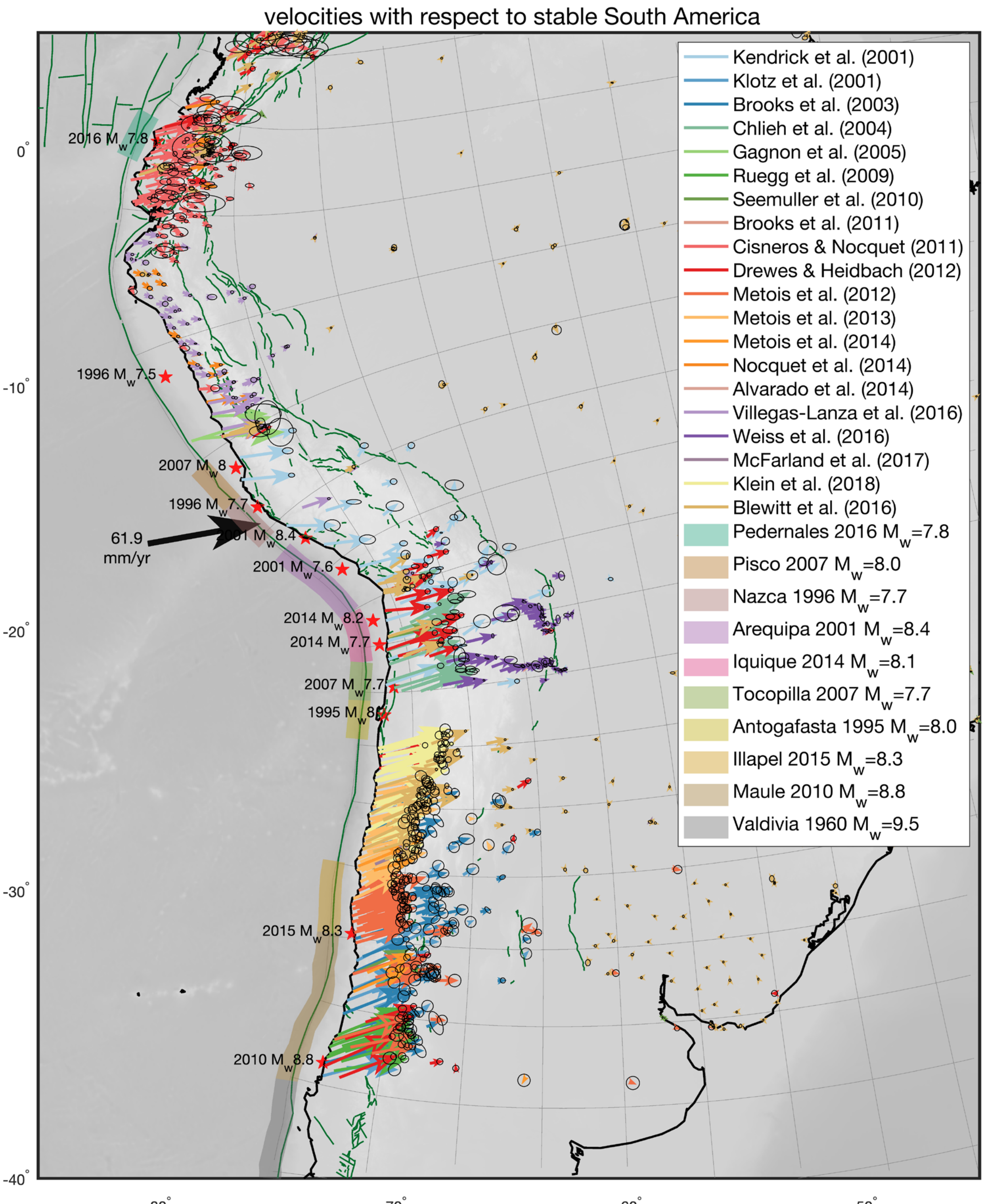
velocities with respect to stable South America
Kendrick et al. (2001)
Klotz et al. (2001)
Brooks et al. (2003)
Chlieh et al. (2004)
Gagnon et al. (2005)
Ruegg et al. (2009)
Seemuller et al. (2010)
Brooks et al. (2011)
Cisneros & Nocquet (2011)
Drewes & Heidbach (2012)
Metois et al. (2012)
Metois et al. (2013)
Metois et al. (2014)
Nocquet et al. (2014)
Alvarado et al. (2014)
Villegas-Lanza et al. (2016)
Weiss et al. (2016)
McFarland et al. (2017)
Klein et al. (2018)
Blewitt et al. (2016)
Pedernales 2016 M_w=7.8
Pisco 2007 M_w=8.0
Nazca 1996 M_w=7.7
Arequipa 2001 M_w=8.4
Iquique 2014 M_w=8.1
Tocopilla 2007 M_w=7.7
Antogafasta 1995 M_w=8.0
Illapel 2015 M_w=8.3
Maule 2010 M_w=8.8
Valdivia 1960 M_w=9.5
2016 M_w 7.8
1996 M_w 7.5
2007 M_w 8
1996 M_w 7.7
2001 M_w 8.4
2001 M_w 7.6
61.9
mm/yr
2014 M_w 8.2
2014 M_w 7.7
2007 M_w 7.7
1995 M_w 8
2015 M_w 8.3
2010 M_w 8.8
0°
-10°
-20°
-30°
-40°
-80°
-70°
-60°
-50°

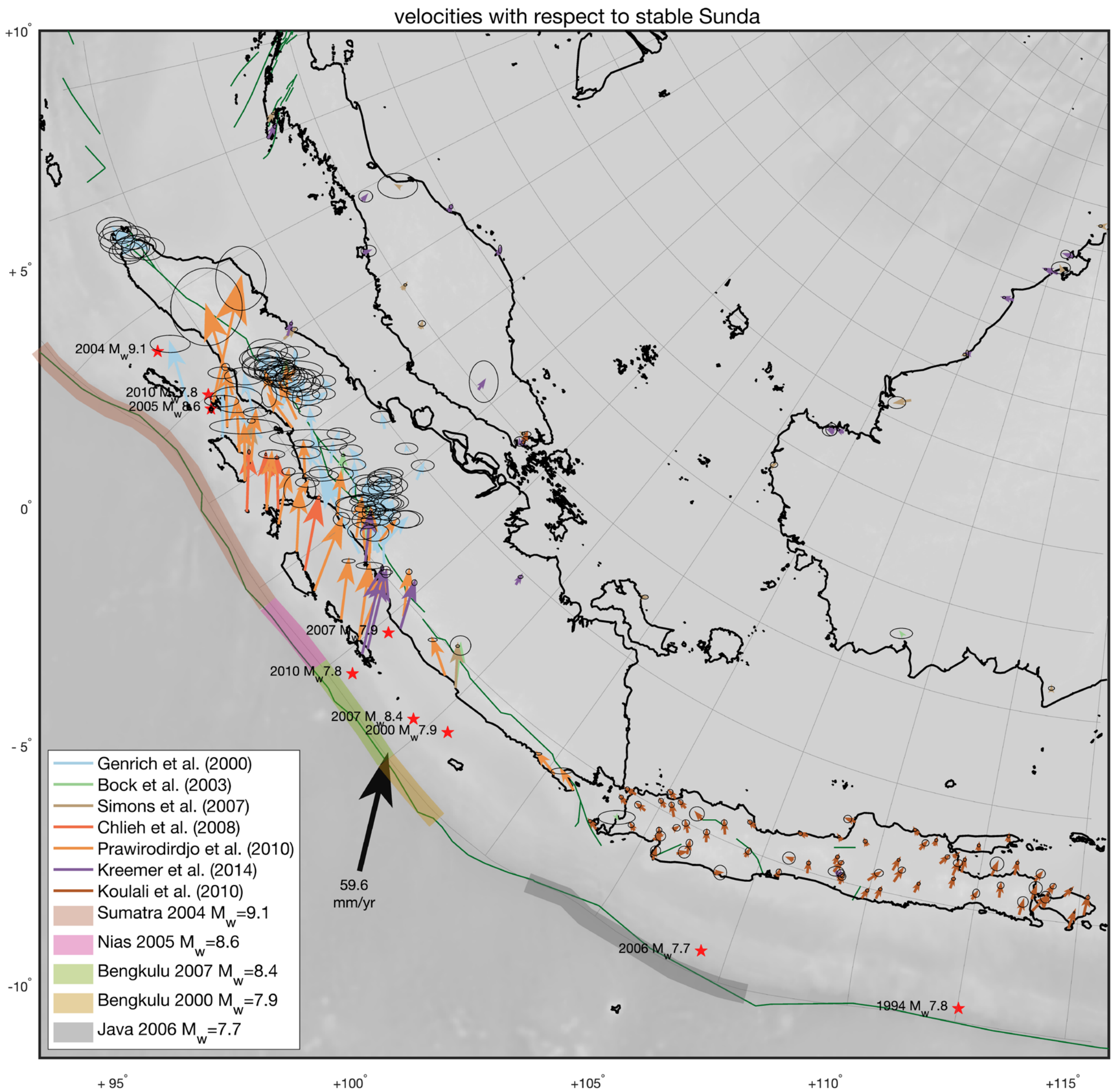
velocities with respect to stable Sunda
+10°
+ 5°
0°
- 5°
-10°
+ 95°
+100°
+105°
+110°
+115°
2004 Mw 9.1
2010 Mw 7.8
2005 Mw 8.6
2007 Mw 7.9
2010 Mw 7.8
2007 Mw 8.4
2000 Mw 7.9
2006 Mw 7.7
1994 Mw 7.8
59.6
mm/yr
Genrich et al. (2000)
Bock et al. (2003)
Simons et al. (2007)
Chlieh et al. (2008)
Prawirodirdjo et al. (2010)
Kreemer et al. (2014)
Koulali et al. (2010)
Sumatra 2004 Mw=9.1
Nias 2005 Mw=8.6
Bengkulu 2007 Mw=8.4
Bengkulu 2000 Mw=7.9
Java 2006 Mw=7.7

199

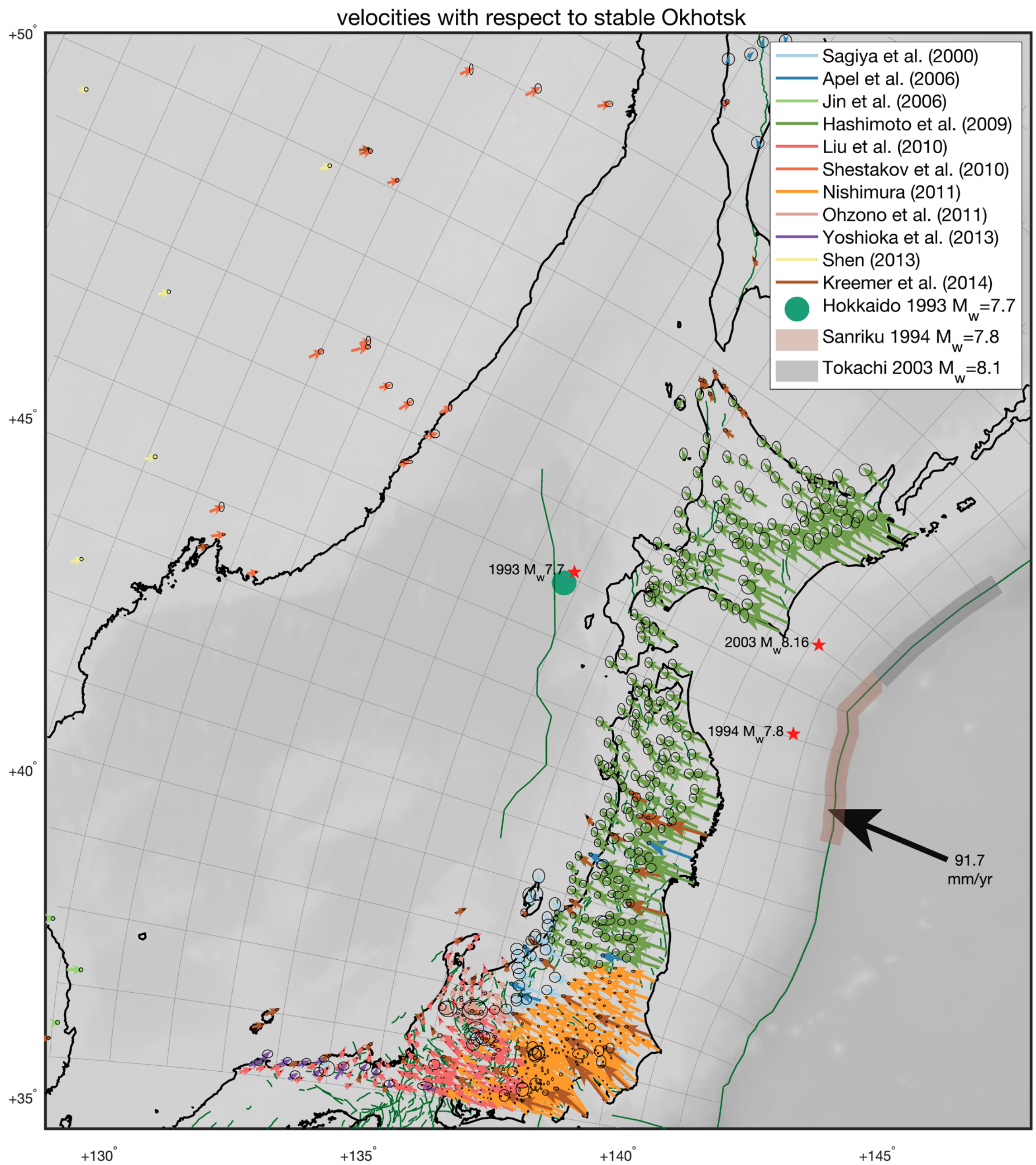

Figure 2. *Published observed velocities, topography, active faults (green), earthquakes with M_w>7.5 during the time of observation (red stars), and trench-perpendicular/parallel orientations (gray grid) in each of the three studied subduction zones. Interplate convergence velocities for the Peru-Chile Trench, Sunda Trench and Japan Trench (pre-2011 Tohoku earthquake) are taken from Kreemer et al. (2014), Simons et al. (2007), and Kreemer et al. (2014) (Okhotsk plate), respectively. To exclude the effect of postseismic relaxation, in each segment of the subduction zone that hosted a significant ($M_w \geq 7.5$) earthquake, we discard all velocities in the area that*

has been affected by coseismic displacements and postseismic transients (areas indicated by colored sections of the trench). For this reason we have a gap in the data distribution at ~23° S *as we exclude all data after the 1995 Antofagasta earthquake. Similarly, we exclude all data in southwest Hokkaido, where velocities increase towards the west, likely due to postseismic relaxation after the 1993 Hokkaido Nansei earthquake* (Ueda et al., 2003)*. We set data exclusion zones stretching from the indicated parts of the trench to a distance from the trench (600 km and 1500 km for events larger than* $M_w \geq 8.7$*), which we apply to data collected after the events.*

2.3 Interpolation of the decomposed velocity fields

Most geodetic studies of GNSS interseismic deformation have focused on deforming zones close to the margin for the purpose of estimating the megathrust locking pattern. In most regions, the geodetic benchmarks are unevenly distributed with much denser networks in near-trench areas than farther away from the trench, and low density in the far-field plate interior that is used as the stable reference. For a continuous view on the velocity field and estimation of the location of velocity gradient discontinuities, we separately interpolate the observed trench-perpendicular and -parallel velocity components. We account for the propagation of observational uncertainty and for the potential velocity variability in between observed sites in the following way. Using ordinary kriging (Wackernagel, 2003), a weighted mean method that relies on the statistics of the observed data, we interpolate the velocities and estimate uncertainties. The mean, variance and correlation of the velocity field are spatially heterogeneous and thus we define natural neighborhoods to construct correlograms that describe the local variability of the velocity field (Broerse et al., in prep.; Fouedjio and Séguret, 2016; Machuca-Mory and Deutsch, 2013). Further technical details are in Text S1 and Figs. S1–S12. in the Supporting Information.

The uncertainties we compute for our interpolated velocity field reflect both the uncertainty of velocity observations (i.e., data uncertainty) and the expected variance of the velocity field between observation points. Figs. S10–S12 show that uncertainties of the interpolated velocity field are small in regions with little variability in observed velocities, but increase substantially with distance from observation points in regions where observed velocities vary significantly in between observation points.

2.4 Estimation of the hurdle location

The hurdle constitutes the main discontinuity in velocity gradients separating the interseismically deforming margin from the stable interior. We use the continuous interpolated velocity fields we compute, together with their robust uncertainty estimates, to estimate the hurdle location all along the trench. First, we take trench-perpendicular profiles, which are equidistant at the trench, through the 2D interpolated field, 277 in total for South America, 64 for Sunda, and 51 for Japan. We determine trench-perpendicular and -parallel components along a profile, and their uncertainties, by applying bilinear interpolation of the field that we estimated in the kriging procedure. Subsequently, we fit a piece-wise continuous function consisting of two linear segments to the velocity transect as function of distance along the profile. We use weighted non-linear least squares with a Trust Region algorithm and, applying inverse variances from the kriging as weights. The junction between the two segments, which is a free parameter in the fitting process, represents the hurdle distance. We propagate the velocity uncertainties to the uncertainties of the hurdle location, approximated by linearization of the non-linear problem, for more details see the Supplement. Figs. 3–5a,b show our estimated hurdle locations for each of the subduction zones. Figs. 3–5c depict hurdle locations along selected trench-perpendicular profiles, next to interpolated velocities, their uncertainties, and GNSS observations.

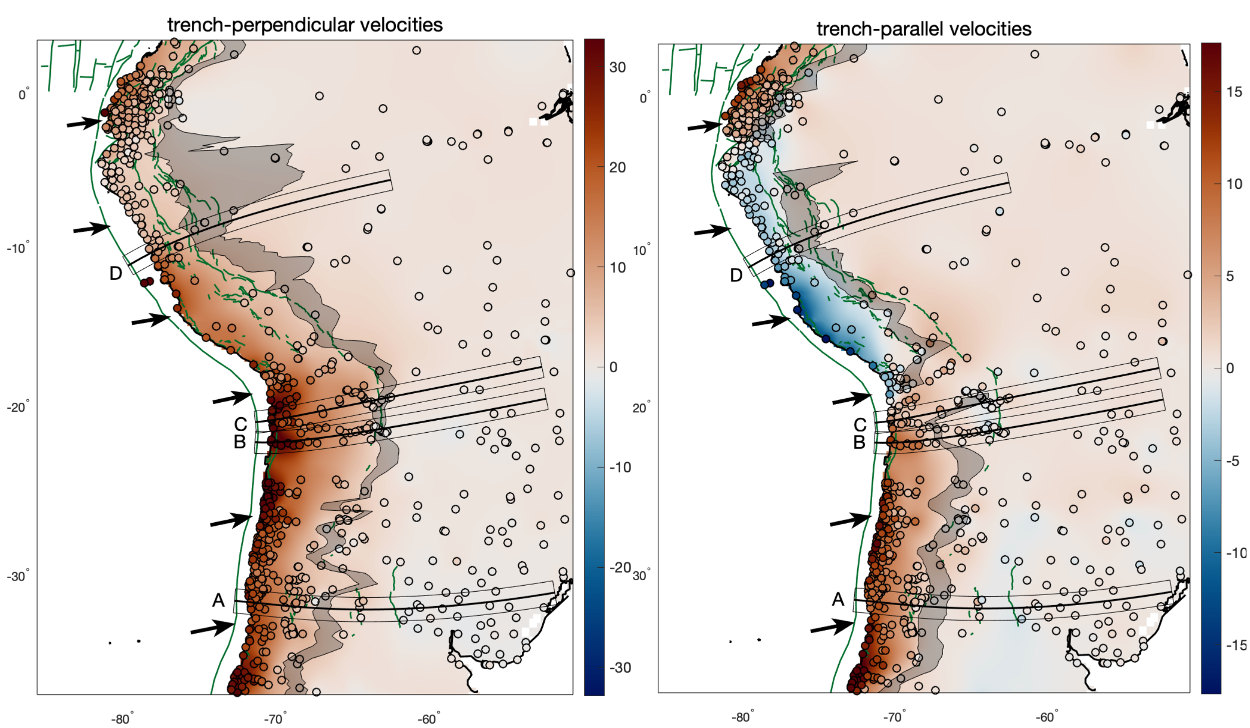

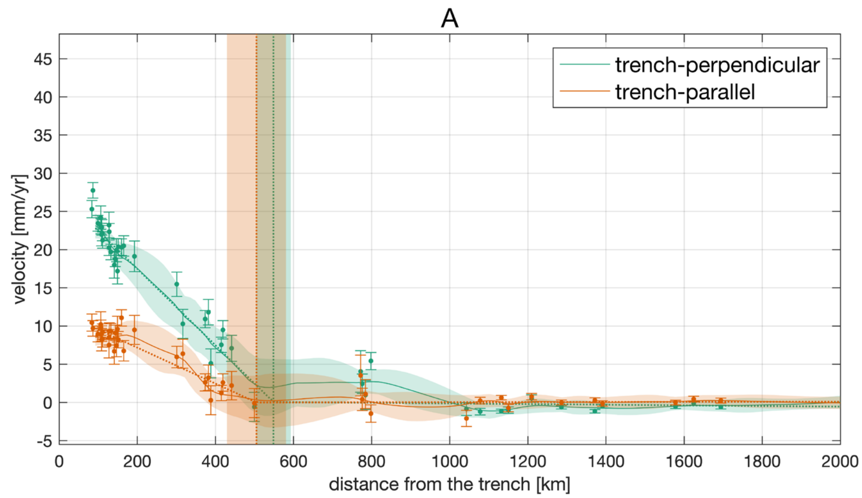
A
trench-perpendicular
trench-parallel
velocity [mm/yr]
distance from the trench [km]

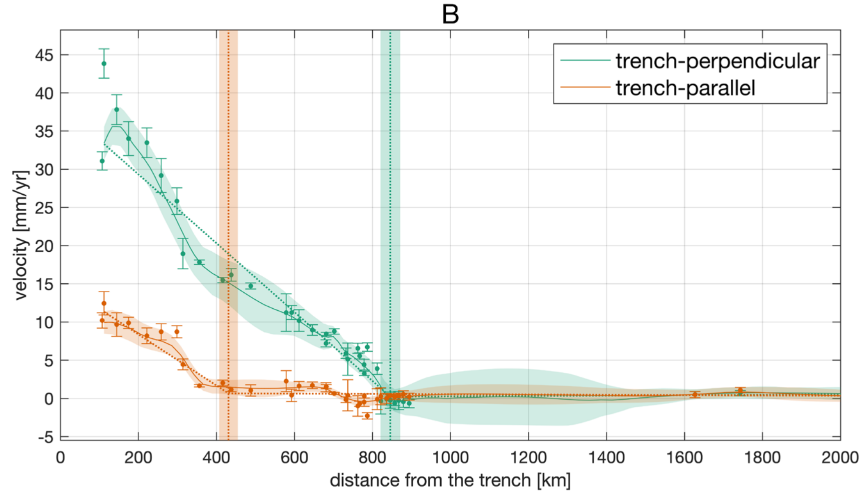
B
trench-perpendicular
trench-parallel
velocity [mm/yr]
distance from the trench [km]

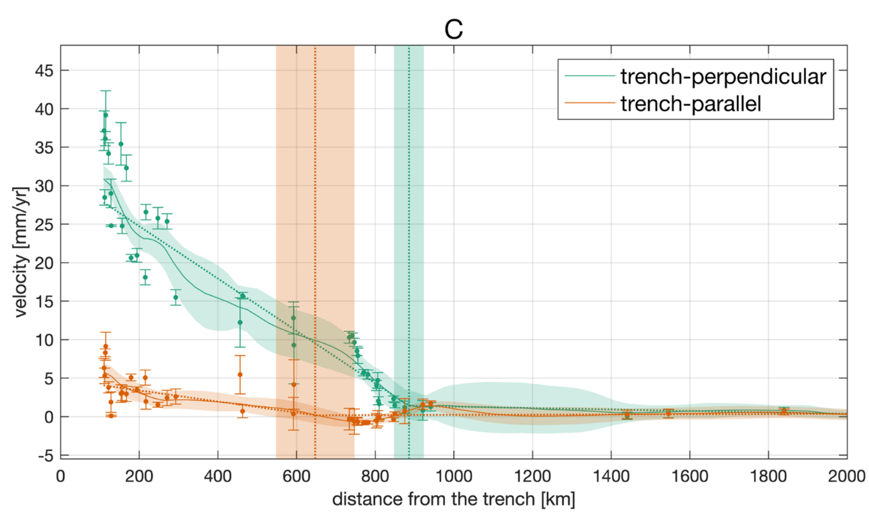
C
trench-perpendicular
trench-parallel
velocity [mm/yr]
distance from the trench [km]

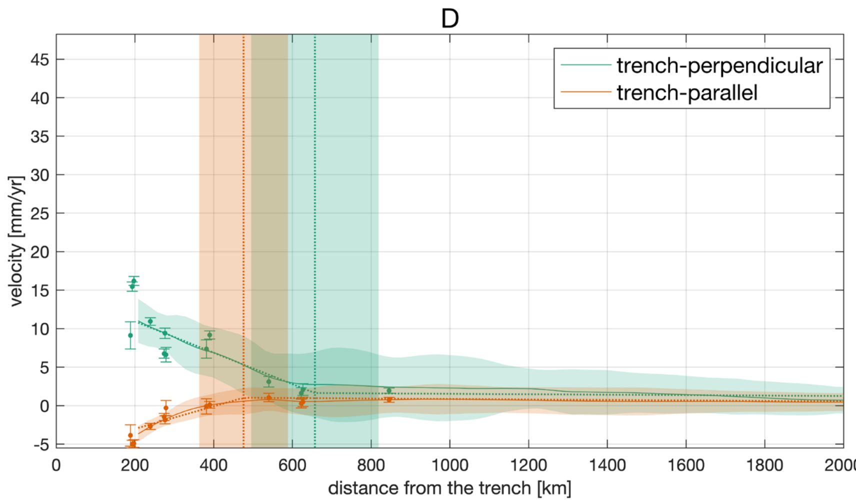

Figure 3. *The maps show interpolated interseismic velocity components (colors) for South America and the 95% confidence interval of the location of the hurdle in gray. Active faults from GEM (Styron & Pagani, 2020) are shown in green; on the left, we show trench-perpendicular velocities (positive landward), and on the right trench-parallel velocities (positive left-lateral). In both panels, circles represent benchmarks, and their fill color is the observed interseismic velocity. Arrows show the convergence direction along the Peru-Chile Trench* (Kreemer et al., 2014). *Coastlines are drawn in black. Locations of trench-perpendicular swath profile lines A, B and C are shown on the maps by the thick line surrounded by the thinner lines showing the swath width. The panels below show the velocity profiles along A, B and C, including both interpolated velocity components (continuous lines) with 1 standard deviation uncertainty (transparent bands), and the velocity components at GNSS stations within the swath (dots) with 1 standard deviation error bars. Note that the interpolated velocities are based on all GNSS velocity estimates, and not only those shown in the swath for reference. Dotted green and orange lines depict the piece-wise linear fit. Vertical dotted lines and bands outline estimated hurdle distances with 95% confidence intervals.*

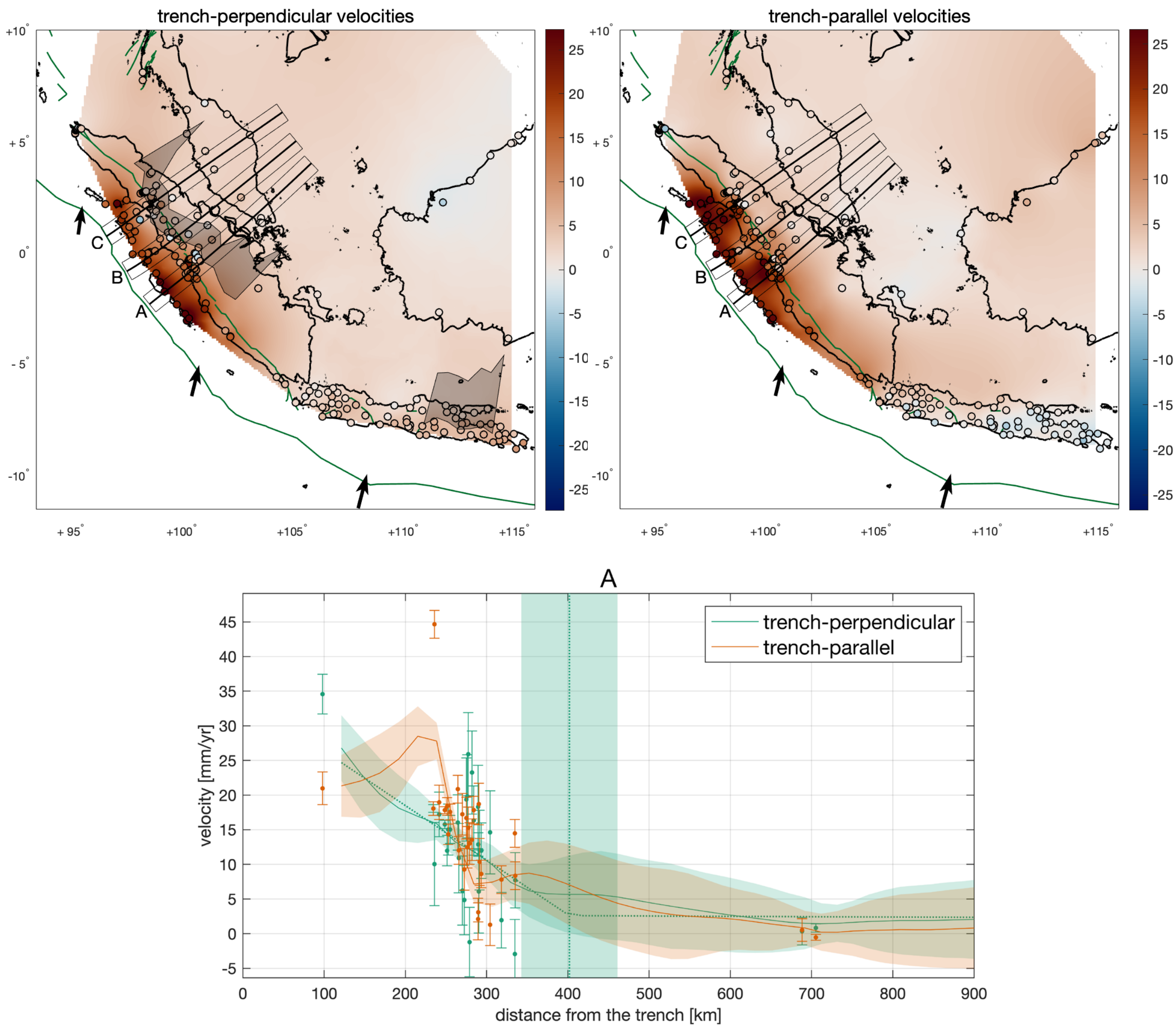
trench-perpendicular velocities
trench-parallel velocities
A
B
C
+10°
+5°
0°
-5°
-10°
+95°
+100°
+105°
+110°
+115°
25
20
15
10
5
0
-5
-10
-15
-20
-25
A
trench-perpendicular
trench-parallel
velocity [mm/yr]
distance from the trench [km]

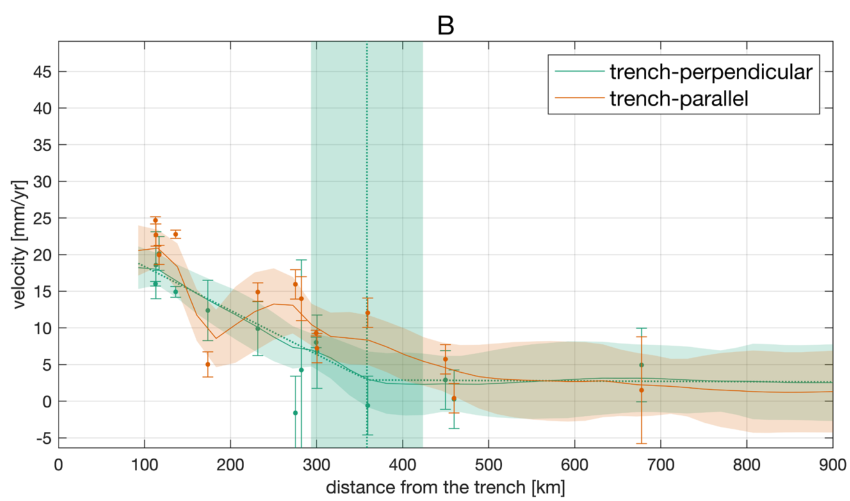
B
trench-perpendicular
trench-parallel
velocity [mm/yr]
distance from the trench [km]

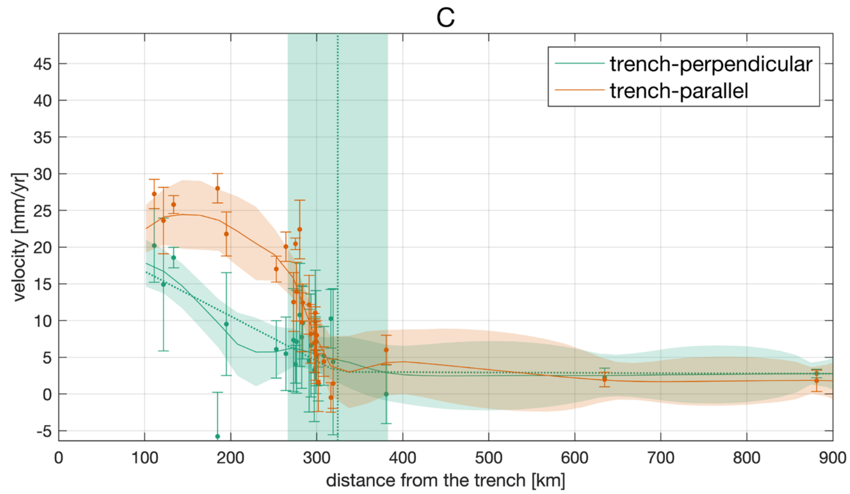

Figure 4. *The maps show interpolated trench-perpendicular (left panel, positive landward) and trench-parallel velocity fields (right panel, positive left-lateral) and 95% confidence-interval location of the hurdle (a,b), together with active faults in green from GEM (Styron & Pagani, 2020). Coastlines are in black and arrows show the interplate convergence direction between the Sunda and Australian plates* (Simons et al., 2007)*. Below, we show selected trench-perpendicular velocity profiles (A–C) in Indonesia and Malaysia, on the landward side of the Sunda Trench, along the profile lines shown and labeled in the maps. The velocity profiles show both interpolated velocity components with 1 standard deviation uncertainty (transparent bands), and the velocity components at GNSS stations within the swath with 1 standard deviation error bars. Note that the interpolated velocities are based on all GNSS velocity estimates, and not only those shown in the swath for reference. Dotted green and orange lines depict the piece-wise linear fit. Vertical dotted lines and bands outline estimated hurdle distances with 95% confidence intervals.*

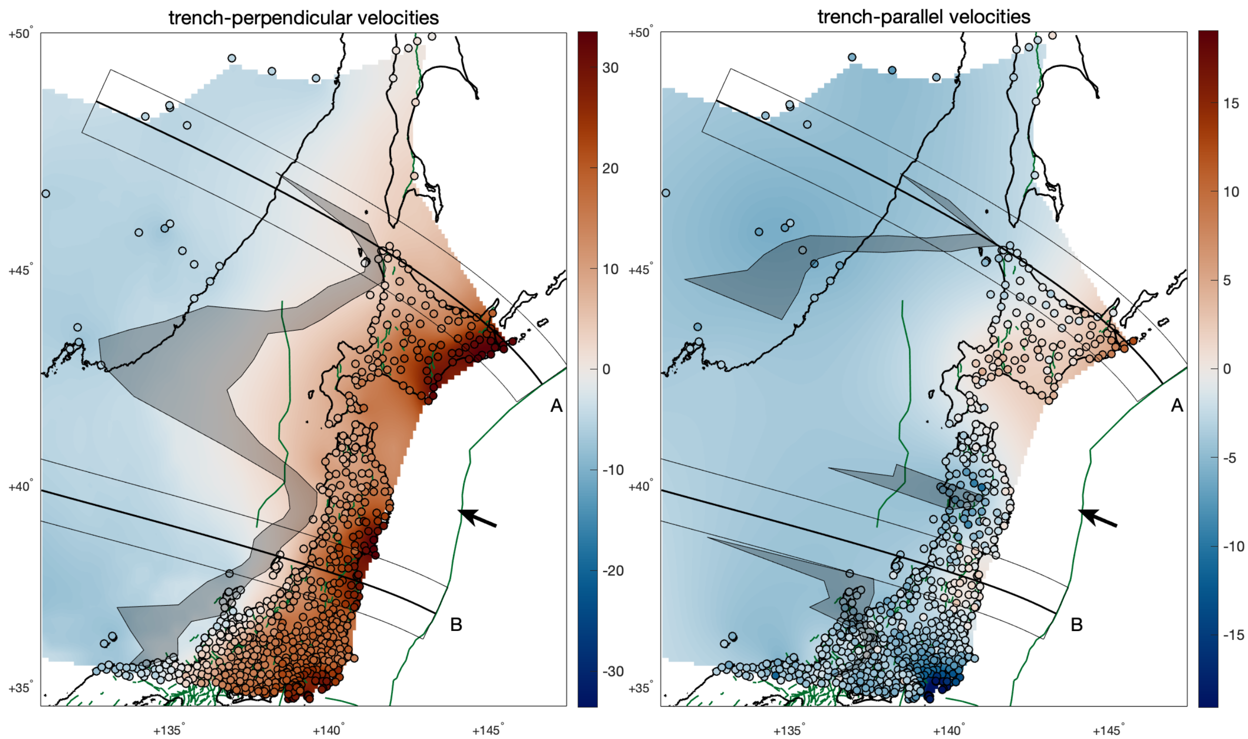
trench-perpendicular velocities
trench-parallel velocities
A
B
+50°
+45°
+40°
+35°
+135°
+140°
+145°
30
20
10
0
-10
-20
-30
15
10
5
0
-5
-10
-15

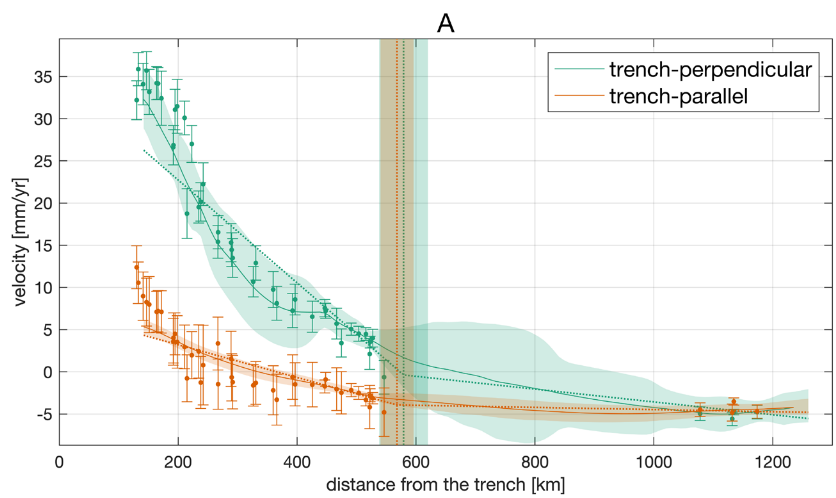
A
trench-perpendicular
trench-parallel
velocity [mm/yr]
distance from the trench [km]
35
30
25
20
15
10
5
0
-5
0
200
400
600
800
1000
1200

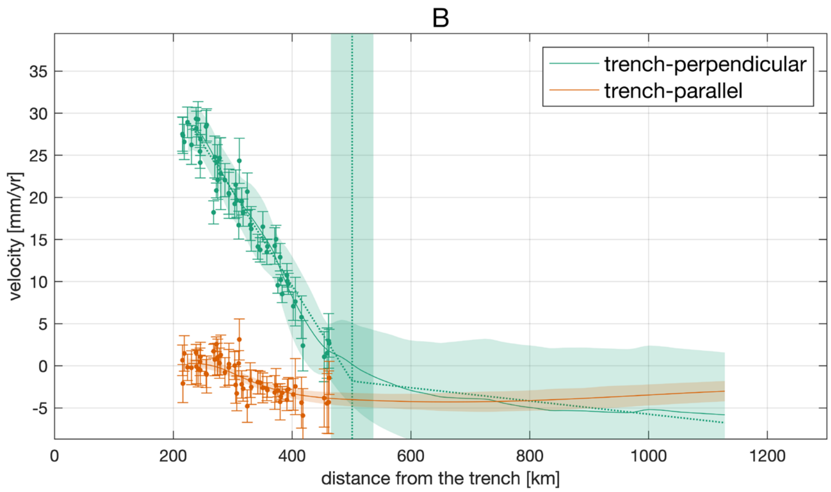

Figure 5. *The maps show interpolated trench-perpendicular (positive landward) and trench-parallel (positive left-lateral) velocity fields with 95% confidence-interval location of the hurdle, together with active faults in green from GEM (Styron & Pagani, 2020). Coastlines are in black and arrows show the interplate convergence direction between the Pacific plate and Okhotsk* (Kreemer et al., 2014)*. Below, we show selected trench-perpendicular profiles, in Honshu and Hokkaido, on the landward side of the Japan Trench, along the profile lines traced in the maps. The velocity profiles show both interpolated velocity components with 1 standard deviation uncertainty (transparent bands), and the velocity components at GNSS stations within the swath with 1 standard deviation error bars. Note that the interpolated velocities are based on all GNSS velocity estimates, and not only those shown in the swath for reference. Dotted green and orange lines depict the piece-wise linear fit. Vertical dotted lines and bands outline estimated hurdle distances with 95% confidence intervals.*

2.5 Data analysis results

Both velocity components decrease quickly with distance from the trench up to a hurdle, behind which a far-field region starts with low velocity amplitudes and gradients (see Figs. 3–5). The hurdle location can be constrained best when both the velocity uncertainties are small and there exists a strong discontinuity between the near-field and far-field velocity gradient. Trench-perpendicular velocities in particular show a steep near-trench decrease, except above sections of the megathrust that are not locked over an extensive trench-parallel distance. Such unlocked portions of the subduction interface are characterized by low interseismic velocity magnitudes (e.g., Matsu'ura & Sato, 1989), e.g., in northern Peru (4–9° S latitude) (Herman & Govers, 2020; Nocquet et al., 2014) and Java (Koulali et al., 2017). Trench-parallel velocities show a more complex behavior, particularly where the convergence obliquity changes direction (inverting the sign of near-trench trench-parallel velocities) and forearc slivers have been suggested to exist (Nocquet et al., 2014; Métois et al., 2016; Herman & Govers, 2020). Nevertheless, trench-parallel velocities also indicate a hurdle, beyond which amplitudes are near-zero and the slope is very shallow.

In South America, we can identify the trench-perpendicular hurdle as the location of the transition between rapid near-trench decay and the other, shallower slope in the far-field. The hurdle is located at distances from the trench varying between 400 and 1000 km approximately, including the lower and upper bounds of the confidence interval, except for the section of subduction zone with poorly coupled megathrust in Northern Peru (4–9° S) (Fig. 2). The hurdle location generally largely tracks the eastern margin of the Andean orogen (Fig. 5a). Only landward of the poorly locked megathrust of Norther Peru, the trench-perpendicular gradient in the velocity component is low and the hurdle location is identified at distances beyond 1000 km from the trench, although the uncertainty on the location is very large and the nearest location within the confidence interval still tracks the eastern boundary of the orogen. The hurdle lies a few tens of km landward of the backthrust in south-central Peru (10–13° S). Further to the south, in Bolivia (14–21°), it precisely follows the backthrust at the base of the mountain range. In northernmost Argentina there is no clear, active backthrust, but the hurdle traces the border of the Puna plateau. Immediately to the south, around 30° S, the hurdle is located in the middle of the Sierras Pampeanas.

For South America, the hurdle for trench-parallel velocities is located between 220 and 800 km from the trench, excluding the poorly coupled megathrust section. It is always closer to the trench or coincident with the trench-perpendicular hurdle. Velocities beyond the hurdle are near, but not always exactly, zero: the trench-perpendicular component is between -1 and 4 mm/yr in amplitude, while the trench-parallel component is between -1 and 2 mm/yr.

Observations of interseismic velocities in Sumatra are sparser than in South America. In the southeast of the island, observations are far apart. Both velocity components are small and have low gradients, including the near-trench region (Fig. 3). This reflects the low coupling in that region (Chlieh et al., 2008) and does not allow us to locate any hurdle. In central Sumatra, where near-trench velocities indicate strong interplate coupling and data coverage is much denser, we observe a hurdle in the trench-perpendicular component, bounding the zone of near-uniform low velocities in the interior of Sunda (Simons et al., 2007). The hurdle runs through the middle of the island, roughly coinciding with the southwestern edge of the Sibumasu terrane reported by Hutchison (2014) and Metcalfe (2011) (Fig. 5b), as well as with the northeastern boundary of the zone of active orogenic deformation as indicated by Hall and Sevastjanova (2012). Trench-parallel velocities do not show a uniform decrease with distance from the trench, but rather are near-uniform on the Indian Ocean coast of central Sumatra and in the smaller offshore islands, and have a steep gradient over the Sumatran Fault (Prawirodirdjo et al., 1997; Genrich et al., 2000a), behind which the parallel velocities quickly converge to zero. We thus do not perform our parallel hurdle location estimation in Sumatra. In Java, both velocity components are low throughout, indicating low megathrust coupling (Koulali et al., 2017), and the lack of observations to the northeast of the island, in the Java Sea, prevents us from confidently identifying a hurdle.

Along the Japan trench, trench-perpendicular velocities decrease with distance from the trench following a steep trend with constant or gently decreasing slope in the vast majority of Hokkaido (trench locations north of 42° N) and most of central-northern Honshu (south of 40° N). The resulting hurdle location measures ~450–600 km from the trench (Fig. 4). It broadly follows the eastern margin of the floor of the Sea of Japan, a few tens of km offshore except for where it touches the northernmost tip of Hokkaido (Fig. 5c). On the other side of the Sea of Japan, observations in Manchuria and South Korea constrain the velocity field at intermediate to far distances, helping locate the hurdle. The trench-perpendicular and trench-parallel velocities in those sites are uniformly negative (around 5 mm/yr, both trenchward and right-lateral, respectively), indicating limited transpressional motion between Manchuria, inferred to be part of the Amurian plate, and Hokkaido, generally considered part of the Okhotsk plate (Weaver et al., 2003; Petit & Fournier, 2005). Off the shore of south-central Honshu (south of 40° latitude), observations in the intermediate- and far-field are not available and the velocity filed in the Sea of Japan is interpolated relying on observations far to the northwest. Nevertheless, the steep, near-linear decrease of trench-perpendicular velocities in the densely instrumented island convincingly supports the existence of a hurdle. The Okhotsk-Amurian plate boundary, inferred here to cross Honshu by Bird (2003), does not affect the slope of trench-perpendicular velocities with distance from the trench. In northernmost Honshu and the southwestern most tip of Hokkaido (for trench locations between 40° and 42° N), both the trench-perpendicular velocities and their trench-perpendicular gradients are lower, possibly reflecting lower interplate coupling than in laterally adjacent portions of the megathrust (Suwa et al., 2006; Hashimoto et al., 2009) or incomplete postseismic transient corrections for the 1994 Sanriku earthquake (Loveless & Meade, 2010).

Trench-parallel velocities in northern Honshu are low, while the uncertainties of available interseismic velocities are relatively high. This, combined with the narrow width where observations are possible, makes it difficult to identify a hurdle in the trench-parallel component. Additionally, trench-parallel velocities vary in sign across the study area. This clearly reflects in part small changes in the strike of the trench which, combined with the overall head-on character of the convergence, changes the sign of the trench-parallel component of the velocity of the downgoing (Pacific) plate with respect to the overriding (Okhotsk) one. Nevertheless, trench-parallel velocities seem to decrease to uniform values (-5–-6 mm/yr, reflecting the northwards motion of the Amurian plate with respect to the Okhotsk) within ~600 km of the trench in northern Hokkaido and within ~300–400 km in northern Honshu.

We also performed the data analysis for Japan expressing all velocities with respect to the Amurian plate, rather than the Okhotsk plate, see Fig. S13. This uniformly increases trench-perpendicular velocities by ~6 mm/yr and the trench-parallel by ~5 mm/yr. Trench-perpendicular velocities are thus entirely positive (landward), while trench-parallel velocities are largely positive (dextral). Only a few areas with negative trench-parallel velocities remain: some isolated near-zero negative patches and the southeastern corner of Honshu, next to the Sagami Trough and the assumed southern boundary of the Okhotsk plate. The estimated trench-perpendicular hurdle location is completely unaffected by shifting the reference frame from the Okhotsk- to the Amurian plate. Conversely, the change in reference frame allows for determination of the hurdle in the trench-parallel component within our uncertainty threshold, by reducing the far-field variability in amplitudes and thus the interpolation uncertainty. The resulting hurdle is located ~260–450 km from the trench off the coast of Honshu and 560–870 km from the trench off Hokkaido, with the largest values for profiles in southern Hokkaido, where the velocities are uniformly higher on the island than in the mainland.

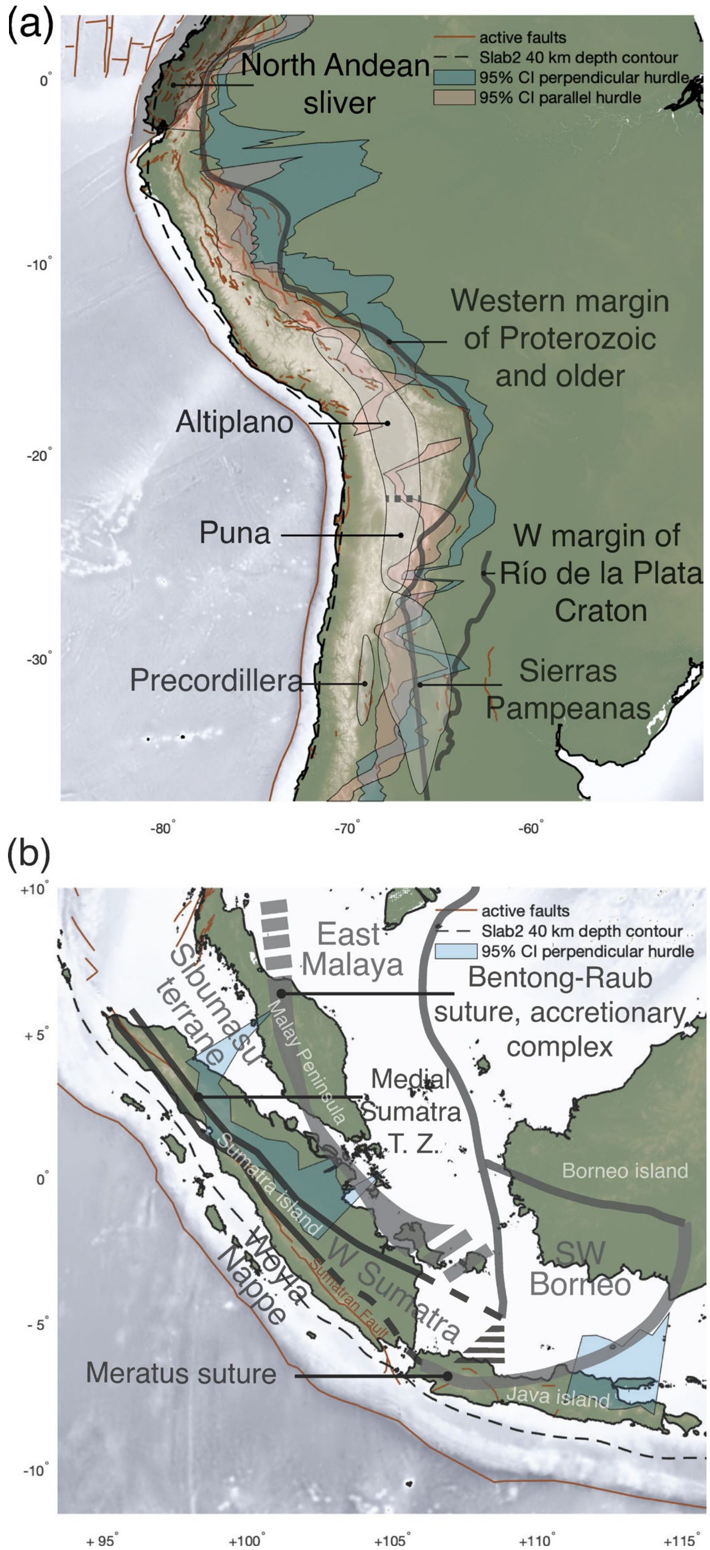
(a)
active faults
Slab2 40 km depth contour
95% CI perpendicular hurdle
95% CI parallel hurdle
North Andean sliver
Western margin of Proterozoic and older
Altiplano
Puna
W margin of Río de la Plata Craton
Precordillera
Sierras Pampeanas
0°
-10°
-20°
-30°
-80°
-70°
-60°
(b)
active faults
Slab2 40 km depth contour
95% CI perpendicular hurdle
East Malaya
Bentong-Raub suture, accretionary complex
Sibumasu terrane
Malay Peninsula
Medial Sumatra T. Z.
Sumatra island
Borneo island
SW Borneo
Woyla Nappe
W Sumatra
Sumatran Fault
Meratus suture
Java island
+10°
+ 5°
0°
- 5°
-10°
+ 95°
+100°
+105°
+110°
+115°

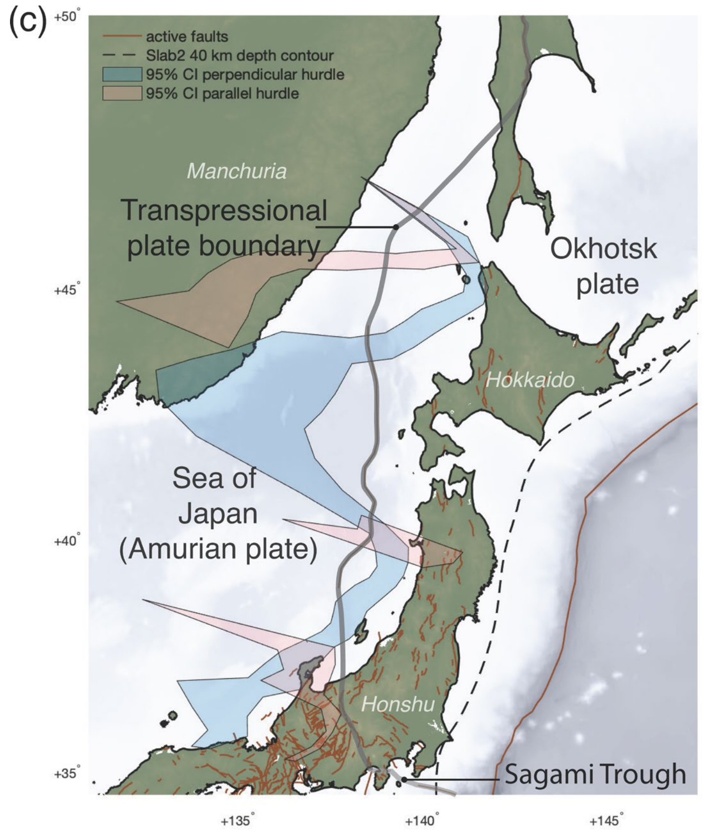

Figure 6. *Location of both hurdles against topography, active faults (green), 40 km depth contour of the top of the slabs (megathrust)* (Hayes et al., 2018)*, and major tectonic and geological features discussed in the main body, for each of the three study areas. Dashed lines indicate inferred or disputed locations. (a) For South America, the eastern front of the Precordillera, the broad location of the Sierras Pampeanas, and the western edge of the Río de la Plata Craton are taken from Álvarez et al. (2012), while the orange line marks the approximate extent of the Proterozoic and older crustal domains* (Chulick et al., 2013)*. (b) For Sunda, the location of the Meratus suture and Southwest Borneo crustal block is taken from Haberland et al. (2014) and Metcalfe (2011), while the Medial Sumatra Tectonic Zone and the crustal domains in Sumatra and the Malay peninsula are taken from Hutchison (2014) and Metcalfe (2011). (c) For Japan, plate boundaries are from Bird (2003).*

2.6 Discussion and conclusions of the data analysis

Trench-perpendicular velocities decreas e with distance from the trench in a broadly linear fashion up to the hurdle. Beyond the hurdle, perpendicular velocities and gradients are distinctly lower.

The hurdle in trench-perpendicular velocities is located within 1000 km or less of the trench along the three studied subduction zones. Trench-parallel velocities sometimes have complex patterns, partly due to curvature of the margin. In South America, parallel velocities generally also decay steeply with distance, up to a hurdle that roughly coincides with the trench-perpendicular hurdle or that is located up to several tens of km closer to the trench. Hurdle locations broadly, but not precisely, follow the inland boundary of the orogen located along the margin, where a clear boundary exists.

That the decay of trench-perpendicular velocities as function of trench distance deviates from a smooth decrease was first noted by Norabuena (1998) for the northern portion of the Central Andes (the Altiplano of Peru and Bolivia) and Brooks et al. (2003) for the Southern Andes. The authors focus on the locally steep velocity gradient at the eastern edge of the Andes and explain the observations by active back-arc convergence or sliver motion, which has remained a popular explanation (Bevis et al., 2001; Brooks et al., 2003, 2011; Kendrick et al., 2006; Métois et al., 2013; Weiss et al., 2016; McFarland et al., 2017; Herman & Govers, 2020; Shi et al., 2020). The interpretation involving active backthrusts implies that interseismic strain accumulation by slip on a backthrust system involves non-recoverable strain by fault slip or shear zones. The fold-and-thrust belt at the eastern margin of the Altiplano-Puna plateau, at roughly 11–22° S latitude, is bounded by a well-defined thrust front and is indeed considered to be actively deforming, despite little recent seismic activity (Brooks et al., 2011; Wimpenny et al., 2018). Farther north in Peru (4–11° S) and farther south in Argentina (around 31° S), moderate instrumentally-observed earthquakes and strong historical earthquakes indicate that some fraction of permanent strain occurs by thrust and reverse faulting in the eastern foreland of the Andes (Jordan et al., 1983; Sébrier et al., 1988; Alvarado & Ramos, 2011; Rivas et al., 2019). However, active and continuous backthrusts faults appear to be absent in some locations along the Andean orogen and the other two subduction zones we study, specifically at 22–29° S and south of 32° S latitude in South America, throughout Sumatra and Java, and south of 39° N and north of 45° N off the west coast of Japan. Elsewhere, in the Sea of Japan, the inferred active faults accommodating convergence between the Okhotsk and Amur plates do not coincide with the location of the hurdle (Figs. 2–5).

Even where active backthrusts are observed, their role in explaining the spatial distribution of surface velocities may have been overestimated because of unrealistic model assumptions. Most studies that numerically model the effect of back-arc convergence on interseismic velocities assume a fully elastic Earth during the entire earthquake cycle, which strongly underestimates far-field horizontal velocities and can lead to mistaken interpretations of observations (Trubienko et al., 2013; Li et al., 2015). Shi et al. (2020) do use a visco-elastic rheology. However, their landward model boundary, with a boundary condition imposing no horizontal motion, is located at a horizontal distance of ~950 km from the trench, i.e. only ~150 km farther than the back-arc thrust front, forcing velocities to decrease to zero there. Additionally, the decrease in trench-perpendicular velocities with distance from the trench is less linear in the model of Shi et al. (2020) than in observations, while the backthrust included in the model produces only local offsets in velocities, above the backthrust. Furthermore, most of the modeling studies invoking back-arc convergence require basal detachment faults extending in the trench-normal direction for ~200 km or more (Brooks et al., 2011; Weiss et al., 2016; McFarland et al., 2017; Shi et al., 2020). This may be unrealistic, considering that the E-W extent of the central Andean back-arc fold-and-thrust belt that is currently geologically active is only ~70 km wide (Pearson et al., 2013). Other authors treat the contact between the Andean orogen and the interior of South America as a plate boundary, implying that this boundary cuts through the entire lithosphere, slipping freely at depth, and that it is laterally continuous all along the orogen. Because of the extreme spatial extent and continuity of the modeled thrusts or plate boundaries, these studies probably overestimate the geodetic imprint of the localized shortening at the eastern edge of the Andes. Additionally, seen at the continental scale, the sharp velocity decrease that has been used as evidence for backthrust slip (Norabuena et al., 1998; Brooks et al., 2011; Weiss et al., 2016; Shi et al., 2020), constitutes a relatively minor deviation from a general decaying trend over the whole orogen (Fig. 3, profiles B and C). Furthermore, the aforementioned studies investigating the spatial distribution of interseismic velocities do not consider whether significant far-field coseismic displacements can be explained by their models. Within the framework of the earthquake cycle, we think there should be consistency in terms of coseismic slip and slip deficit accumulation, response of backthrust slip and creep to the stress evolution during the cycle, and boundary conditions.

Active faults are the possible cause of hurdle behavior in some regions. North of ~2° S in South America, in southern Ecuador and Colombia, convergence is highly oblique and subparallel to a system of strike-slip and thrust faults (Veloza et al., 2012) that roughly coincides with the location of the hurdle in both velocity components. Localization of interseismic velocities might be chiefly caused by the fault system, consistently with the interpretation of this fault system as bounding a distinct, internally deforming North Andean sliver (e.g., Alvarado et al., 2016; Kellogg et al., 1995; Nocquet et al., 2014; White et al., 2003). In Sumatra, trench-parallel velocities seem to be governed by the active strike-slip Sumatran Fault (Prawirodirdjo et al., 1997; Genrich et al., 2000a). Trench-parallel velocities also suggest localized strike-slip motion between southern Hokkaido (on the Okhotsk plate per Bird, 2003) and northern Manchuria (on the Amurian plate), but the lack of GNSS observations in the Sea of Japan precludes a specific localization of the boundary from a purely geodetic perspective.

Trench-perpendicular velocities in all three study areas show a consistent steep decrease with distance from the trench. Trench-parallel velocities in South America, away from the North Andean sliver, show a similar trend. This suggests a more universal cause of the observed hurdles than fault zones. We find no correlation between shallow megathrust dip and hurdle location, since the dip changes very little along the studied trenches (Fig. 5). We therefore focus on a possible explanation involving the overriding plate. Although the thrust faults in the Andean back-arc are unlikely to directly account for the decrease in observed velocities as we move away from the trench, they are likely associated with a mechanical contrast between the deformed and partly accreted Andean region and the interior of the South America plate. We thus hypothesize that such a contrast exists in this and other subduction zones, that it is responsible for the behavior of interseismic velocities, and that a uniform overriding plate cannot account for observations.

The effective elastic thickness T_e derived from flexure observations is much lower at the margin than in the interior of South America (Pérez-Gussinyé et al., 2008, 2007; Stewart & Watts, 1997). Variations in effective elastic thickness may derive from variations in thickness, composition, temperature, rheology, and on the age of the load (Burov & Diament, 1995; Watts, 1981). The effective elastic thickness is derived from lithospheric flexure on geological time scales and is not directly applicable to the predominantly horizontal plate loading over interseismic timescales. It is very likely however that a relevant mechanical contrast exists. The load-bearing capacity of the low-viscosity mantle wedge is negligible on (interseismic) time scales, meaning that the contrast must be related to properties of the overriding plate. The bulk of the interseismic shortening of the overriding plate is recovered during megathrust earthquakes, so it can be considered largely elastic. A mechanical contrast that is relevant in the context of earthquake cycles is thus a compliance contrast or thickness contrast. Below we present mechanical models aimed at exploring our hypothesis that (interseismic) hurdles are a consequence of such contrast, whilst also showing significant coseismic displacements beyond the hurdle.

The presence of stiff cratonic lithosphere in the interior of the South American plate in central Argentina was proposed as the explanation for the relatively low horizontal postseismic velocities in the region (compared to model results without such a craton) by Klein et al. (2016). Itoh et al. (2019) instead showed that a compliant arc and back-arc region can explain the high gradient of onshore horizontal interseismic velocities with distance from the trench in Hokkaido. We hypothesize that a mechanical contrast between more compliant lithosphere at the convergent margin of the overriding plate (in the arc and back-arc region) and less compliant, more rigid lithosphere of the interior of the plate can explain the observed near-trench localization of high spatial gradients of horizontal surface velocities. We thus propose that such a contrast, while avoiding artificially fixed model edges in the vicinity of the trench, can produce a hurdle in interseismic velocities and surface motion generally consistent with observations throughout the seismic cycle, even though we specifically focus here on interseismic observations.

3 Numerical model

3.1 General concept

To study the interseismic and coseismic surface deformation field we develop a three-dimensional (3D) mechanical model. We seek to explain observation trends at different margins, i.e., the semi-linear decrease of interseismic velocities from the trench to the hurdle, the low interseismic strain accumulation beyond it, but significant far-field coseismic displacements due to a megathrust earthquake. We test whether these trends may be a consequence of a compliancy contrast in the overriding plate. In the context of our model, we use a contrast in Young's modulus E and shear modulus G, with the same ratio between the two moduli, in an overriding plate with a uniform thickness and Poisson's ratio ν. Rather than representing realistic averages of the elastic properties of the lithosphere, the model Young's modulus values proxy for a more general ability of the plate to resist intraplate stresses resulting from the total thickness, composition, and thermal state of the real lithosphere. The modeled contrast in the elastic properties of the overriding plate consists of a relatively low Young's modulus in the "near-trench" region and a higher modulus in the far-field. The assumed geometry of the slab and overriding plate in the model is not specific for any margin and instead follows a realistic trench-perpendicular slab profile (Fig. 6). We consequently do not expect to reproduce specific regional observations with the model.

Model deformation is driven by slab motion and periodic unlocking of asperities. The slab itself is kinematically driven, as updip and downdip end of the slab are driven at the interplate convergence rate. Coseismic slip and afterslip are not imposed kinematically and are instead physically determined, together with viscous relaxation, by the asperity size and location and by the mechanical properties of the material in the model. Govers et al. (2018) show that coseismic slip increases per earthquake cycle until no variation occurs from one cycle to the next and physically consistent prestresses have developed.

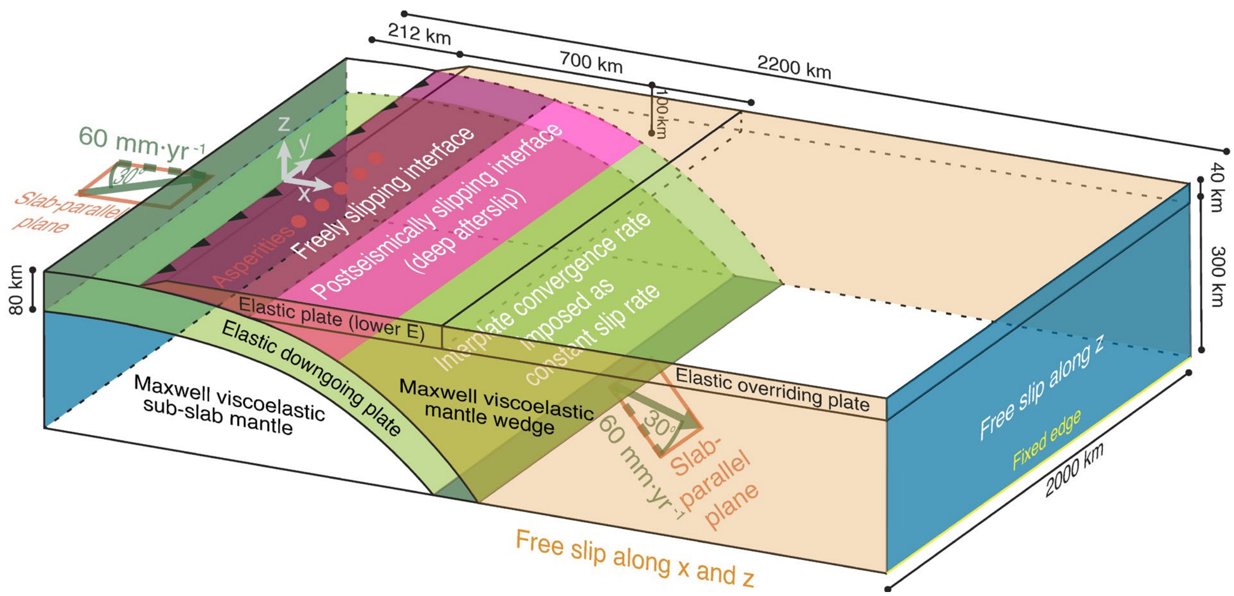

***Figure** 7. Schematic representation of the model domain with its geometry, spatial extent, coordinate system, main mechanical properties, and the applied boundary conditions.*

3.2 Model domain and rheology

We have chosen the model domain size so that boundaries and boundary conditions do not affect the results in our region of interest; the trench-perpendicular (x) model extent is 2200 km, 2000 km in the trench-parallel direction (y) direction, and 338 km in the depth (z) direction. The trench is located at $x = 0$, while the oceanward model boundary is located at x=-212 km. The surface downgoing plate has its upper surface at a depth of 8 km, and the overriding plate at z=0. The subducting plate has a thickness of 80 km, consistent with the seismologically detected depth of the lithosphere-asthenosphere boundary of various oceanic plates (Kawakatsu et al., 2009; Kumar & Kawakatsu, 2011). The overriding plate has a uniform 40 km thickness, except at the taper due to the megathrust geometry at the bottom and at the slope down to the trench over 18 km horizontal distance.

The model slab and the overriding plate are elastic, and the mantle wedge and sub-slab asthenosphere are viscoelastic with a Maxwell rheology. We model seismic cycles with quasi-dynamic slip on discrete faults and shear zones (see Section 3.4 and Govers et al., 2018, Section 2). After model spin-up, the model has identical megathrust earthquake cycles with a return period of 300 years. Postseismic relaxation in the model involves the two most relevant large-scale processes, afterslip and viscous relaxation (Bürgmann & Dresen, 2008; Diao et al., 2014; Broerse et al., 2015; Klein et al., 2016). Our reference model has a mantle viscosity η of 10^{19} Pa·s. Throughout the model domain, outside of the overriding plate, the elastic moduli are uniform: Poisson's ratio ν is 0.25 and Young's modulus E is 100 GPa, consistently with values from PREM (Dziewonski & Anderson, 1981) in the 0–40 km depth range. In particular, the ν value of 0.25 consists of the common Poisson solid assumption (e.g., Melosh and Raefsky, 1983) and is very consistent with the values determined for lower crustal and mantle lithologies, while being at the lower end of the realistic range for the upper crust . The return period thus is ~37.9 characteristic relaxation (Maxwell) times long, so that about 55% of the model cycle period is interseismic, given that the earthquakes on the different asperities within one cycle occur within 40 years of each other (Govers et al., 2018).

3.3 Numerical method

We use a finite element method to solve the 3D mechanical equilibrium equations for given material properties and boundary conditions including a free surface, as detailed below. Finite element platform *GTECTON* version 2021.0 uses the Portable, Extensible, Toolkit for Scientific Computation (*PETSc* version 3.10.4; Balay et al., 2021a, 2021b, 1997) and *OpenMPI* (version 3.0.0; Gabriel et al., 2004) to solve the time-dependent mechanical problem in parallel (e.g., Govers et al., 2018; Govers and Wortel, 2005).

Each model includes 384,566 nodes arranged in 2,238,109 tetrahedral elements and 1,284,193 total degrees of freedom. These choices are based on pilot models to find a mesh where surface deformation is insensitive to further grid refinement. A posteriori estimates of the model error (Verfürth, 1994) for the selected mesh are small enough to support our conclusion that our results are accurate within a few %.

3.4 Modeling the megathrust

Dynamic differential slip on the megathrust is modeled using the slippery nodes technique (Melosh & Williams, 1989). Five asperities on the otherwise freely-slipping megathrust are fully coupled (locked) during all stages of the earthquake cycle, except during the coseismic phase when unlocked asperities can slip freely. Treating the megathrust away from the asperities as freely sliding is consistent with observations of megathrust regions immediately up- and downdip of the asperities sliding stably and with low friction (Scholz, 1998; Ikari et al., 2011; Hardebeck, 2015).

The asperities are circular in map view and have a diameter of 50 km, which is consistent with inversion results of Herman and Govers (2020). They are centered at a horizontal distance of 120 km from the trench and 100 km from each other, resulting in accumulation of slip deficit (locking and pseudo-locking) on and around the asperities, over an along-trench distance of ~500 km (Herman et al., 2018). At the start of each new 300-year cycle, the middle asperity first has its coseismic phase. After a delay of 20 years, the intermediate asperities have their coseismic phase. After 20 more years, the outer asperities have the coseismic phase. Each asperity has its coseismic phase every 300 years. Every coseismic phase is instantaneous (meaning model time does not elapse) and consists of the relevant asperities being unlocked, the megathrust slipping freely until mechanical equilibrium is reached, and the asperities being relocked at the end. Therefore, all slip deficit accumulated on the megathrust interseismically due to each asperity is released during the coseismic phase of that asperity. The distribution of coseismic slip is thus determined by the asperities, and by the mechanical properties of the plates and, to a lesser extent, of the viscoelastic mantle. Coseismic slip can occur at depths shallower than 40 km, as that is the maximum depth of the overriding plate and thus of the megathrust.

Coseismic slip, although traditionally thought to not extend to very shallow depth as a result of the unconsolidated material in the hanging-wall (Kanamori, 1972; Moore & Saffer, 2001), can indeed propagate up to the trench (Fujiwara et al., 2011; Sladen & Trevisan, 2018). We minorly restrict coseismic slip on the updip portion of the megathrust, above 15 km depth, by applying (small) shear tractions that are proportional to the amount of coseismic fault slip, with a spring constant of 200 Pa/m.

Downdip of the megathrust, the contact between the subducting plate and the mantle wedge (depths >40 km in our models) is often viewed as a viscoelastic shear zone (van Keken et al., 2002; Tichelaar & Ruff, 1993). In our model, we represent it as a discrete interface that slips freely interseismically and is fully locked coseismically. Additionally, immediately after each coseismic phase, we include an instantaneous afterslip phase, during which the shear zone, together with the megathrust outside of the asperities, slips freely until mechanical equilibrium is reached. The shear zone thus resolves coseismic stress changes as much as possible via afterslip and creeps interseismically, but behaves as part of the mechanical continuum responding elastic to coseismic slip on the megathrust. This implementation has the significant benefit of avoiding the computationally demanding simulation of viscous flow in a narrow channel, while capturing the main features of interseismic and coseismic behavior and while producing afterslip with no need to impose it kinematically. Govers et al. (2018) used a similar approach, and they defined "primary afterslip" as immediate viscous slip on the shear zone in response to coseismic stress changes that is generally thought to occur much more quickly than bulk viscous relaxation in the mantle wedge (Govers et al., 2018; Muto et al., 2019). "Secondary" afterslip also occurs on the deep shear zone, over time, in response to bulk viscous relaxation during the postseismic phase.

Afterslip on the deep shear zone is commonly assumed to occur at depths shallower than about 80–100 km (Diao et al., 2014; Sun et al., 2014; Yamagiwa et al., 2015; Hu et al., 2016; Freed et al., 2017). Klein et al. (2016) showed that allowing relative motion between the mantle wedge and the slab, by introducing a narrow low-viscosity zone between 70 and 135 km depth along the top of the slab, produces little change in postseismic horizontal surface motion. In our model, we therefore allow afterslip, and interseismic slip deficit accumulation, on the shear zone downdip of the megathrust only at depths smaller than 100 km.

We aim to capture deformation and flow of the mantle wedge and asthenosphere in response to stress changes during the earthquake cycle. To exclude modeling steady-state mantle flow on geological time scales that is irrelevant for the seismic cycle, we use the finite element split node technique (Melosh & Raefsky, 1981) to impose the slab velocity beyond a depth of 100 km. Similarly, we avoid driving long term sub-slab asthenosphere by applying the slab velocity along the base of the slab. We remove a small residue of long-term deformation of the model related to stretching and unbending of the slab that we identify from an identical model without asperities or earthquakes. This approach facilitates loading of the mantle wedge and sub-slab asthenosphere by non-steady velocity/stress perturbations during all stages of the earthquake cycle.

3.5 Boundary conditions

We impose the updip and downdip ends of the downgoing plate to move obliquely at the interplate velocity in the direction parallel to the slab surface. The trench-perpendicular component of the velocity is 60 mm/yr, while the trench-parallel component (34.64 mm/yr) is such that the total velocity is at a 30° angle (counter-clockwise), in a slab-parallel plane, to the trench-perpendicular direction (Fig. 7). We have verified that the presence and magnitude of the trench-parallel velocity does not affect trench-perpendicular late interseismic surface velocities or coseismic surface displacement. We apply a free-slip boundary to the remaining lateral, vertical sides of the model, while we allow only vertical motion at the landward end and fix the bottom landward and oceanward edges of the vertical sides.

Restoring pressures impose isostasy along the free surface of both plates (Govers & Wortel, 1993). These pressures act perpendicularly to the surface and have a magnitude directly proportional to displacement in that direction. The constant of proportionality is the gravitational acceleration (9.8 m/s^2) times the density contrast—3250 kg/m^3 at the top of the overriding plate, 2200 $kg\cdot m^{-3}$ at the top of the oceanic plate.

4 Modeling results and analysis

4.1 Reference model

In our reference model, the overriding plate has a Young's modulus of 50 GPa within 700 km horizontal distance from the trench, while the remainder of the overriding plate has a Young's modulus of 250 GPa. Fig. 7 shows the resulting surface deformation. Fig. 7a and 8c show interseismic velocities for 260 years after the last earthquake on any asperity, i.e., after ~33 Maxwell times and immediately before the next 40-year earthquake sequence on the five asperities. Both the trench-perpendicular and trench-parallel velocity components decrease with distance from the locked asperities. The transect through the central asperity in Fig. 8c (solid line) shows a roughly linear decrease in the trench-perpendicular velocity with distance from the trench, from the peak value (above the asperity) to the location of the contrast, where the gradient decreases sharply. Here, the trench-perpendicular velocity is ~10% of the interplate convergence rate and ~8% of the peak value. Beyond the contrast, the trench-perpendicular velocity in the far-field decreases gradually to zero at the far end of the model, which is a consequence of the model boundary condition there. Trench-parallel velocities along this transect instead decay with a progressively shallower slope away from the peak (Fig. 8c). They reach a near-zero value at the compliance contrast and reach ~10% of the peak value ~200 km closer to the trench. The steeper decrease in the trench-parallel component causes velocity directions in the locked portion of the subduction zone to rotate from convergence-parallel to trench-perpendicular with distance from the trench (Fig. 7a). The results thus show slow and mostly trench-perpendicular interseismic strain accumulation beyond the contrast. The mechanical contrast thus results in hurdle-type behavior comparable to what we infer from the GNSS data. The hurdle is expressed in both horizontal velocity components, albeit more clearly in the trench-perpendicular velocities.

Interseismic velocities 500 km to the north of the middle of the model (Fig.7a and 7c) are substantially slower than above the central asperity. They are higher than velocities 500 km to the south of the central asperity, showing that oblique convergence results in a distinctly asymmetric pattern of interseismic strain accumulation. Particularly the trench-parallel velocity differs. Trench-parallel velocities along the northern transect in Fig. 8a and 8c increase with distance from the trench before decreasing again. Fig. 8a shows that, in a trench-perpendicular profile 500 km the south of the middle of the model, trench-parallel velocities decrease with distance from the trench. Trench-perpendicular velocities on both lateral sides decrease with distance from the trench. The imprint of the contrast on the (gradient of the) velocities is less pronounced away from locked asperities than in the central region.

Unlocking of the central model asperity results in coseismic slip on the megathrust. The coseismic slip on the megathrust corresponds to a moment magnitude M_W=8.7, computed using the average elastic shear modulus of the overriding and subducting plates. Fig. 8b shows coseismic horizontal surface displacements in the overriding plate. The displacement magnitude is highest (~11 m) and obliquely ocean directed above the ruptured asperity. Fig. 8d shows a steep decrease of trench-perpendicular displacement with distance from the trench, and a change in the gradient at the mechanical contrast. Trench-parallel displacements are less affected by the contrast. However, both components are significantly non-zero beyond the compliance contrast.

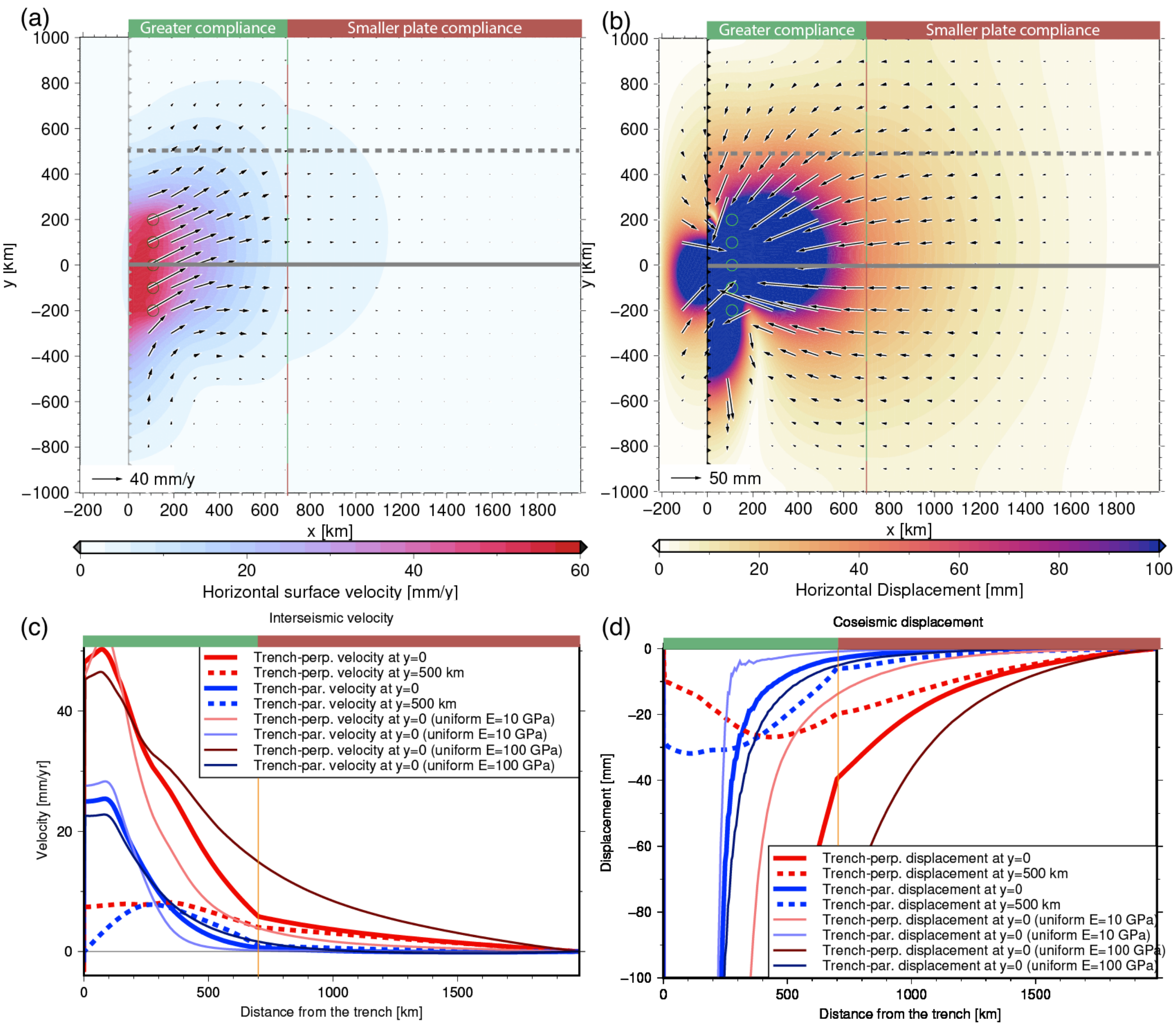

***Figure 8**. Reference model surface deformation and profiles. The extent of the forearc and backarc region with low Young's modulus E, and of the far-field region with high Young's modulus is shown above the panels. **(a)** Interseismic horizontal velocities at the end of the earthquake supercycle, immediately before the next unlocking of the central asperity. Colors show magnitudes, and vectors show directions and magnitudes. The black barbed line indicates the model trench that separates the subducting plate (left) from the overriding plate (right). Black circles are surface projections of locked asperities. Solid and dashed thick gray lines correspond with transect locations in panels (c) and (d). **(b)** Coseismic horizontal displacements due to unlocking of the*

central asperity. Colors show magnitudes, and vectors show directions and magnitudes of horizontal surface displacements. ***(c)*** *Interseismic surface velocity components along transects on the overriding plate shown in (a) with the same line stroke (continuous or dashed). Positive velocities are landward, to the right.* ***(d)*** *Coseismic displacement components along a trench-perpendicular transects show in (b). Seaward displacement is negative, to the left.*

4.2 Lateral compliance contrast versus a homogeneous plate

We compare the results of our reference model with results from two other models, both with an overriding plate with a uniform Young's modulus, and all else the same as in the reference model (Fig. 8c). We find that a low uniform value of 10 GPa produces a steep decrease in both interseismic velocity components, i.e., it concentrates interseismic strain closer to the trench. However, it lacks significant trench-perpendicular coseismic displacement in the far-field, with amplitudes below 10 mm at distances from the trench greater than 800 km, unlike our reference model. Conversely, a uniform, realistic value of 100 GPa for the overriding plate produces large far-field coseismic displacement. However, its trench-perpendicular interseismic velocities decrease slowly and have significant amplitudes (more than a third of the peak value) at the location of the contrast in the reference model (700 km from the trench).

We conclude that a uniform overriding plate cannot simultaneously explain the observed interseismic hurdle and far-field coseismic displacements. A compliance contrast in the overriding plate does explain an interseismic hurdle and far-field coseismic displacements.

4.3 Radial elasticity variations

Pollitz et al. (2011a, 2011b) concluded that radial elasticity layering is needed for fitting both the near- and far-field coseismic static GNSS displacements following the Maule and Tohoku earthquakes. We evaluate to what extent a radial elasticity variation affects the model results. We use elastic moduli varying with depth according to PREM (Dziewonski & Anderson, 1981; Pollitz et al. 2011a,b). The modeled interseismic surface velocities differ little from a model with uniform Young's modulus E=100 GPa (Fig. S15), being less than 5% higher or lower and near-indistinguishable beyond 300 km of distance from the trench. We conclude that the hurdle-type response of interseismic velocities cannot be explained by the radial elasticity layering only. In the context of our numerical models a lateral contrast is thus needed in the overriding plate to reproduce the hurdle-like observations. In Sections 5.2 and 5.3 we address the tectonic and rheological viability of a mechanical contrast in overriding plates.

4.4 Importance of near-trench elasticity and of its contrast with far-field elasticity

The reference model uses a Young's modulus E=50 GPa in the near-trench and E=250 GPa in the far-field of the overriding plate. The latter value is beyond the upper limit of ~200 GPa for lithospheric rocks (specifically eclogite; Aoki and Takahashi, 2004; Christensen, 1996). Here we explore the sensitivity of our model results to elastic properties.

We systematically vary the Young's modulus in both the near-trench and the far-field portion of the overriding plate. Fig. 9a,b shows trench-perpendicular profiles of interseismic velocities through the central asperity for models where the Young's modulus is higher in the far-field than near the trench by a factor of 3 (red) and 5 (purple), with different average values (less continuous line strokes for lower values). We also vary the Young's modulus of the far-field while keeping the near-trench value the same (Fig. 9c,d), the latter with a value of 50 GPa (purple), 30 GPa (dark red), or 20 GPa (orange) with less continuous line strokes for lower far-field values. In Fig 9e,f we do the opposite, showing the effect of different values of Young's modulus in the near field (less continuous strokes for lower values) while keeping a far-field value of 150 GPa (dark red) or 100 GPa (orange).

Looking at the trench-perpendicular velocities (Fig. 9a,c,e), the results show that a larger contrast in E result in lower velocity amplitudes trenchward of the contrasts and steeper slopes in velocity, particularly between 200 and 300 km of distance from the trench, and in shallower slopes beyond the contrast (Fig, 9a). Lowering both values of E accordingly, while keeping the amplitude of the contrast unaltered, has a similar effect (Fig, 9a, different line strokes with the same color). The effect of increasing the far-field value of E while keeping the near-trench value constant (Fig. 9c) is generally smaller than doing the opposite (Fig. 9e), but it is still noticeable when the near-trench E is high (Fig. 9c, purple lines). With lower near-trench E values, increasing the far-field E is hardly noticeable (Fig. 9c, dark red lines and orange lines). There is no sharp cutoff beyond which hurdle behavior is exhibited, and a break in the slope of the profile is always present at the location of the contrast, if any. We take the trench-perpendicular hurdle to be a good indicator of the location of a compliance contrast in the overriding plate.

The amplitude (i.e., ratio) of the contrast in Young's modulus on trench-parallel velocities (Fig, 9b) is variable. This is because the far-field Young's modulus by itself has very little effect on the profiles of trench-parallel velocities (Fig. 9d). The near-trench Young's modulus alone controls the decrease in trench-parallel interseismic velocities with distance from the trench, with lower values causing a steeper decrease on the landward side of the peak velocity (Fig. 9f). We observe however that all curves (including the uniform E model) decrease to low velocities at the contrast, i.e., hurdle behavior of trench-parallel interseismic velocities is not a very strong indicator for a compliance contrast.

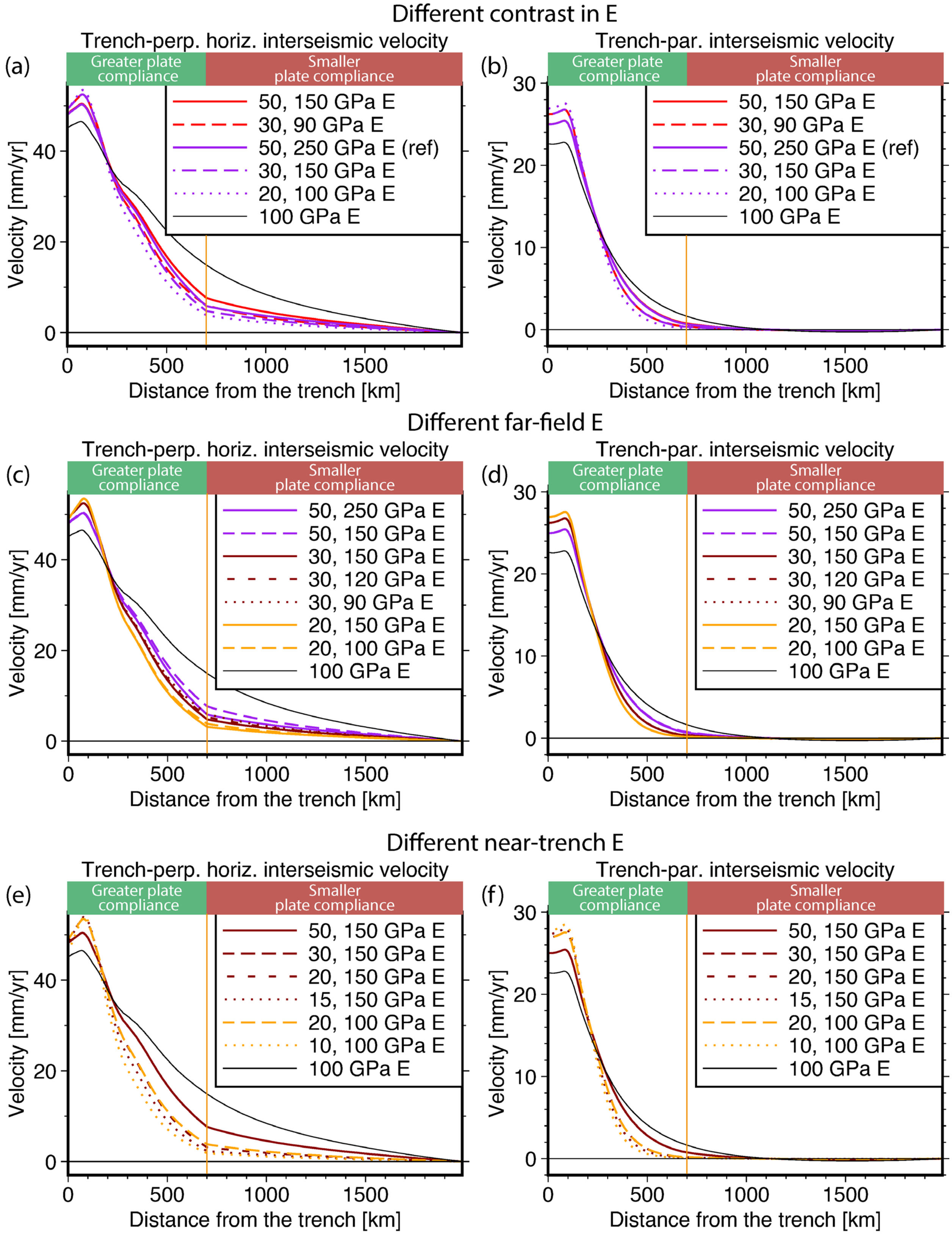

Different contrast in E
Trench-perp. horiz. interseismic velocity
Trench-par. interseismic velocity
(a)
(b)
Greater plate compliance
Smaller plate compliance
50, 150 GPa E
30, 90 GPa E
50, 250 GPa E (ref)
30, 150 GPa E
20, 100 GPa E
100 GPa E
Velocity [mm/yr]
Distance from the trench [km]
Different far-field E
(c)
(d)
50, 250 GPa E
50, 150 GPa E
30, 150 GPa E
30, 120 GPa E
30, 90 GPa E
20, 150 GPa E
20, 100 GPa E
100 GPa E
Different near-trench E
(e)
(f)
50, 150 GPa E
30, 150 GPa E
20, 150 GPa E
15, 150 GPa E
20, 100 GPa E
10, 100 GPa E
100 GPa E

***Figure 9**. Interseismic velocity components along the transect through the central asperity (solid grey line in Fig.7a). The extent of the forearc and backarc region with low Young's modulus E, and of the far-field region with higher Young's modulus is shown above the panels. The location of the contrast in E, if any, is also marked by the dark orange vertical line. **(a,c,d)** Trench-perpendicular velocity, and **(b,e,f)** and trench-parallel velocity. **(a,b)** Different average E values (different line strokes, less continuous for lower values) with the same contrast (ratio) between near-trench E and far-field E (same color). **(c,d)** Different far-field E values (different line strokes, less continuous for lower values) with the same near-trench E values (same color). **(e,f)** Different near-trench E values (different line strokes, less continuous for lower values) with the same far-field E values (same color). The model with a uniform of E of 100 GPa is always shown in black.*

Fig. 10 shows profiles of trench-perpendicular coseismic displacement (corresponding to an earthquake with M_W=8.7) of the same models as in Fig. 9. The amplitude of the far-field displacement is controlled by the Young's modulus in the near-trench, more compliant portion of the plate, regardless of the contrast with the higher Young's modulus in the less compliant internal portion. Pollitz et al., 2010 observed trench-perpendicular coseismic displacements after the M_W=8.8 Maule earthquake up to a few tens of millimeters beyond 700 km from the trench. A near-trench Young's modulus $E \geq 20$ GPa is needed for a coseismic displacement greater than 20 mm 700 km from the trench (where the contrast is located in the reference model), while a modulus of 50 GPa is needed for a displacement of 20 mm 1000 km from the trench. This need for a moderate E in the near-trench region, combined with the need for a sufficient E contrast in to reproduce the hurdle behavior in trench-perpendicular interseismic velocities, requires the use of a very high far-field E in the overriding plate of the reference model (Section 4.1) to produce realistic behavior both interseismically and coseismically. If the far-field E is only moderately high (~100 GPa or less, for instance), the contrast between far-field and relatively near-trench E is probably insufficient to explain hurdle behavior, given that coseismic displacement requires near-trench E to be moderate. In this case, the compliance contrast within the overriding plate, responsible for the hurdle, should be greater than implied by the elastic moduli of the constituent materials alone. In Section 5.3 we discuss the rheological implications of the model sensitivities presented here.

4.5 Shear modulus contrast in the overriding plate

We thus far focused on contrasts in Young's modulus E, which is the resistance to interseismic (elastic) shortening of the overriding plate in response to the head-on component of the convergence velocity. The resistance to (elastic) shear deformation due to the trench-parallel component of the convergence velocity is better represented by the shear modulus $G = \frac{E}{2(1+\nu)}$.

All presented models used a uniform Poisson's ratio ν=0.25, meaning that the contrasts in Young's modulus E and shear modulus G are the same. We now test whether varying the contrast in G while keeping the contrast in E constant, affects trench-perpendicular and -parallel velocities. The near-field and far-field values of E are 30 and 150 GPa, respectively, while ν is 0.2. We decrease the near-field G by 14% through a drastic increase (doubling) in Poisson's ratio, to 0.4, which results in a slight change in the trench-parallel velocity, but does not alter the trench-perpendicular velocity (Fig. S16). Different contrasts in E and G are thus unlikely to affect the apparent hurdle location, particularly as determined in the trench-perpendicular component of velocities, justifying our use of the same contrast in both moduli.

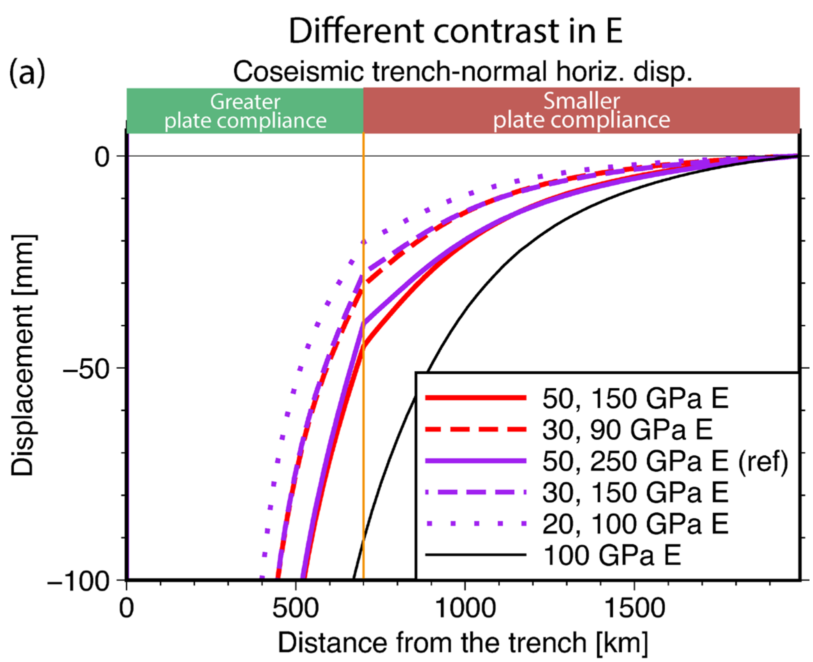

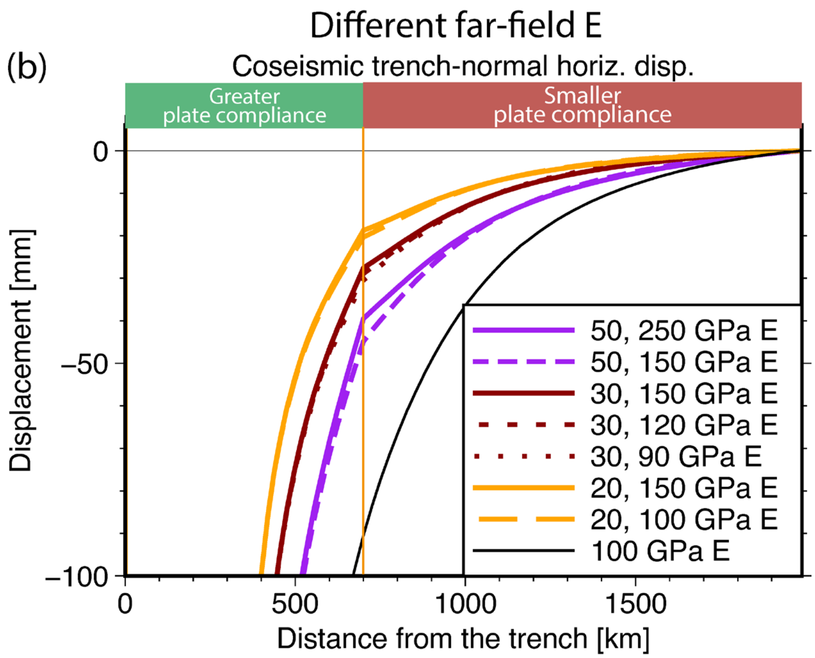

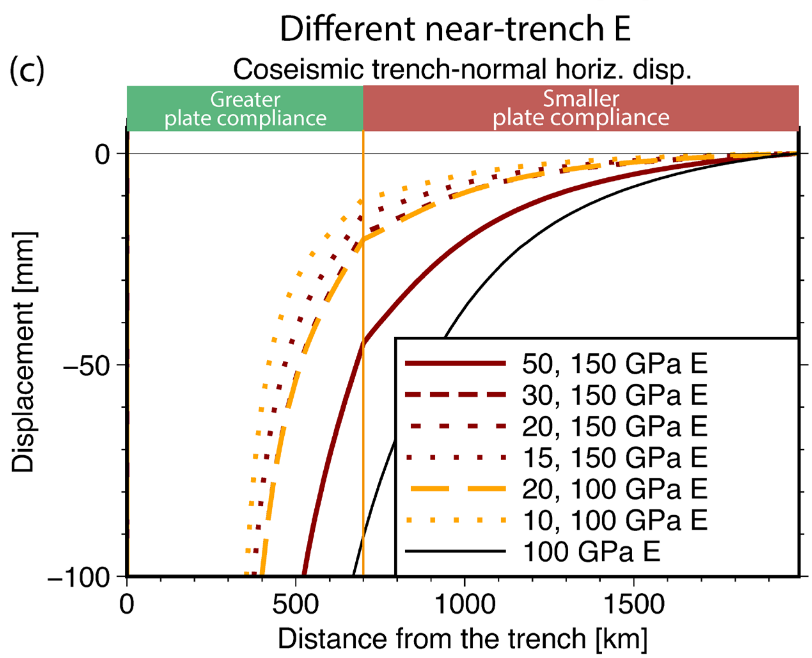

Figure 10. *Trench-perpendicular profiles of intermediate- and far-field trench-perpendicular coseismic displacement at y=0, for models with different contrasts in E and for a uniform model as comparison.* ***(a,b)*** *Different average E values (different line strokes, less continuous for lower values) with the same contrast (ratio) between near-trench E and far-field E (same color).* ***(c,d)*** *Different far-field E values (different line strokes, less continuous for lower values) with the same near-trench E values (same color).* ***(e,f)*** *Different near-trench E values (different line strokes, less*

continuous for lower values) with the same far-field E values (same color). The model with a uniform E of 100 GPa is always shown in black.

4.6 Role of the location of the mechanical contrast

We investigate the sensitivity of the models to the location of the contrast in E by stepwise reducing its distance from the trench to 400 km in 100 km intervals. We do so in a model with a contrast that produces the largest differences in interseismic velocities compared to a uniform E (10 and 100 GPa; Fig. 9). Bringing the contrast closer to the trench most noticeably affects trench-perpendicular velocity profiles (Fig. 11a). Increasing the contrast distance produces less uniform decay of such velocities on the trenchward side of the contrast, as the slope becomes shallower before reaching the contrast. Instead, when the contrast distance is increased, the velocities at the contrast become lower while beyond the contrast, the slopes become flatter. Trench-parallel velocities are much less affected by the location of the contrast (Fig. 11b), as the near-trench value of E controls the general shape of the decrease. The presence of a single contrast in E can thus produce a varying distance between the apparent location of the hurdle (a sharp transition between a steep decay and near-0 amplitudes) in the two components of horizontal interseismic velocities, depending on the near-trench value of E and its spatial extent. Overall, the two horizontal velocity components not only have different spatial distribution with the same contrast, but also respond differently to variations in distance to the contrast or in the value of E on either side of the contrast. This behavior is compatible with our observations showing that the apparent location of the trench-parallel hurdle relative to the trench-perpendicular one varies along a subduction zone and between subduction zones, rather than coinciding with it or being offset by a constant distance.

Interseismic locking results in steadily increasing shear tractions on asperities. The slope of the velocity curves in Fig. 11 represents horizontal strain accumulation rates in the overriding plate. In the region within 200 km from the trench, strain accumulation rates show to be insensitive to the distance of the contrast, and shear tractions on asperities are consequently expected to be insensitive to the width of the zone where strain accumulates. Fig. S15 shows indeed that the average traction on the middle asperity in the downdip direction increases little with decreasing trench-contrast distance; for instance, the traction becomes only ~3% larger when the distance to the contrast reduces from 700 to 500 km. The temporal rate of change of this traction at the end of the cycle in the late interseismic phase is linear and thus increases by the same, small amount. Overall, the presence and location of the mechanical contrast in the overriding plate has little effect on stressing rates on locked asperities.

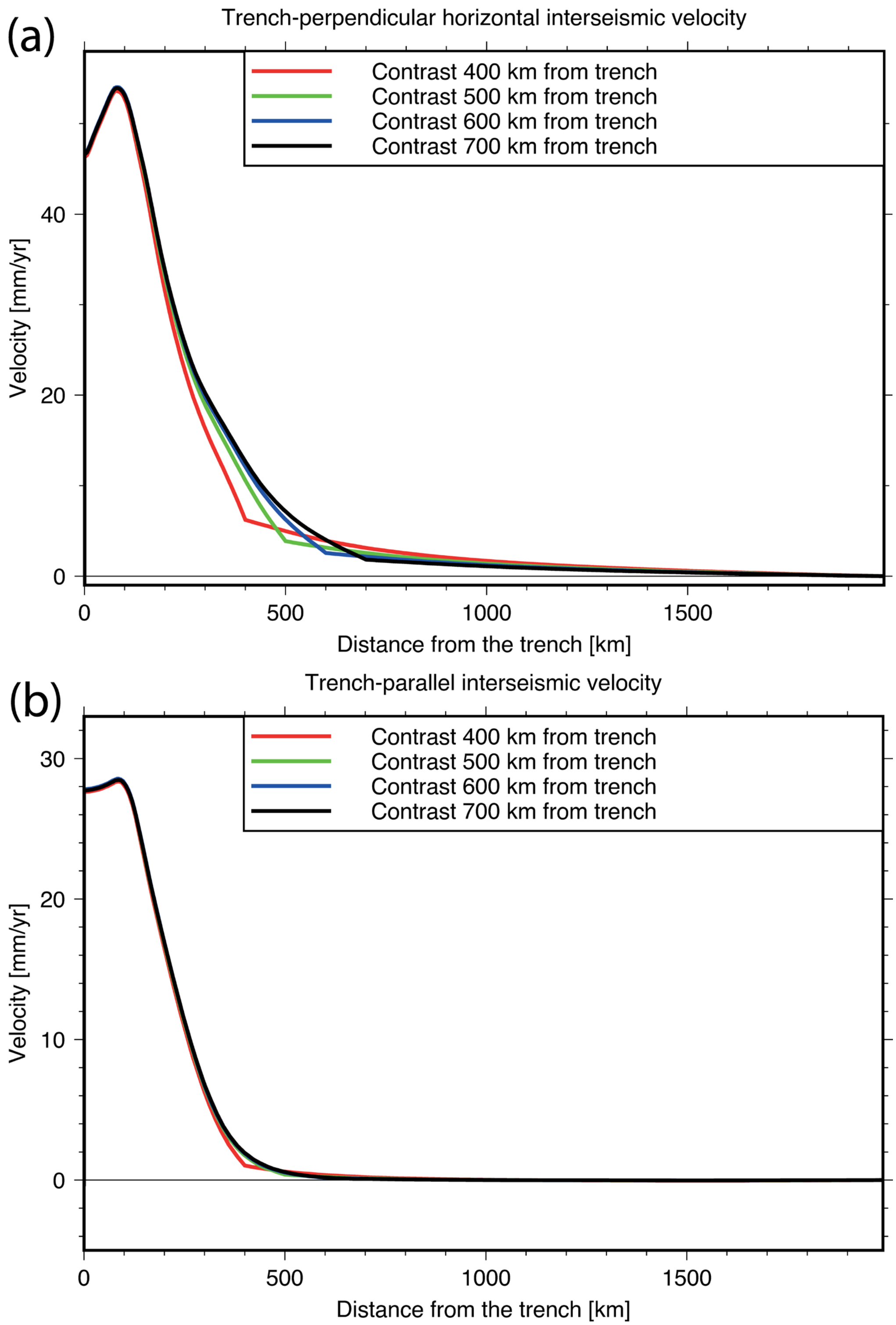

Figure 11. *Trench-perpendicular profiles through the middle of the model, at y=0, of the interseismic horizontal surface velocity components, trench-perpendicular (a) and trench-parallel (b), respectively, for models with a contrast in the E value of the overriding plate (10 GPa near-trench, 100 GPa in the far-field) for different trench-contrast distances.*

4.7 Megathrust locking pattern affects the detectability of hurdles and contrasts

To assess the effect of a contrast on interseismic velocities in areas of low interplate locking, such as northern Peru and Ecuador (Herman & Govers, 2020; Nocquet et al., 2017), we run two simulations in which the two intermediate asperities are removed, leaving 3 total asperities (2 lateral asperities centered 200 km from the center of the middle one). We cut a profile halfway between the middle and outer asperities (at y=100 km) (Fig. 12). The profile through the former asperity (with 3 remaining asperities in the model) has lower trench-perpendicular velocities than the same profile through the asperity (model with 5 asperities), with a shallower slope of decrease in the near-trench portion of the overriding plate, but still with a clear hurdle in the form of a break in the slope at the location of the contrast in E (Fig. 12a). Trench-parallel velocities have a similar behavior, except that velocities beyond the contrast are approximately identical.

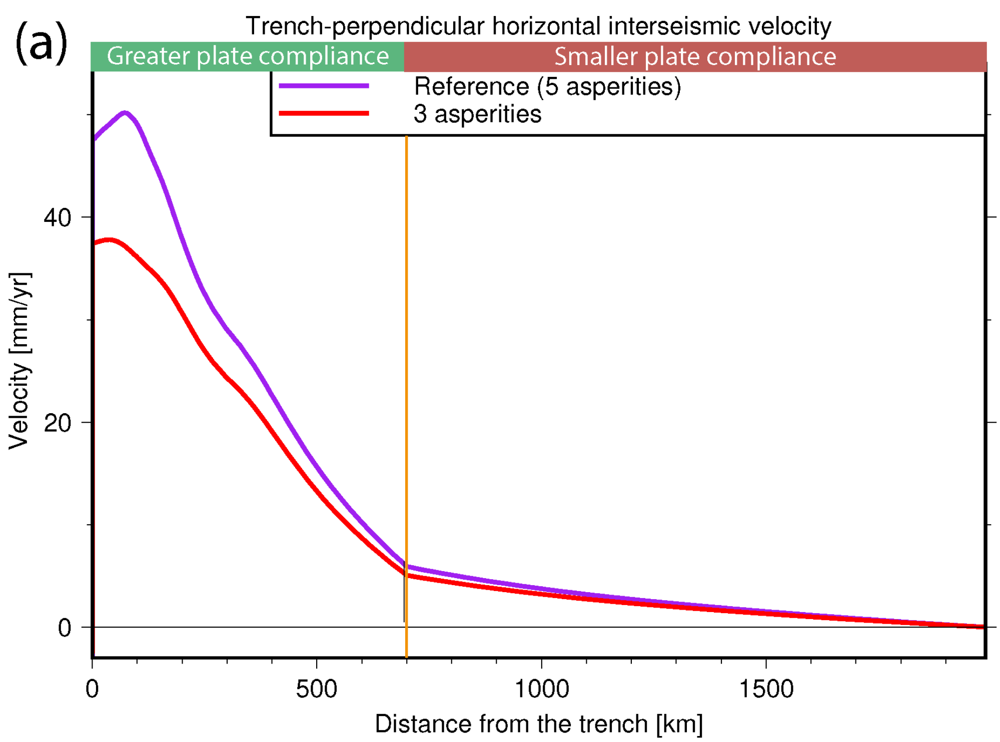

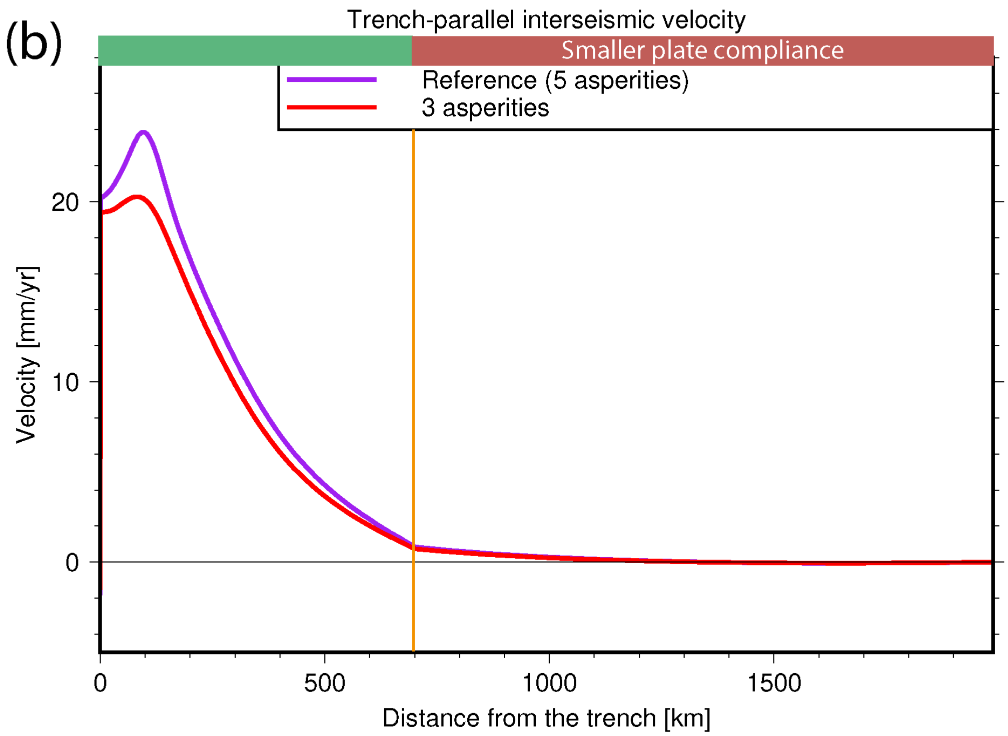

Figure 12. *Trench-perpendicular profiles at y=100 km (through the middle of one of the intermediate asperities, if present) of the two horizontal velocity components, trench-perpendicular (a) and trench-parallel (b), of interseismic velocities in a model with or without an intermediate asperity centered at y=±100 km, halfway between the middle one (at y=0) and each of the outer ones (at y=±200 km).*

4.8 Lateral thickness variation and sharpness of the mechanical contrast

In our models, a contrast in elastic moduli in an overriding plate of uniform thickness is a proxy for a general contrast in the plate's elastic compliance. We test the addition of a step increase in overriding plate thickness, doubling in thickness from 40 km at $x<700$ km to 80 km at $x\geq700$ km, to our reference model and to the model with a uniform E of 100 GPa. The trench-perpendicular interseismic velocity decreases ~30% at the contrast while leaving the peak value unaffected, thus making its decrease with distance from the trench slightly steeper on the oceanward side of the contrast and more gradual on the beyond the contrast (Fig. 13). Trench-parallel velocities are unaffected by the thickness contrast. Heterogeneity in overriding plate thickness, and particularly a thinner arc region, likely contributes to the observed behavior of interseismic surface velocities, but is not solely responsible for hurdle characteristics.

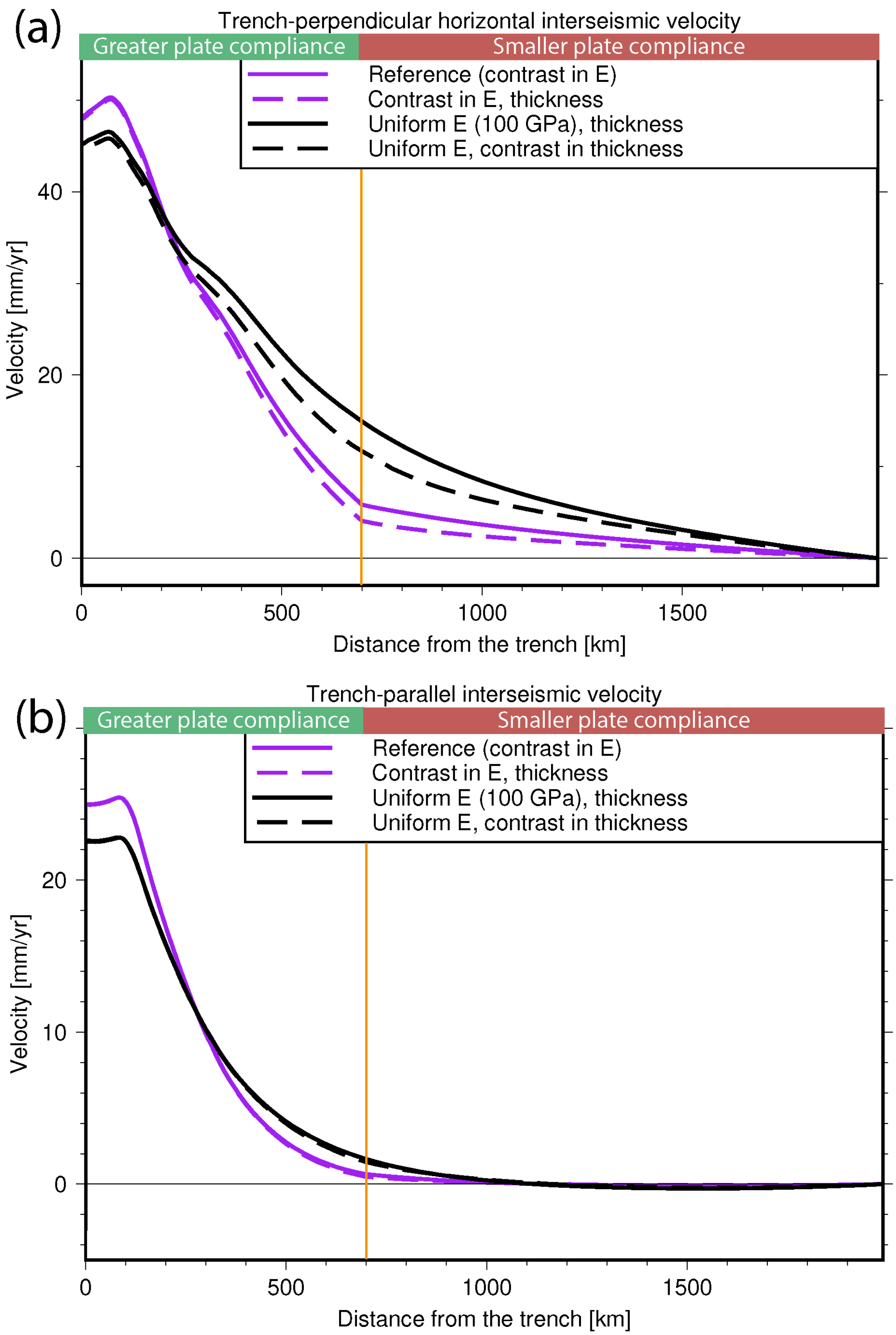

***Figure 13**. Trench-perpendicular profiles at y=0 km of the two horizontal components, trench-perpendicular (a) and trench-parallel (b), of interseismic velocities in a model with or without a contrast in overriding plate thickness (40 km at x <700 km, 80 km at x>700 km). In both models there is the same contrast in overriding plate elastic moduli: the thinner portion of the plate has E=50 GPa and the thicker one E=250 GPa.*

4.9 Effect of the ratio of the earthquake recurrence interval to the Maxwell time

The ratio $\frac{T}{\tau}$ of the earthquake recurrence interval T to the characteristic Maxwell relaxation time $\tau = \frac{\eta}{G}$ is an important property of the megathrust system. In fact, it determines to what extent coseismic stresses have relaxed late in the cycle, and thus to what extent late interseismic motion reflects steady-state loading of the plate due to continued convergence and locking (Savage, 1983). Higher $\frac{T}{\tau}$ ratios reduce the slope of trench-perpendicular velocities with distance from the fault trace in a simple 2D dip-slip fault cutting across an elastic lithosphere overlying a Maxwell viscoelastic mantle (Wang et al., 2021). Our models so far use a $\frac{T}{\tau}$ ratio of 37.9, intermediate for the range of possible ratios observed for subduction zones worldwide and representing a case in which the stress changes due to coseismic slip and afterslip have relaxed late in the cycle (Govers et al., 2018).

We now explore the effect of reducing the $\frac{T}{\tau}$ ratio of our model with uniform elastic moduli throughout (ν=0.25, E =100 GPa in the overriding plate and elsewhere), while keeping the convergence rate and earthquake size constant. Fig. 14 shows the interseismic velocity profiles for the model with the reference model viscosity of 10^{19} Pa·s (black line, same model and curves as in Figs. 8, 8, and 11), and for alternative models with higher viscosities (i.e., longer relaxation times and smaller $\frac{T}{\tau}$) of the viscoelastic mantle. The resulting interseismic model velocities decrease more steeply with distance from the trench with decreasing $\frac{T}{\tau}$. The effect is particularly significant for the trench-perpendicular component. When the $\frac{T}{\tau}$ ratio is halved to 18.9, the effect is limited and the trench-perpendicular velocities still decrease shallowly with distance. However, further reducing $\frac{T}{\tau}$ makes the slope at intermediate-field distances even steeper, and particularly $\frac{T}{\tau}$

<10 makes the velocity 700 km away from the trench equal to or lower than 25% of the peak value. This indicates that, for a sufficiently long Maxwell time relative to the earthquake recurrence interval, the hurdle behavior exhibited by observed trench-perpendicular velocities may be explained without invoking a contrast in the compliance of the overriding plate. We further discuss the viability and implications of such explanation in Section 5.2.

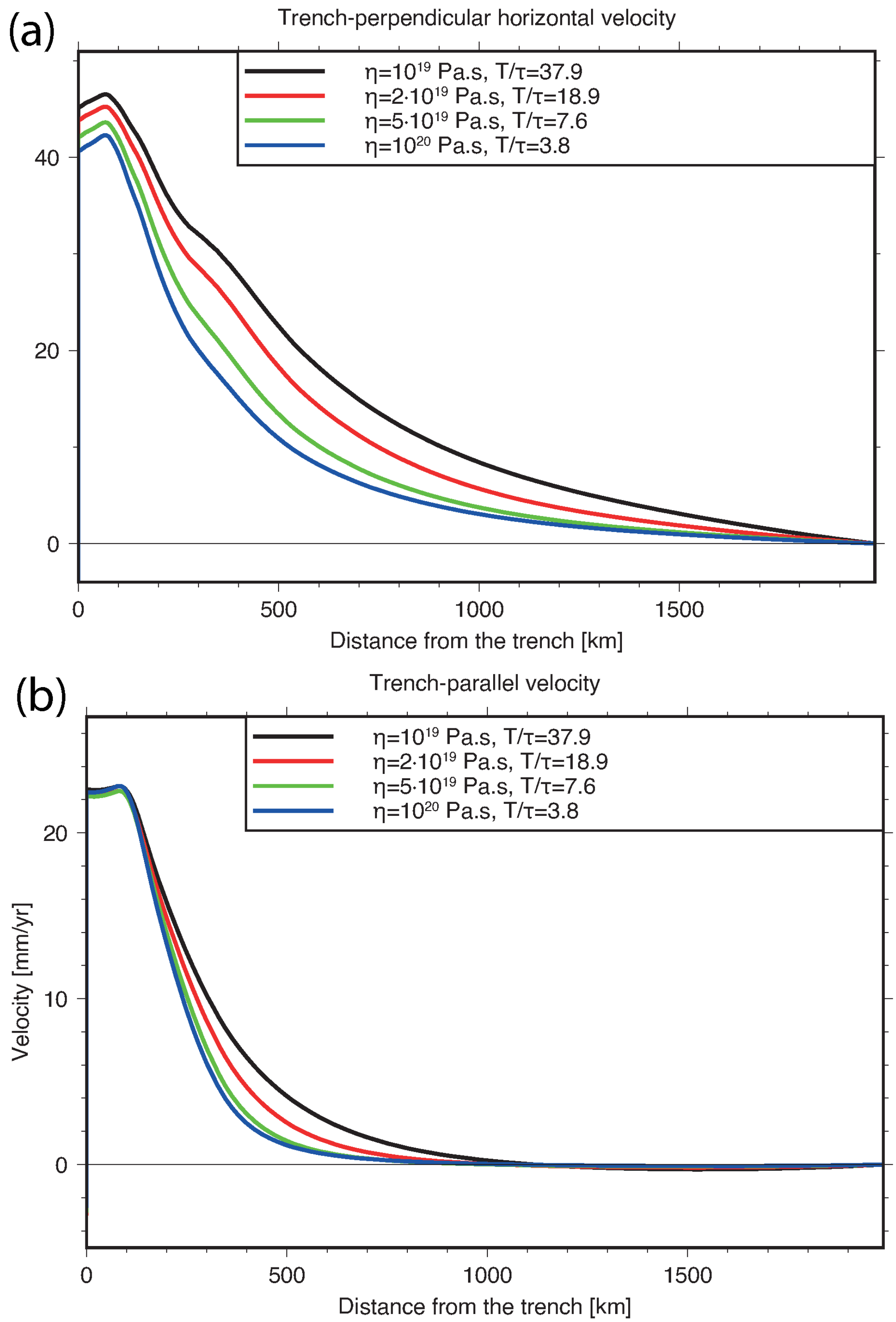

***Figure 14**. Trench-perpendicular profiles at y=0 km of the two horizontal components, trench-perpendicular (a) and trench-parallel (b), of interseismic velocities in models with a uniform E of*

100 GPa and different values of viscosity η*, and thus Maxwell characteristic relaxation time* τ *and the ratio* $\frac{T}{\tau}$ *of the earthquake return period* T *to* τ*, in the viscoelastic mantle domains.*

5 Discussion and implications

5.1 Scope and limitations of our study

We reevaluate published interseismic GNSS velocity observations along three subduction margins: the Peru-Chile Trench (South America), the Sunda Trench (Sumatra, Java), and the Japan Trench (Hokkaido and northern Honshu). In South America, our analysis is not hampered by marine basins, which therefore yields the most continuous sampling of the kinematics in the overriding plate. The analysis will need to be extended to other convergent margins before we can conclude that hurdles, breaks in the interseismic velocity gradient, are global features of megathrust margins. Still, with three out of the three margins showing hurdles, we think that we have a basis to hypothesize a more common feature that mechanically separates the deforming margin from a semi-stable overriding plate interior.

Our mechanical models are generic in their geometry, earthquake cycle, and mechanical properties. Further work will be needed to model the specific contribution of regional rheological makeup and active deformation structures to interseismic velocities. It will be important to also include radial elasticity variations and the sphericity of the Earth. The former feature decreases near-trench velocities, and far-field velocities remain the same (Pollitz et al., 2011b, 2011a; see also Section 4.3). Sphericity has been shown by Nostro et al. (1999) to have a negligible effect on coseismic horizontal displacement due to thrust faulting at distances of 0 to 5000 km from the trench. Trubienko et al. (2013) showed that interseismic displacement normalized by coseismic displacement 700 km from the trench has the same slope towards the end of the cycle, regardless of sphericity, indicating that interseismic velocities at the end of the cycle should also be hardly affected.

5.2 Role of the Maxwell time in relation to the earthquake recurrence interval

As we show in Section 4.9, low values (broadly below 10) of the $\frac{T}{\tau}$ ratio cause the velocities to decrease more steeply with distance from the trench. In that case, coseismic stresses have not fully relaxed before the next earthquake occurs, and as a result viscoelastic model results become similar to those of fully elastic models. This effect is consistent with the results of the simple 2D models of Wang et al. (2021) and of the earthquake cycle models of Li et al. (2015) and Trubienko et al. (2013). It is also analogous to the finding by Zhu et al. (2020) that shorter recurrence time, for a given viscoelastic rheology, leads to greater localization of interseismic deformation around strike-slip faults. Trubienko et al. (2013) explain the spatial distribution of interseismic velocities in two transects, one through central Sumatra and the Malay peninsula and another in northern Honshu in Japan, using an earthquake cycle model with a uniform elastic overriding plate. Their model employs a plane-strain approximation, a Burgers viscoelastic rheology for the mantle with a steady-state (Maxwell) viscosity $\eta = 3 \cdot 10^{19}$ Pa·s, asthenospheric elastic parameters from PREM (Dziewonski and Anderson, 1981; giving $G \approxeq 68$ GPa and $\nu \approxeq 0.28$ in the asthenosphere), and a return period of 170 years. Their $\frac{T}{\tau}$ is thus ~7.2, accounting for the fact that τ is $3\frac{1-\nu}{1+\nu}\frac{\eta}{G}$ higher in the plane strain regime (Melosh & Raefsky, 1983). Li et al. (2015) similarly reproduce interseismic velocities in the North Chile portion of the Andean subduction zone in a model with a uniform overriding plate, a viscosity of $4 \cdot 10^{19}$ Pa·s in the Maxwell viscoelastic mantle underlying the overriding plate, an earthquake cycle duration of 200 years, and a resulting $\frac{T}{\tau}$ of ~10.1.

Li et al. (2015) and Trubienko et al. (2013) do not incorporate finite gradients in slip deficit downdip of the locked interface and instead impose slip deficit to sharply transition from non-zero to zero at the downdip end of the megathrust. A sharp transition in slip deficit is physically unlikely (Herman & Govers, 2020) and precludes the occurrence of the intermediate-depth afterslip (down to at least 80 km depth) that has been inferred from geodetic and seismological observations (Diao et al., 2014; Sun et al., 2014; Yamagiwa et al., 2015; Hu et al., 2016; Freed et al., 2017). The depth to which slip deficit accumulates is especially important, as Li et al. (2015) and Trubienko et al. (2013) show that greater locking depths producing larger intermediate- and far-field velocities. These studies rely on shallow locking depths to reproduce interseismic velocities.–Furthermore, when inverting observations, Li et al. (2015) do not apply a model spin-up, necessary to obtain viscous stresses and strain rates consistent with the long-term repetition of the earthquake cycle. As Li et al. (2015) point out, the spin-up would increase horizontal velocities, particularly in the intermediate-field (100–300 km from the trench), decreasing their trench-perpendicular slope. Therefore, the steepness of the decrease in interseismic velocities with distance from the trench is overestimated for a given $\frac{T}{\tau}$ ratio in the models of Li et al. (2015) and Trubienko et al. (2013). Nevertheless, their results suggest that low $\frac{T}{\tau}$ ratios might explain the apparent hurdle behavior of interseismic velocities in the absence of contrasts in the compliance of the overriding plate.

Models of postseismic relaxation following the 2004 Sumatra-Andaman earthquake, using Burgers rheologies for the asthenospheric mantle, consistently indicate steady-state viscosities of ~10^{19} Pa·s, corresponding to a Maxwell time τ of ~5 years (Hu & Wang, 2012; Govers et al., 2018; Qiu et al., 2018), while the recurrence interval for an earthquake of similar size has been estimated to be between 174 and 600 years (Gahalaut et al., 2008; Meltzner et al., 2010; Van Veen et al., 2014), yielding $\frac{T}{\tau}$ ratios of 34.8–120. For the Chilean convergent margin, Klein et al. (2016) and Li et al. (2018) invert postseismic GNSS observations in the few years (5 and 8, respectively) following the 2010 Maule earthquake, using a Burgers or Maxwell viscoelastic rheology, and consistently find Maxwell viscosities of 5–6·10^{18} Pa·s in the continental asthenosphere under the Andes, corresponding to Maxwell times of 2.4–3.0 years. Aron et al. (2015) estimate the return period as between 84 and 178 years, which would put $\frac{T}{\tau}$ in the 28.0–74.2 range. In the Japan subduction zone, simultaneous inversions of GNSS time series following the 2011 Tohoku earthquake into afterslip and visco-elastic relaxation parameters, using Burgers or non-linear flow law–based visco-elastic rheologies for the asthenosphere, indicate that the steady-state viscosity of the mantle wedge is in the range of $4\text{–}10 \cdot 10^{18}$ Pa·s (Agata et al., 2019; Muto et al., 2019; Fukuda & Johnson, 2021). This corresponds to Maxwell relaxation times of 2.0–5.0 years and is in agreement with the results of the inversion of gravity data into viscous relaxation parameters only by Cambiotti (2020). The recurrence interval T for events similar to the 2011 Tohoku-oki earthquake is ~600 years (Satake, 2015), which puts the $\frac{T}{\tau}$ ratio in the 120–300 range. The ratios (12.1 and 7.2, respectively) used by Trubienko et al. (2013) and Li et al. (2015) are thus below the low end of the realistic range. Our models reproduce the hurdle-like response for low ratios of $\frac{T}{\tau}$ (section 4.9). Still, higher ratios are more realistic for the active margins that we investigate, and our model results show that hurdle behavior is not reproduced with high $\frac{T}{\tau}$ ratios (mantle viscosities in line with the majority of postseismic studies) combined with uniform elastic compliancy of the overriding plate (sections 4.2 and 4.4). This argues for compliancy contrasts in the overriding plate.

5.3 Tectonic significance of a mechanical contrast

Klein et al. (2016) suggest that stiff cratonic back-arc lithosphere in central Argentina affects horizontal and vertical postseismic surface velocities following the Maule earthquake. Li et al. (2018) invert postseismic displacements, including in the far field, following the Maule earthquake into rheological structures of the upper mantle, finding strong evidence for a stiff (elastic, or viscoelastic with high viscosity) cratonic lithospheric root beneath central Argentina. Seismic data also indicate that the Andean lithosphere has very thick crust and warm lithospheric mantle that contrast with thinner (but still thick) cratonic crust underlain by cold, stiff lithospheric mantle farther to the east, from Venezuela to central Argentina (Chulick et al., 2013). This juxtaposition represents a significant contrast in lithospheric averages of the compliance. The hurdle location that we inferred from the GNSS velocities agrees with the tectonic boundary (Section 2.5, Fig. 6a). Immediately to the south of the Central Andes, around 30°S, the trench-perpendicular hurdle coincides with different terrane and active tectonic boundaries (Fig. 6a; Ramos, 1999, 1988). In particular, it is located between the eastern front of the active Andean Precordillera fold-and-thrust belt (Baldis et al., 1982; Ortiz & Zambrano, 1981) and the western margin of the Rio de la Plata craton (Álvarez et al., 2012), within a mountain range (the Sierras Pampeanas) characterized by active reverse faults and lateral contrasts in crustal thickness and layering (Perarnau et al., 2012) (Fig. 6a). The eastern edge of the Andes as marked by active faults correlates spatially with the western edge of the distinct, stable, largely cratonic interior of the South America plate. Thus, the general but imperfect coincidence of the hurdle with the active backthrust, where present, is consistent with the hurdle being determined by a contrast in compliance that occurs with different amplitudes and different depth dependences along the orogen.

In Sunda, the overriding plate is a set of Paleozoic-Cenozoic accreted terranes (Hall et al., 2009). We are unaware of independent proof that Sundaland is mechanically stiffer than the Sumatra forearc. However, a significant crustal contrast exists across the Meratus paleosuture in Java (Fig. 6b; Haberland et al., 2014). Contrasts may also exist across two major structural boundaries. The first of these is peninsular Malaysia's Bentong-Raub suture zone, which separates the Sibumasu terrane to its southwest from the Indochina terrane (Metcalfe, 2000). The second boundary is the Medial Sumatra Tectonic Zone, which separates the Sibumasu terrane to the northeast from the

West Sumatra block and the overlying Woyla accretionary complex and volcanic arc (Hutchison, 1994, 2014; Barber, 2000; Barber et al., 2005) and which largely coincides with the strike-slip Sumatran Fault in central and northern Sumatra. Simons et al. (2007) used GNSS data to identify the approximate boundaries of the interseismically nondeforming part of the Sundaland block (Michel et al., 2001); its internal (south and west) boundary aligns roughly with geological suture boundaries. On the other hand, estimates from coherence between gravity and topography show no evidence of a block in the interior of the plate with higher T_e than the forearc region (Audet & Bürgmann, 2011; Shi et al., 2017).

To explain the steep spatial gradient near the trench in horizontal interseismic velocities in Hokkaido, Japan, Itoh et al. (2019, 2021) proposed and modeled the effect of a compliant (less stiff or thinner) lithosphere in the volcanic arc and back-arc, in contrast with a less compliant (thicker) forearc, as evidenced by temperature, heat flux, and seismic wave attenuation (Katsumata et al., 2006; Kita et al., 2014; Liu et al., 2013; Tanaka et al., 2004; Wada & Wang, 2009; Wang & Zhao, 2005). However, in the model of Itoh et al. (2019) velocities are restricted by the fixed landward edge of the domain, which localizes shortening and shearing in the compliant material. We propose that velocities are instead restricted by the contrast between the compliant arc and back-arc and the less compliant material farther from the trench, in the Sea of Japan and beyond. The Sea of Japan is a Miocene back-arc basin of the Japan and southern Kurile subduction zones. It is inactive (Karig, 1974), having ceased extending around 14 Mya (Tatsumi et al., 1989), and is likely less compliant than the Japan arc. The Amurian-Okhotsk plate boundary follows the sea's eastern margin (Seno et al., 1996) (Fig. 6c), hosts M_w 7.6-7.8 thrust earthquakes (Satake, 1986; Sato et al., 1986; Tanioka et al., 1995) and accommodates a relative velocity of 9-17 mm/yr (Jin et al., 2007). The plate boundary mechanically decouples these plates in the long term, but they are coupled during most of the earthquake cycle. The lack of GNSS observations in the Sea of Japan prevents us from determining where exactly the compliance contrast occurs and whether creep along the plate boundary further affects velocities.

5.4 Compliance contrasts in a rheological and geodynamic context

As stated in Section 4.4, our model results suggest that interseismic velocities might necessitate a larger contrast in interseismic compliance within the overriding plate than can be provided by realistic elastic parameters. Concretely, the Young's modulus needs to be high enough in the portion of the plate between the trench and the hurdle as to transmit substantial coseismic displacement to the far-field, and low enough in the far-field interior of the plate as to not exceed plausible values. The portion of the plate between the trench and hurdle must thus transition from its greater coseismic compliance, dictated by elastic properties, to lesser compliance in the interseismic period. This transition might be related to viscous creep of the lower crust and upper mantle (Bürgmann & Dresen, 2008), which reduces flexural rigidity (Ranalli, 1995), and likely also compliance, over time after loading. Low effective elastic thickness is thought to indicate departure from purely elastic rheology, such as due to high temperatures, inherited weak zones, or high horizontal stresses (Burov & Diament, 1995), which are likely to occur in the thermomechanically young lithosphere at convergent boundaries. The increased water content at subduction zones also contributes to departure from elasticity by weakening the lower crust and upper mantle, in terms of both lower viscosity (Kirby, 1983; Chopra & Paterson, 1984; Hirth & Kohlstedt, 1996) and lower plastic strength (Blacic & Christie, 1984; Mainprice & Paterson, 1984). Geodynamical, petrological–thermomechanical numerical modeling of subduction shows that brittle-plastic rheological weakening by both fluids and melts plays an important role in the evolution of the subduction zone and in the development of the volcanic arc and the back-arc region (Gerya & Meilick, 2011).

5.5 Geodetically stable parts of overriding plates?

Observations of significant coseismic displacements thousands of km away from the megathrust rupture called into question the concept of an undeforming (rigid) reference plate (Pollitz et al., 2011a; Vigny et al., 2005; Wang et al., 2011; see also Section 4.1). Our analysis suggests indeed that small but non-zero interseismic velocities and velocity gradients extend beyond the hurdles, and this presents a challenge for defining a reference on a geodetic observation time scale. On time scales spanning the time needed to complete a seismic catalog on the megathrust (tens to thousands of years, e.g., Ward 1998), it is possible that the net accumulated strain is zero, i.e., there may exist a fully rigid reference on geological time scales.

5.6 Role of major faults in the Central Andes

As discussed in Section 2.6, previous studies observe and explain the spatial behavior of interseismic velocities, in the context of the Central Andes, as a result of shortening on back-thrusts (Norabuena et al., 1998; Bevis et al., 2001; Brooks et al., 2003, 2011; Kendrick et al., 2006; Weiss et al., 2016; McFarland et al., 2017; Shi et al., 2020). Quantitative models in these studies use either a uniform elastic half-space, or apply zero-displacement boundary conditions close to the back-thrust. Both model types artificially restrict interseismic velocities to the near-trench region, compared to models with elastic plates overlying viscoelastic mantle and extending well into the far-field. To explain the observed interseismic surface velocities, most of the studies also need basal thrusts that are more spatially extensive than supported by geological evidence (see Section 2.6). However, localized shortening has a more regional role in determining specific trench-perpendicular velocities, particularly in back-arc thrust belts and basal faults and in thrusts in the interior of orogens at the active margin. For instance, when these faults only decouple the shallow lithosphere, they may locally cause discontinuities and increased spatial gradients, without affecting the near-trench portion of the velocity field (Shi et al., 2020). Major, creeping strike-slip faults likely cause large local gradients in trench-parallel velocities, and can localize trench-parallel velocities in a way not necessarily related to the presence of a contrast (Section 2.6). Nevertheless, contrasts in lithologies and plate thickness, responsible for hurdles, might also result from continued motion along strike-slip faults. In turn, the presence of such contrasts might localize lateral motion into narrow fault zones.

6 Conclusions

Interseismic GNSS velocities from the three studied subduction zones show a broadly linear decrease of the trench-perpendicular velocity with distance from the trench up to what we define as the hurdle, located at variable distances less than 1000 km. Beyond the hurdle, trench-perpendicular velocities are near-zero (less than ~5 mm/yr) extending over thousands of kilometers away from the trench. Trench-parallel velocities are in some cases affected by presence of strike-slip faults (Sumatra), or are insignificant because of head-on convergence (Japan, Java). In South America, however, they generally also decrease steeply with distance, up to a hurdle. The hurdle roughly coincides with the trench-perpendicular hurdle or is located up to several tens of km closer to the trench. This interseismic deformation restricted to the near-trench region contrasts with significant coseismic displacements that were recorded beyond these hurdles during the large 2004 Sumatra, 2010 Maule and 2011 Tohoku earthquakes.

The location of the hurdle in observed trench-perpendicular velocities often coincides with major tectonic or geological boundaries separating a plate margin region from a distinct, and likely more rigid, plate interior. In South America the trench-perpendicular hurdle generally follows the eastern edge of the orogen, coinciding with the western margin of the cratonic lithosphere and the eastern margin of the accreted, deformed terranes at the active plate margin. In Sumatra, the hurdle follows the Medial Sumatra Tectonic Zone. Off the shore of northern Honshu and Hokkaido in Japan, the hurdle probably coincides with the boundary between the back-arc region of the islands, to the east, and the inactive back-arc basin and Amur plate interior to the west.

Our numerical modeling results show that a contrast in overriding plate compliance can reproduce the steep, largely linear near-trench decrease in trench-perpendicular velocities with distance. In our models, this decrease ends abruptly at the location of the contrast, i.e., at the hurdle. The value of elastic moduli on either side of the contrast determines the contrast amplitude and thus affects the intensity of the hurdle behavior: a weaker contrast steepens the near-trench slope and/or makes the far-field slope more shallow. Strengthening the contrast by decreasing the near-trench elastic moduli has a greater effect on trench-perpendicular velocities than increasing the far-field moduli, but higher far-field moduli are still important in introducing and defining the hurdle behavior. In contrast, trench-parallel velocities are controlled only by the near-trench elastic moduli and decrease more gradually. The steep decrease in the first couple of hundred km from the trench defines an apparent hurdle that, for the values tested in our models, is closer to the trench than the location of the contrast. The distance between the two depends on the specific elastic moduli and the location of their contrast.

The presence and location of compliance contrasts does not significantly affect the rate at which shear traction increases on the asperities in our models. The width of the zone where interseismic strain primarily accumulates, roughly between the coastline and the hurdle, likely does not generate significant variations in megathrust earthquake magnitude or recurrence interval. Velocities in portions of the subduction zone with little slip deficit, i.e., little apparent interplate coupling on the megathrust, have lower near-trench trench-perpendicular gradients but otherwise similar behavior, particularly in the trench-perpendicular components. Their near-trench trench-parallel components exhibit more complex gradients depending on location with respect to the fully coupled asperities and the direction of trench-parallel, far-field interplate motion.

Acknowledgments

We thank the following people for providing additional background information for the velocity data sets that we have used in this study: Laura Sánchez, Jean-Mathieu Nocquet, Corné Kreemer and Achraf Koulali. Insightful reviews by Kelin Wang, Emilie Klein and two anonymous reviewers contributed significantly to the improvement of earlier versions of the manuscript.

Author contributions following the CRediT taxonomy: Conceptualization: R. Govers, T. Broerse, M. D'Acquisto. Methodology: T. Broerse, M. D'Acquisto. Software: R. Govers, T. Broerse. Validation: T. Broerse, M. D'Acquisto. Formal Analysis: M. D'Acquisto, T. Broerse. Investigation: M. D'Acquisto, C. P. Marsman. Resources: R. Govers. Data Curation: M. D'Acquisto. Writing-Original Draft: M. D'Acquisto, R. Govers, T. Broerse , C. P. Marsman. Writing-Review & Editing: M. D'Acquisto, T. Broerse, R. Govers, C. P. Marsman. Visualization: M. D'Acquisto, T. Broerse. Supervision: R. Govers. Project Administration: R. Govers. Funding Acquisition: R. Govers.

The mesh generator program Gmsh (Geuzaine & Remacle, 2009) was used to make the finite element meshes for the numerical models. The MATLAB software platform (MATLAB, 2018), the Generic Mapping Tools (Wessel et al., 2019), and the Adobe Illustrator program (Adobe Inc., 2019) were used for visualization.

Data availability

The model output files that we used for the figures of this paper are digitally stored in the Yoda repository of Utrecht University and are freely available under the CC-BY license at https://doi.org/10.24416/UU01-6SC8XG .

References

Adobe Inc. (2019, April 1). Adobe Illustrator (Version CC 2019 (23.0.3)). Retrieved from https://adobe.com/products/illustrator

Agata, R., Barbot, S. D., Fujita, K., Hyodo, M., Iinuma, T., Nakata, R., Ichimura, T., & Hori, T. (2019). Rapid mantle flow with power-law creep explains deformation after the 2011 Tohoku mega-quake. *Nature Communications*, *10*(1), 1–11. doi:10.1038/s41467-019-08984-7

Altamimi, Z., Collilieux, X., & Métivier, L. (2011). ITRF2008: an improved solution of the international terrestrial reference frame. *Journal of Geodesy*, *85*(8), 457–473. doi:10.1007/s00190-011-0444-4

Altamimi, Z., Métivier, L., & Collilieux, X. (2012a). ITRF2008 plate motion model: ITRF2008 PLATE MOTION MODEL. *Journal of Geophysical Research: Solid Earth*, *117*(B7), n/a-n/a. doi:10.1029/2011JB008930

Altamimi, Z., Métivier, L., & Collilieux, X. (2012b). ITRF2008 plate motion model: ITRF2008 PLATE MOTION MODEL. *Journal of Geophysical Research: Solid Earth*, *117*(B7), n/a-n/a. doi:10.1029/2011JB008930

Alvarado, A., Audin, L., Nocquet, J. M., Lagreulet, S., Segovia, M., Font, Y., Lamarque, G., Yepes, H., Mothes, P., Rolandone, F., Jarrín, P., & Quidelleur, X. (2014a). Active tectonics in Quito, Ecuador, assessed by geomorphological studies, GPS data, and crustal seismicity. *Tectonics*, *33*(2), 67–83. doi:10.1002/2012TC003224

Alvarado, A., Audin, L., Nocquet, J. M., Lagreulet, S., Segovia, M., Font, Y., Lamarque, G., Yepes, H., Mothes, P., Rolandone, F., Jarrín, P., & Quidelleur, X. (2014b). Active tectonics in Quito, Ecuador, assessed by geomorphological studies, GPS data, and crustal seismicity. *Tectonics*, *33*(2), 67–83. doi:10.1002/2012TC003224

Alvarado, A., Audin, L., Nocquet, J. M., Jaillard, E., Mothes, P., Jarrín, P., Segovia, M., Rolandone, F., & Cisneros, D. (2016). Partitioning of oblique convergence in the Northern Andes subduction zone: Migration history and the present-day boundary of the North Andean Sliver in Ecuador. *Tectonics*, *35*(5), 1048–1065. doi:10.1002/2016TC004117

Alvarado, P., & Ramos, V. A. (2011). Earthquake deformation in the northwestern Sierras Pampeanas of Argentina based on seismic waveform modelling. *Journal of Geodynamics*, *51*(4), 205–218. doi:10.1016/j.jog.2010.08.002

Álvarez, O., Gimenez, M., Braitenberg, C., & Folguera, A. (2012). GOCE satellite derived gravity and gravity gradient corrected for topographic effect in the South Central Andes region. *Geophysical Journal International*, *190*(2), 941–959. doi:10.1111/j.1365-246X.2012.05556.x

Aoki, I., & Takahashi, E. (2004). Density of MORB eclogite in the upper mantle. *Physics of the Earth and Planetary Interiors*, *143–144*, 129–143. doi:10.1016/j.pepi.2003.10.007

Apel, E. V., Bürgmann, R., Steblov, G., Vasilenko, N., King, R., & Prytkov, A. (2006a). Independent active microplate tectonics of northeast Asia from GPS velocities and block modeling. *Geophysical Research Letters*, *33*(11), 2006GL026077. doi:10.1029/2006GL026077

Apel, E. V., Bürgmann, R., Steblov, G., Vasilenko, N., King, R., & Prytkov, A. (2006b). Independent active microplate tectonics of northeast Asia from GPS velocities and block modeling. *Geophysical Research Letters*, *33*(11), 2006GL026077. doi:10.1029/2006GL026077

Aron, F., Cembrano, J., Astudillo, F., Allmendinger, R. W., & Arancibia, G. (2015). Constructing forearc architecture over megathrust seismic cycles: Geological snapshots from the Maule earthquake region, Chile. *GSA Bulletin*, *127*(3–4), 464–479. doi:10.1130/B31125.1

Audet, P., & Bürgmann, R. (2011). Dominant role of tectonic inheritance in supercontinent cycles. *Nature Geoscience*, *4*(3), 184–187. doi:10.1038/ngeo1080

Balay, S., Gropp, W. D., McInnes, L. C., & Smith, B. F. (1997). Efficient management of parallelism in object oriented numerical software libraries. In E. Arge, A. M. Bruaset, & H. P. Langtangen (Eds.), *Modern software tools in scientific computing* (pp. 163–202). Birkhäuser Press.

Balay, S., Abhyankar, S., Adams, M. F., Benson, S., Brown, J., Brune, P., Buschelman, K., Constantinescu, E. M., Dalcin, L., Dener, A., Eijkhout, V., Gropp, W. D., Hapla, V., Isaac, T., Jolivet, P., Karpeev, D., Kaushik, D., Knepley, M. G., Kong, F., Kruger, S., May, D. A., McInnes, L. C., Mills, R. T., Mitchell, L., Munson, T., Roman, J. E., Rupp, K., Sanan, P., Sarich, J., Smith, B. F., Zampini, S., Zhang, H., Zhang, H., & Zhang, J. (2021). PETSc Web page. Retrieved April 30, 2022, from https://petsc.org/

Balay, S., Abhyankar, S., Adams, M. F., Benson, S., Brown, J., Brune, P., Buschelman, K., Constantinescu, E., Dalcin, L., Dener, A., Eijkhout, V., Gropp, W. D., Hapla, V., Isaac, T., Jolivet, P., Karpeev, D., Kaushik, D., Knepley, M. G., Kong, F., Kruger, S., May, D. A., McInnes, L. C., Mills, R. T., Mitchell, L., Munson, T., Roman, J. E., Rupp, K., Sanan, P., Sarich, J., Smith, B. F., Zampini, S., Zhang, H., Zhang, H., & Zhang, J. (2021). *PETSc/TAO users manual* (No. ANL-21/39-Revision 3.16). Argonne National Laboratory.

Baldis, B. A., Beresi, M., Bordonaro, O., & Vaca, A. (1982). Síntesis evolutiva de la Precordillera Argentina. In *Actas* (Vol. 4, pp. 399–445). Buenos Aires, Argentina: Servicio Geológico Nacional, Subsecretaría de Minería.

Barber, A. J. (2000). The origin of the Woyla Terranes in Sumatra and the Late Mesozoic evolution of the Sundaland margin. *Journal of Asian Earth Sciences*, *18*(6), 713–738. doi:10.1016/S1367-9120(00)00024-9

Barber, A. J., Crow, M. J., & Milsom, J. (2005). *Sumatra: Geology, Resources and Tectonic Evolution*. Geological Society of London.

Bevis, M., Kendrick, E., Smalley, R., Brooks, B., Allmendinger, R., & Isacks, B. (2001). On the strength of interplate coupling and the rate of back arc convergence in the central Andes: An analysis of the interseismic velocity field. *Geochemistry, Geophysics, Geosystems*, *2*(11). doi:https://doi.org/10.1029/2001GC000198

Bird, P. (2003). An updated digital model of plate boundaries. *Geochemistry, Geophysics, Geosystems*, *4*(3). doi:10.1029/2001GC000252

Blacic, J. D., & Christie, J. M. (1984). Plasticity and hydrolytic weakening of quartz single crystals. *Journal of Geophysical Research: Solid Earth*, *89*(B6), 4223–4239. doi:10.1029/JB089iB06p04223

Blewitt, G., Kreemer, C., Hammond, W. C., & Gazeaux, J. (2016). MIDAS robust trend estimator for accurate GPS station velocities without step detection. *Journal of Geophysical Research: Solid Earth*, *121*(3), 2054–2068. doi:10.1002/2015JB012552

Bock, Y., Prawirodirdjo, L., Genrich, J. F., Stevens, C. W., McCaffrey, R., Subarya, C., Puntodewo, S. S. O., & Calais, E. (2003). Crustal motion in Indonesia from Global

Positioning System measurements. *Journal of Geophysical Research: Solid Earth*, *108*(B8). doi:10.1029/2001JB000324

Broerse, T., Riva, R., Simons, W., Govers, R., & Vermeersen, B. (2015). Postseismic GRACE and GPS observations indicate a rheology contrast above and below the Sumatra slab. *Journal of Geophysical Research: Solid Earth*, *120*(7), 5343–5361. doi:10.1002/2015JB011951

Brooks, B. A., Bevis, M., Smalley, R., Kendrick, E., Manceda, R., Lauría, E., Maturana, R., & Araujo, M. (2003). Crustal motion in the Southern Andes (26°–36°S): Do the Andes behave like a microplate? *Geochemistry, Geophysics, Geosystems*, *4*(10). doi:https://doi.org/10.1029/2003GC000505

Brooks, B. A., Bevis, M., Whipple, K., Ramon Arrowsmith, J., Foster, J., Zapata, T., Kendrick, E., Minaya, E., Echalar, A., Blanco, M., Euillades, P., Sandoval, M., & Smalley, R. J. (2011). Orogenic-wedge deformation and potential for great earthquakes in the central Andean backarc. *Nature Geoscience*, *4*(6), 380–383. doi:10.1038/ngeo1143

Bürgmann, R., & Dresen, G. (2008). Rheology of the Lower Crust and Upper Mantle: Evidence from Rock Mechanics, Geodesy, and Field Observations. *Annual Review of Earth and Planetary Sciences*, *36*(1), 531–567. doi:10.1146/annurev.earth.36.031207.124326

Burov, E. B., & Diament, M. (1995). The effective elastic thickness (T e) of continental lithosphere: What does it really mean? *Journal of Geophysical Research: Solid Earth*, *100*(B3), 3905–3927. doi:10.1029/94JB02770

Cambiotti, G. (2020). Joint estimate of the coseismic 2011 Tohoku earthquake fault slip and post-seismic viscoelastic relaxation by GRACE data inversion. *Geophysical Journal International*, *220*(2), 1012–1022. doi:10.1093/gji/ggz485

Chlieh, M., De Chabalier, J. B., Ruegg, J. C., Armijo, R., Dmowska, R., Campos, J., & Feigl, K. L. (2004). Crustal deformation and fault slip during the seismic cycle in the North Chile subduction zone, from GPS and InSAR observations. *Geophysical Journal International*, *158*(2), 695–711. doi:10.1111/j.1365-246X.2004.02326.x

Chlieh, M., Avouac, J. P., Sieh, K., Natawidjaja, D. H., & Galetzka, J. (2008). Heterogeneous coupling of the Sumatran megathrust constrained by geodetic and paleogeodetic measurements. *Journal of Geophysical Research: Solid Earth*, *113*(B5). doi:10.1029/2007JB004981

Chopra, P. N., & Paterson, M. S. (1984). The role of water in the deformation of dunite. *Journal of Geophysical Research: Solid Earth*, *89*(B9), 7861–7876. doi:10.1029/JB089iB09p07861

Christensen, N. I. (1996). Poisson's ratio and crustal seismology. *Journal of Geophysical Research: Solid Earth*, *101*(B2), 3139–3156. doi:https://doi.org/10.1029/95JB03446

Chulick, G. S., Detweiler, S., & Mooney, W. D. (2013). Seismic structure of the crust and uppermost mantle of South America and surrounding oceanic basins. *Journal of South American Earth Sciences*, *42*, 260–276. doi:10.1016/j.jsames.2012.06.002

Cisneros, D., & Nocquet, J. (2011). Campo de velocidades del Ecuador, obtenido a través de mediciones de campañes GPS de los ultimos 15 años y medidas de une red GPS permanente. Retrieved from https://www.sirgas.org/fileadmin/docs/Cisneros_2010_Campo_velocidades_Ecuador_web.pdf

Conn, A. R., Gould, N. I. M., & Toint, P. L. (2000). *Trust Region Methods*. SIAM.

Delouis, B., Nocquet, J.-M., & Vallée, M. (2010). Slip distribution of the February 27, 2010 Mw = 8.8 Maule Earthquake, central Chile, from static and high-rate GPS, InSAR, and broadband teleseismic data. *Geophysical Research Letters*, *37*(17). doi:10.1029/2010GL043899

Diao, F., Xiong, X., Wang, R., Zheng, Y., Walter, T. R., Weng, H., & Li, J. (2014). Overlapping post-seismic deformation processes: afterslip and viscoelastic relaxation following the 2011 Mw 9.0 Tohoku (Japan) earthquake. *Geophysical Journal International*, *196*(1), 218–229. doi:10.1093/gji/ggt376

Drewes, H., & Heidbach, O. (2012a). The 2009 Horizontal Velocity Field for South America and the Caribbean. In S. Kenyon, M. C. Pacino, & U. Marti (Eds.), *Geodesy for Planet Earth* (Vol. 136, pp. 657–664). Berlin, Heidelberg: Springer Berlin Heidelberg. doi:10.1007/978-3-642-20338-1_81

Drewes, H., & Heidbach, O. (2012b). The 2009 Horizontal Velocity Field for South America and the Caribbean. In S. Kenyon, M. C. Pacino, U. Marti, S. Kenyon, M. C. Pacino, & U. Marti (Eds.), *Geodesy for Planet Earth* (Vol. 136, pp. 657–664). Berlin, Heidelberg. Retrieved from http://link.springer.com/10.1007/978-3-642-20338-1_81

Driscoll, T. A. (2002). *Schwarz-Christoffel Mapping* (1st edition). Cambridge ; New York: Cambridge University Press.

Dziewonski, A. M., & Anderson, D. L. (1981). Preliminary reference Earth model. *Physics of the Earth and Planetary Interiors*, *25*(4), 297–356. doi:10.1016/0031-9201(81)90046-7

Fitch, T. J. (1972). Plate convergence, transcurrent faults, and internal deformation adjacent to Southeast Asia and the western Pacific. *Journal of Geophysical Research (1896-1977)*, *77*(23), 4432–4460. doi:10.1029/JB077i023p04432

Fouedjio, F., & Séguret, S. (2016). Predictive Geological Mapping Using Closed-Form Non-stationary Covariance Functions with Locally Varying Anisotropy: Case Study at El Teniente Mine (Chile). *Natural Resources Research*, *25*(4), 431–443. doi:10.1007/s11053-016-9293-4

Freed, A. M., Hashima, A., Becker, T. W., Okaya, D. A., Sato, H., & Hatanaka, Y. (2017). Resolving depth-dependent subduction zone viscosity and afterslip from postseismic displacements following the 2011 Tohoku-oki, Japan earthquake. *Earth and Planetary Science Letters*, *459*, 279–290. doi:10.1016/j.epsl.2016.11.040

Fujiwara, T., Kodaira, S., No, T., Kaiho, Y., Takahashi, N., & Kaneda, Y. (2011). The 2011 Tohoku-Oki Earthquake: Displacement Reaching the Trench Axis. *Science*, *334*(6060), 1240–1240. doi:10.1126/science.1211554

Fukuda, J., & Johnson, K. M. (2021). Bayesian Inversion for a Stress-Driven Model of Afterslip and Viscoelastic Relaxation: Method and Application to Postseismic Deformation Following the 2011 MW 9.0 Tohoku-Oki Earthquake. *Journal of Geophysical Research: Solid Earth*, *126*(5), e2020JB021620. doi:10.1029/2020JB021620

Furlong, K. P., & Govers, R. (1999). Ephemeral crustal thickening at a triple junction:The Mendocino crustal conveyor. *Geology*, *27*(2), 127–130. doi:10.1130/0091-7613(1999)027<0127:ECTAAT>2.3.CO;2

Gabriel, E., Fagg, G. E., Bosilca, G., Angskun, T., Dongarra, J. J., Squyres, J. M., Sahay, V., Kambadur, P., Barrett, B., Lumsdaine, A., Castain, R. H., Daniel, D. J., Graham, R. L., & Woodall, T. S. (2004). Open MPI: Goals, Concept, and Design of a Next Generation MPI Implementation. In D. Kranzlmüller, P. Kacsuk, & J. Dongarra (Eds.), *Recent Advances* *in Parallel Virtual Machine and Message Passing Interface* (Vol. 3241, pp. 97–104). Berlin, Heidelberg: Springer Berlin Heidelberg. doi:10.1007/978-3-540-30218-6_19

Gagnon, K., Chadwell, C. D., & Norabuena, E. (2005a). Measuring the onset of locking in the Peru–Chile trench with GPS and acoustic measurements. *Nature*, *434*(7030), 205–208. doi:10.1038/nature03412

Gagnon, K., Chadwell, C. D., & Norabuena, E. (2005b). Measuring the onset of locking in the Peru–Chile trench with GPS and acoustic measurements. *Nature*, *434*(7030), 205–208. doi:10.1038/nature03412

Gahalaut, V. K., Jade, S., Catherine, J. K., Gireesh, R., Ananda, M. B., Kumar, P., Narsaiah, M., Jafri, S. S. H., Ambikapathy, A., Bansal, A., Chadha, R. K., Gupta, D. C., Nagarajan, B., & Kumar, S. (2008). GPS measurements of postseismic deformation in the Andaman-Nicobar region following the giant 2004 Sumatra-Andaman earthquake. *Journal of Geophysical Research: Solid Earth*, *113*(B8). doi:10.1029/2007JB005511

Genrich, J. F., Bock, Y., McCaffrey, R., Prawirodirdjo, L., Stevens, C. W., Puntodewo, S. S. O., Subarya, C., & Wdowinski, S. (2000a). Distribution of slip at the northern Sumatran fault system. *Journal of Geophysical Research: Solid Earth*, *105*(B12), 28327–28341. doi:10.1029/2000JB900158

Genrich, J. F., Bock, Y., McCaffrey, R., Prawirodirdjo, L., Stevens, C. W., Puntodewo, S. S. O., Subarya, C., & Wdowinski, S. (2000b). Distribution of slip at the northern Sumatran fault system. *Journal of Geophysical Research: Solid Earth*, *105*(B12), 28327–28341. doi:10.1029/2000JB900158

Gerya, T. V., & Meilick, F. I. (2011). Geodynamic regimes of subduction under an active margin: effects of rheological weakening by fluids and melts. *Journal of Metamorphic Geology*, *29*(1), 7–31. doi:https://doi.org/10.1111/j.1525-1314.2010.00904.x

Geuzaine, C., & Remacle, J.-F. (2009). Gmsh: A 3-D finite element mesh generator with built-in pre- and post-processing facilities. *International Journal for Numerical Methods in Engineering*, *79*(11), 1309–1331. doi:10.1002/nme.2579

Govers, R., & Wortel, R. (1993). Initiation of asymmetric extension in continental lithosphere. *Tectonophysics*, *223*(1), 75–96. doi:10.1016/0040-1951(93)90159-H

Govers, R., & Wortel, R. (2005). Lithosphere tearing at STEP faults: response to edges of subduction zones. *Earth and Planetary Science Letters*, *236*(1), 505–523. doi:10.1016/j.epsl.2005.03.022

Govers, R., Furlong, K. P., van de Wiel, L., Herman, M. W., & Broerse, T. (2018). The Geodetic Signature of the Earthquake Cycle at Subduction Zones: Model Constraints on the Deep Processes. *Reviews of Geophysics*, *56*(1), 6–49. doi:10.1002/2017RG000586

Haberland, C., Bohm, M., & Asch, G. (2014). Accretionary nature of the crust of Central and East Java (Indonesia) revealed by local earthquake travel-time tomography. *Journal of Asian Earth Sciences*, *96*, 287–295. doi:10.1016/j.jseaes.2014.09.019

Hall, R., & Sevastjanova, I. (2012). Australian crust in Indonesia. *Australian Journal of Earth Sciences*, *59*(6), 827–844. doi:10.1080/08120099.2012.692335

Hall, R., Clements, B., & Smyth, H. R. (2009). Sundaland: Basement Character, Structure and Plate Tectonic Development. *PROCEEDINGS, INDONESIAN PETROLEUM ASSOCIATION*, *33rd Annual Convention, 2009*.

Hardebeck, J. L. (2015). Stress orientations in subduction zones and the strength of subduction megathrust faults. *Science*, *349*(6253), 1213–1216. doi:10.1126/science.aac5625

Hashimoto, C., Noda, A., Sagiya, T., & Matsu'ura, M. (2009). Interplate seismogenic zones along the Kuril–Japan trench inferred from GPS data inversion. *Nature Geoscience*, *2*(2), 141–144. doi:10.1038/ngeo421

Hayes, G. P., Moore, G. L., Portner, D. E., Hearne, M., Flamme, H., Furtney, M., & Smoczyk, G. M. (2018). Slab2, a comprehensive subduction zone geometry model. *Science*, *362*(6410), 58–61. doi:10.1126/science.aat4723

Herman, M. W., & Govers, R. (2020). Locating Fully Locked Asperities Along the South America Subduction Megathrust: A New Physical Interseismic Inversion Approach in a Bayesian Framework. *Geochemistry, Geophysics, Geosystems*, *21*(8). doi:10.1029/2020GC009063

Hirth, G., & Kohlstedt, D. L. (1996). Water in the oceanic upper mantle: implications for rheology, melt extraction and the evolution of the lithosphere. *Earth and Planetary Science Letters*, *144*(1), 93–108. doi:10.1016/0012-821X(96)00154-9

Hu, Y., & Wang, K. (2012). Spherical-Earth finite element model of short-term postseismic deformation following the 2004 Sumatra earthquake. *Journal of Geophysical Research: Solid Earth*, *117*(B5). doi:10.1029/2012JB009153

Hu, Y., Bürgmann, R., Uchida, N., Banerjee, P., & Freymueller, J. T. (2016). Stress-driven relaxation of heterogeneous upper mantle and time-dependent afterslip following the 2011 Tohoku earthquake. *Journal of Geophysical Research: Solid Earth*, *121*(1), 385–411. doi:10.1002/2015JB012508

Hutchison, C. S. (1994). Gondwana and Cathaysian blocks, Palaeotethys sutures and Cenozoic tectonics in South-east Asia. In P. Giese & J. Behrmann (Eds.), *Active Continental Margins — Present and Past* (pp. 388–405). Berlin, Heidelberg: Springer. doi:10.1007/978-3-662-38521-0_14

Hutchison, C. S. (2014). Tectonic evolution of Southeast Asia, *60*, 18.

Ikari, M. J., Marone, C., & Saffer, D. M. (2011). On the relation between fault strength and frictional stability. *Geology*, *39*(1), 83–86. doi:10.1130/G31416.1

Itoh, Y., Wang, K., Nishimura, T., & He, J. (2019). Compliant Volcanic Arc and Backarc Crust in Southern Kurile Suggested by Interseismic Geodetic Deformation. *Geophysical Research Letters*, *46*(21), 11790–11798. doi:10.1029/2019GL084656

Itoh, Y., Nishimura, T., Wang, K., & He, J. (2021). New Megathrust Locking Model for the Southern Kurile Subduction Zone Incorporating Viscoelastic Relaxation and Non-Uniform Compliance of Upper Plate. *Journal of Geophysical Research: Solid Earth*, *126*(5), e2020JB019981. doi:https://doi.org/10.1029/2020JB019981

Jin, S., & Park, P.-H. (2006a). Strain accumulation in South Korea inferred from GPS measurements. *Earth, Planets and Space*, *58*(5), 529–534. doi:10.1186/BF03351950

Jin, S., & Park, P.-H. (2006b). Strain accumulation in South Korea inferred from GPS measurements. *Earth, Planets and Space*, *58*(5), 529–534. doi:10.1186/BF03351950

Jin, S., Park, P.-H., & Zhu, W. (2007). Micro-plate tectonics and kinematics in Northeast Asia inferred from a dense set of GPS observations. *Earth and Planetary Science Letters*, *257*(3), 486–496. doi:10.1016/j.epsl.2007.03.011

Jordan, T. E., Isacks, B. L., Allmendinger, R. W., Brewer, J. A., Ramos, V. A., & Ando, C. J. (1983). Andean tectonics related to geometry of subducted Nazca plate. *GSA Bulletin*, *94*(3), 341–361. doi:10.1130/0016-7606(1983)94<341:ATRTGO>2.0.CO;2

Kanamori, H. (1972). Mechanism of tsunami earthquakes. *Physics of the Earth and Planetary Interiors*, *6*(5), 346–359. doi:10.1016/0031-9201(72)90058-1

Karig, D. E. (1974). Evolution of Arc Systems in the Western Pacific. *Annual Review of Earth and Planetary Sciences*, *2*(1), 51–75. doi:10.1146/annurev.ea.02.050174.000411

Katsumata, K., Wada, N., & Kasahara, M. (2006). Three-dimensional P and S wave velocity structures beneath the Hokkaido corner, Japan-Kurile arc-arc junction. *Earth, Planets and Space*, *58*(8), e37–e40. doi:10.1186/BF03352595

Kawakatsu, H., Kumar, P., Takei, Y., Shinohara, M., Kanazawa, T., Araki, E., & Suyehiro, K. (2009). Seismic Evidence for Sharp Lithosphere-Asthenosphere Boundaries of Oceanic Plates. *Science*, *324*(5926), 499–502. doi:10.1126/science.1169499

van Keken, P. E., Kiefer, B., & Peacock, S. M. (2002). High-resolution models of subduction zones: Implications for mineral dehydration reactions and the transport of water into the deep mantle. *Geochemistry, Geophysics, Geosystems*, *3*(10). doi:https://doi.org/10.1029/2001GC000256

Kellogg, J. N., Vega, V., Stailings, T. C., Aiken, C. L. V., & Kellogg, J. N. (1995). Tectonic development of Panama, Costa Rica, and the Colombian Andes: Constraints from Global Positioning System geodetic studies and gravity. *Geological Society of America Special Paper*, *295*, 75–90. doi:10.1130/SPE295-p75

Kendrick, E., Bevis, M., Smalley, R., & Brooks, B. (2001). An integrated crustal velocity field for the central Andes. *Geochemistry, Geophysics, Geosystems*, *2*(11). doi:https://doi.org/10.1029/2001GC000191

Kendrick, E., Brooks, B. A., Bevis, M., Jr, R. S., Lauria, E., Araujo, M., & Parra, H. (2006). Active orogeny of the south-central Andes studied with GPS geodesy. *Revista de La Asociación Geológica Argentina*, *61*(4), 555–566.

Khazaradze, G., & Klotz, J. (2003). Short- and long-term effects of GPS measured crustal deformation rates along the south central Andes: SHORT- AND LONG-TERM DEFORMATION ALONG THE ANDES. *Journal of Geophysical Research: Solid Earth*, *108*(B6). doi:10.1029/2002JB001879

Kirby, S. H. (1983). Rheology of the lithosphere. *Reviews of Geophysics*, *21*(6), 1458–1487. doi:10.1029/RG021i006p01458

Kita, S., Nakajima, J., Hasegawa, A., Okada, T., Katsumata, K., Asano, Y., & Kimura, T. (2014). Detailed seismic attenuation structure beneath Hokkaido, northeastern Japan: Arc-arc collision process, arc magmatism, and seismotectonics. *Journal of Geophysical Research: Solid Earth*, *119*(8), 6486–6511. doi:https://doi.org/10.1002/2014JB011099

Klein, E., Fleitout, L., Vigny, C., & Garaud, J. D. (2016). Afterslip and viscoelastic relaxation model inferred from the large-scale post-seismic deformation following the 2010 Mw 8.8 Maule earthquake (Chile). *Geophysical Journal International*, *205*(3), 1455–1472. doi:10.1093/gji/ggw086

Klein, E., Métois, M., Meneses, G., Vigny, C., & Delorme, A. (2018a). Bridging the gap between North and Central Chile: insight from new GPS data on coupling complexities and the Andean sliver motion. *Geophysical Journal International*, *213*(3), 1924–1933. doi:10.1093/gji/ggy094

Klein, E., Métois, M., Meneses, G., Vigny, C., & Delorme, A. (2018b). Bridging the gap between North and Central Chile: insight from new GPS data on coupling complexities and the Andean sliver motion. *Geophysical Journal International*, *213*(3), 1924–1933. doi:10.1093/gji/ggy094

Klotz, J., Khazaradze, G., Angermann, D., Reigber, C., Perdomo, R., & Cifuentes, O. (2001). Earthquake cycle dominates contemporary crustal deformation in Central and Southern Andes. *Earth and Planetary Science Letters*, *193*(3), 437–446. doi:10.1016/S0012-821X(01)00532-5

Koulali, A., McClusky, S., Susilo, S., Leonard, Y., Cummins, P., Tregoning, P., Meilano, I., Efendi, J., & Wijanarto, A. B. (2017). The kinematics of crustal deformation in Java from GPS observations: Implications for fault slip partitioning. *Earth and Planetary Science Letters*, *458*, 69–79. doi:10.1016/j.epsl.2016.10.039

Kreemer, C., Blewitt, G., & Klein, E. C. (2014). A geodetic plate motion and Global Strain Rate Model. *Geochemistry, Geophysics, Geosystems*, *15*(10), 3849–3889. doi:10.1002/2014GC005407

Kumar, P., & Kawakatsu, H. (2011). Imaging the seismic lithosphere-asthenosphere boundary of the oceanic plate. *Geochemistry, Geophysics, Geosystems*, *12*(1). doi:10.1029/2010GC003358

Li, S., Moreno, M., Bedford, J., Rosenau, M., & Oncken, O. (2015). Revisiting viscoelastic effects on interseismic deformation and locking degree: A case study of the Peru-North

Chile subduction zone. *Journal of Geophysical Research: Solid Earth*, *120*(6), 4522–4538. doi:10.1002/2015JB011903

Li, S., Bedford, J., Moreno, M., Barnhart, W. D., Rosenau, M., & Oncken, O. (2018). Spatiotemporal Variation of Mantle Viscosity and the Presence of Cratonic Mantle Inferred From 8 Years of Postseismic Deformation Following the 2010 Maule, Chile, Earthquake. *Geochemistry, Geophysics, Geosystems*, *19*(9), 3272–3285. doi:10.1029/2018GC007645

Li, S., Fukuda, J., & Oncken, O. (2020). Geodetic Evidence of Time-Dependent Viscoelastic Interseismic Deformation Driven by Megathrust Locking in the Southwest Japan Subduction Zone. *Geophysical Research Letters*, *47*(4). doi:10.1029/2019GL085551

Lin, Y. N., Sladen, A., Ortega-Culaciati, F., Simons, M., Avouac, J.-P., Fielding, E. J., Brooks, B. A., Bevis, M., Genrich, J., Rietbrock, A., Vigny, C., Smalley, R., & Socquet, A. (2013). Coseismic and postseismic slip associated with the 2010 Maule Earthquake, Chile: Characterizing the Arauco Peninsula barrier effect. *Journal of Geophysical Research: Solid Earth*, *118*(6), 3142–3159. doi:10.1002/jgrb.50207

Liu, X., Zhao, D., & Li, S. (2013). Seismic heterogeneity and anisotropy of the southern Kuril arc: insight into megathrust earthquakes. *Geophysical Journal International*, *194*(2), 1069–1090. doi:10.1093/gji/ggt150

Liu, Z., Owen, S., Dong, D., Lundgren, P., Webb, F., Hetland, E., & Simons, M. (2010a). Estimation of interplate coupling in the Nankai trough, Japan using GPS data from 1996 to 2006. *Geophysical Journal International*, *181*(3), 1313–1328. doi:https://doi.org/10.1111/j.1365-246X.2010.04600.x

Liu, Z., Owen, S., Dong, D., Lundgren, P., Webb, F., Hetland, E., & Simons, M. (2010b). Estimation of interplate coupling in the Nankai trough, Japan using GPS data from 1996 to 2006. *Geophysical Journal International*, *181*(3), 1313–1328. doi:10.1111/j.1365-246X.2010.04600.x

Loveless, J. P., & Meade, B. J. (2010). Geodetic imaging of plate motions, slip rates, and partitioning of deformation in Japan. *Journal of Geophysical Research*, *115*(B2), B02410. doi:10.1029/2008JB006248

Loveless, J. P., & Meade, B. J. (2011). Spatial correlation of interseismic coupling and coseismic rupture extent of the 2011 MW = 9.0 Tohoku-oki earthquake. *Geophysical Research Letters*, *38*(17). doi:10.1029/2011GL048561

Machuca-Mory, D. F., & Deutsch, C. V. (2013). Non-stationary Geostatistical Modeling Based on Distance Weighted Statistics and Distributions. *Mathematical Geosciences*, *45*(1), 31–48. doi:10.1007/s11004-012-9428-z

Mainprice, D. H., & Paterson, M. S. (1984). Experimental studies of the role of water in the plasticity of quartzites. *Journal of Geophysical Research: Solid Earth*, *89*(B6), 4257–4269. doi:10.1029/JB089iB06p04257

MATLAB. (2018). *R2018b*. Natick, Massachusetts: The MathWorks Inc.

Matsu'ura, M., & Sato, T. (1989). A dislocation model for the earthquake cycle at convergent plate boundaries. *Geophysical Journal International*, *96*(1), 23–32. doi:10.1111/j.1365-246X.1989.tb05247.x

McCaffrey, R. (1992). Oblique plate convergence, slip vectors, and forearc deformation. *Journal of Geophysical Research: Solid Earth*, *97*(B6), 8905–8915. doi:https://doi.org/10.1029/92JB00483

McCaffrey, R. (1996). Estimates of modern arc-parallel strain rates in fore arcs. *Geology*, *24*(1), 27–30. doi:10.1130/0091-7613(1996)024<0027:EOMAPS>2.3.CO;2

McFarland, P. K., Bennett, R. A., Alvarado, P., & DeCelles, P. G. (2017). Rapid Geodetic Shortening Across the Eastern Cordillera of NW Argentina Observed by the Puna-Andes GPS Array. *Journal of Geophysical Research*, 24. doi:10.1002/2017JB014739

McKenzie, K. A., & Furlong, K. P. (2021). Isolating non-subduction-driven tectonic processes in Cascadia. *Geoscience Letters*, *8*(1), 10. doi:10.1186/s40562-021-00181-z

Melosh, H. J., & Raefsky, A. (1981). A simple and efficient method for introducing faults into finite element computations. *Bulletin of the Seismological Society of America*, *71*(5), 1391–1400. doi:10.1785/BSSA0710051391

Melosh, H. J., & Raefsky, A. (1983). Anelastic response of the Earth to a dip slip earthquake. *Journal of Geophysical Research: Solid Earth*, *88*(B1), 515–526. doi:10.1029/JB088iB01p00515

Melosh, H. J., & Williams, C. A. (1989). Mechanics of graben formation in crustal rocks: A finite element analysis. *Journal of Geophysical Research: Solid Earth*, *94*(B10), 13961–13973. doi:10.1029/JB094iB10p13961

Meltzner, A. J., Sieh, K., Chiang, H.-W., Shen, C.-C., Suwargadi, B. W., Natawidjaja, D. H., Philibosian, B. E., Briggs, R. W., & Galetzka, J. (2010). Coral evidence for earthquake recurrence and an A.D. 1390–1455 cluster at the south end of the 2004 Aceh–Andaman rupture. *Journal of Geophysical Research: Solid Earth*, *115*(B10). doi:10.1029/2010JB007499

Metcalfe, I. (2000). The Bentong–Raub Suture Zone. *Journal of Asian Earth Sciences*, *18*(6), 691–712. doi:10.1016/S1367-9120(00)00043-2

Metcalfe, I. (2011). Tectonic framework and Phanerozoic evolution of Sundaland. *Gondwana Research*, *19*(1), 3–21. doi:10.1016/j.gr.2010.02.016

Métivier, L., Altamimi, Z., & Rouby, H. (2020). Past and present ITRF solutions from geophysical perspectives. *Advances in Space Research*, *65*(12), 2711–2722. doi:10.1016/j.asr.2020.03.031

Métois, M., Socquet, A., & Vigny, C. (2012). Interseismic coupling, segmentation and mechanical behavior of the central Chile subduction zone. *Journal of Geophysical Research: Solid Earth*, *117*(B3). doi:10.1029/2011JB008736

Métois, M., Socquet, A., Vigny, C., Carrizo, D., Peyrat, S., Delorme, A., Maureira, E., Valderas-Bermejo, M.-C., & Ortega, I. (2013). Revisiting the North Chile seismic gap segmentation using GPS-derived interseismic coupling. *Geophysical Journal International*, *194*(3), 1283–1294. doi:10.1093/gji/ggt183

Métois, M., Vigny, C., Socquet, A., Delorme, A., Morvan, S., Ortega, I., & Valderas-Bermejo, C.-M. (2014). GPS-derived interseismic coupling on the subduction and seismic hazards in the Atacama region, Chile. *Geophysical Journal International*, *196*(2), 644–655. doi:10.1093/gji/ggt418

Métois, M., Vigny, C., & Socquet, A. (2016). Interseismic Coupling, Megathrust Earthquakes and Seismic Swarms Along the Chilean Subduction Zone (38°–18°S). *Pure and Applied Geophysics*, *173*(5), 1431–1449. doi:10.1007/s00024-016-1280-5

Michel, G. W., Yu, Y. Q., Zhu, S. Y., Reigber, C., Becker, M., Reinhart, E., Simons, W., Ambrosius, B., Vigny, C., Chamot-Rooke, N., Le Pichon, X., Morgan, P., & Matheussen, S. (2001). Crustal motion and block behaviour in SE-Asia from GPS measurements.

Earth and Planetary Science Letters, *187*(3), 239–244. doi:10.1016/S0012-821X(01)00298-9

Moore, J. C., & Saffer, D. (2001). Updip limit of the seismogenic zone beneath the accretionary prism of southwest Japan: An effect of diagenetic to low-grade metamorphic processes and increasing effective stress. *Geology*, *29*(2), 183–186. doi:10.1130/0091-7613(2001)029<0183:ULOTSZ>2.0.CO;2

Moreno, M., Rosenau, M., & Oncken, O. (2010). 2010 Maule earthquake slip correlates with pre-seismic locking of Andean subduction zone. *Nature*, *467*(7312), 198–202. doi:10.1038/nature09349

Moreno, M., Melnick, D., Rosenau, M., Baez, J., Klotz, J., Oncken, O., Tassara, A., Chen, J., Bataille, K., Bevis, M., Socquet, A., Bolte, J., Vigny, C., Brooks, B., Ryder, I., Grund, V., Smalley, B., Carrizo, D., Bartsch, M., & Hase, H. (2012). Toward understanding tectonic control on the Mw 8.8 2010 Maule Chile earthquake. *Earth and Planetary Science Letters*, *321–322*, 152–165. doi:10.1016/j.epsl.2012.01.006

Mouthereau, F., Watts, A. B., & Burov, E. (2013). Structure of orogenic belts controlled by lithosphere age. *Nature Geoscience*, *6*(9), 785–789. doi:10.1038/ngeo1902

Muto, J., Moore, J. D. P., Barbot, S., Iinuma, T., Ohta, Y., & Iwamori, H. (2019). Coupled afterslip and transient mantle flow after the 2011 Tohoku earthquake. *Science Advances*, *5*(9), eaaw1164. doi:10.1126/sciadv.aaw1164

Nishimura, T. (2011a). Back-arc spreading of the northern Izu–Ogasawara (Bonin) Islands arc clarified by GPS data. *Tectonophysics*, *512*(1–4), 60–67. doi:10.1016/j.tecto.2011.09.022

Nishimura, T. (2011b). Back-arc spreading of the northern Izu–Ogasawara (Bonin) Islands arc clarified by GPS data. *Tectonophysics*, *512*(1–4), 60–67. doi:10.1016/j.tecto.2011.09.022

Nocquet, J.-M., Villegas-Lanza, J. C., Chlieh, M., Mothes, P. A., Rolandone, F., Jarrin, P., Cisneros, D., Alvarado, A., Audin, L., Bondoux, F., Martin, X., Font, Y., Régnier, M., Vallée, M., Tran, T., Beauval, C., Maguiña Mendoza, J. M., Martinez, W., Tavera, H., & Yepes, H. (2014). Motion of continental slivers and creeping subduction in the northern Andes. *Nature Geoscience*, *7*(4), 287–291. doi:10.1038/ngeo2099

Nocquet, J.-M., Jarrin, P., Vallée, M., Mothes, P. A., Grandin, R., Rolandone, F., Delouis, B., Yepes, H., Font, Y., Fuentes, D., Régnier, M., Laurendeau, A., Cisneros, D., Hernandez, S., Sladen, A., Singaucho, J.-C., Mora, H., Gomez, J., Montes, L., & Charvis, P. (2017). Supercycle at the Ecuadorian subduction zone revealed after the 2016 Pedernales earthquake. *Nature Geoscience*, *10*(2), 145–149. doi:10.1038/ngeo2864

Norabuena, E., Leffler-Griffin, L., Mao, A., Dixon, T., Stein, S., Sacks, I. S., Ocola, L., & Ellis, M. (1998). Space Geodetic Observations of Nazca-South America Convergence Across the Central Andes. *Science*, *279*(5349), 358–362. doi:10.1126/science.279.5349.358

Nostro, C., Piersanti, A., Antonioli, A., & Spada, G. (1999). Spherical versus flat models of coseismic and postseismic deformations. *Journal of Geophysical Research: Solid Earth*, *104*(B6), 13115–13134. doi:10.1029/1999JB900097

Ohzono, M., Sagiya, T., Hirahara, K., Hashimoto, M., Takeuchi, A., Hoso, Y., Wada, Y., Onoue, K., Ohya, F., & Doke, R. (2011a). Strain accumulation process around the Atotsugawa fault system in the Niigata-Kobe Tectonic Zone, central Japan. *Geophysical Journal International*, *184*(3), 977–990. doi:10.1111/j.1365-246X.2010.04876.x

Ohzono, M., Sagiya, T., Hirahara, K., Hashimoto, M., Takeuchi, A., Hoso, Y., Wada, Y., Onoue, K., Ohya, F., & Doke, R. (2011b). Strain accumulation process around the Atotsugawa fault system in the Niigata-Kobe Tectonic Zone, central Japan: Strain field around the

Atotsugawa fault system. *Geophysical Journal International*, *184*(3), 977–990. doi:10.1111/j.1365-246X.2010.04876.x

Ortiz, A., & Zambrano, J. J. (1981). La provincia geológica Precordillera Oriental. In *Actas* (Vol. 3, pp. 59–74). Buenos Aires, Argentina.

Pearson, D. M., Kapp, P., DeCelles, P. G., Reiners, P. W., Gehrels, G. E., Ducea, M. N., & Pullen, A. (2013). Influence of pre-Andean crustal structure on Cenozoic thrust belt kinematics and shortening magnitude: Northwestern Argentina. *Geosphere*, *9*(6), 1766–1782. doi:10.1130/GES00923.1

Perarnau, M., Gilbert, H., Alvarado, P., Martino, R., & Anderson, M. (2012). Crustal structure of the Eastern Sierras Pampeanas of Argentina using high frequency local receiver functions. *TECTONOPHYSICS*, *580*, 208–217. doi:10.1016/j.tecto.2012.09.021

Pérez-Gussinyé, M., Lowry, A. R., & Watts, A. B. (2007). Effective elastic thickness of South America and its implications for intracontinental deformation. *Geochemistry, Geophysics, Geosystems*, *8*(5). doi:https://doi.org/10.1029/2006GC001511

Pérez-Gussinyé, M., Lowry, A. R., Morgan, J. P., & Tassara, A. (2008). Effective elastic thickness variations along the Andean margin and their relationship to subduction geometry. *Geochemistry, Geophysics, Geosystems*, *9*(2). doi:https://doi.org/10.1029/2007GC001786

Petit, C., & Fournier, M. (2005). Present-day velocity and stress fields of the Amurian Plate from thin-shell finite-element modelling. *Geophysical Journal International*, *160*(1), 357–369. doi:10.1111/j.1365-246X.2004.02486.x

Pollitz, F. F., Thatcher, W. R., & Hearn, E. H. (2010). The resolution of mantle viscosity using nine years of GPS measurements following the 1999 M=7.1 Hector Mine, CA, earthquake (Invited). *AGU Fall Meeting Abstracts*, *51*, T51F-02.

Pollitz, F. F., Brooks, B., Tong, X., Bevis, M. G., Foster, J. H., Bürgmann, R., Smalley, R., Vigny, C., Socquet, A., Ruegg, J.-C., Campos, J., Barrientos, S., Parra, H., Soto, J. C. B., Cimbaro, S., & Blanco, M. (2011). Coseismic slip distribution of the February 27, 2010 Mw 8.8 Maule, Chile earthquake. *Geophysical Research Letters*, *38*(9). doi:https://doi.org/10.1029/2011GL047065

Pollitz, F. F., Bürgmann, R., & Banerjee, P. (2011). Geodetic slip model of the 2011 M9.0 Tohoku earthquake. *Geophysical Research Letters*, *38*(7). doi:10.1029/2011GL048632

Prawirodirdjo, L., Bocl, Y., McCaffrey, R., Genrich, J., Calais, E., Stevens, C., Puntodewo, S. S. O., Subarya, C., Rais, J., Zwick, P., & Fauzi, R. M. (1997). Geodetic observations of interseismic strain segmentation at the Sumatra Subduction Zone. *Geophysical Research Letters*, *24*(21), 2601–2604. doi:10.1029/97GL52691

Prawirodirdjo, L., McCaffrey, R., Chadwell, C. D., Bock, Y., & Subarya, C. (2010). Geodetic observations of an earthquake cycle at the Sumatra subduction zone: Role of interseismic strain segmentation. *Journal of Geophysical Research: Solid Earth*, *115*(B3). doi:10.1029/2008JB006139

Qiu, Q., Moore, J. D. P., Barbot, S., Feng, L., & Hill, E. M. (2018). Transient rheology of the Sumatran mantle wedge revealed by a decade of great earthquakes. *Nature Communications*, *9*(1), 995. doi:10.1038/s41467-018-03298-6

Ramos, V. A. (1988). Late Proterozoic-Early Paleozoic of South America -a Collisional History. *Episodes Journal of International Geoscience*, *11*(3), 168–174. doi:10.18814/epiiugs/1988/v11i3/003

Ramos, V. A. (1999). Plate tectonic setting of the Andean Cordillera. *Episodes Journal of International Geoscience*, *22*(3), 183–190. doi:10.18814/epiiugs/1999/v22i3/005

Ranalli, G. (1995). *Rheology of the earth*. London; New York: Chapman & Hall.

Rivas, C., Ortiz, G., Alvarado, P., Podesta, M., & Martin, A. (2019). Modern crustal seismicity in the northern Andean Precordillera, Argentina. *Tectonophysics*, *762*, 144–158. doi:10.1016/j.tecto.2019.04.019

Ruegg, J. C., Rudloff, A., Vigny, C., Madariaga, R., de Chabalier, J. B., Campos, J., Kausel, E., Barrientos, S., & Dimitrov, D. (2009). Interseismic strain accumulation measured by GPS in the seismic gap between Constitución and Concepción in Chile. *Physics of the Earth and Planetary Interiors*, *175*(1), 78–85. doi:10.1016/j.pepi.2008.02.015

Sagiya, T., Miyazaki, S., & Tada, T. (2000a). Continuous GPS Array and Present-day Crustal Deformation of Japan, (157), 2303–2322.

Sagiya, T., Miyazaki, S., & Tada, T. (2000b). Continuous GPS Array and Present-day Crustal Deformation of Japan. *Pure and Applied Geophysics*, *157*(11), 2303–2322. doi:10.1007/PL00022507

Satake, K. (1986). Re-examination of the 1940 Shakotan-oki earthquake and the fault parameters of the earthquakes along the eastern margin of the Japan Sea. *Physics of the Earth and Planetary Interiors*, *43*(2), 137–147. doi:10.1016/0031-9201(86)90081-6

Satake, K. (2015). Geological and historical evidence of irregular recurrent earthquakes in Japan. *Philosophical Transactions of the Royal Society A: Mathematical, Physical and Engineering Sciences*, *373*(2053), 20140375. doi:10.1098/rsta.2014.0375

Sato, T., Kosuga, M., & Tanaka, K. (1986). AFTERSHOCK DISTRIBUTION OF THE 1983 NIHONKAI-CHUBU (JAPAN SEA) EARTHQUAKE DETERMINED FROM RELOCATED HYPOCENTERS. *Journal of Physics of the Earth*, *34*(3), 203–223. doi:10.4294/jpe1952.34.203

Savage, J. C. (1983). A dislocation model of strain accumulation and release at a subduction zone. *Journal of Geophysical Research: Solid Earth*, *88*(B6), 4984–4996. doi:10.1029/JB088iB06p04984

Scholz, C. H. (1998). Earthquakes and friction laws. *Nature*, *391*(6662), 37–42. doi:10.1038/34097

Sébrier, M., Mercier, J. L., Macharé, J., Bonnot, D., Cabrera, J., & Blanc, J. L. (1988). The state of stress in an overriding plate situated above a flat slab: The Andes of central Peru. *Tectonics*, *7*(4), 895–928. doi:10.1029/TC007i004p00895

Seemüller, W., Sánchez, L., Seitz, M., & Drewes, H. (2010a). The position and velocity solution SIR10P01 of the IGS Regional Network Associate Analysis Centre for SIRGAS (IGS RNAAC SIR). DGFI, Munich. Retrieved from http://www.sirgas.org/fileadmin/docs/SIR10P01_DGFI_Report_86.pdf

Seemüller, W., Sánchez, L., Seitz, M., & Drewes, H. (2010b). The position and velocity solution SIR10P01 of the IGS Regional Network Associate Analysis Centre for SIRGAS (IGS RNAAC SIR). Retrieved from http://www.sirgas.org/fileadmin/docs/SIR10P01_DGFI_Report_86.pdf

Seno, T., Sakurai, T., & Stein, S. (1996). Can the Okhotsk Plate be discriminated from the North American plate? *Journal of Geophysical Research: Solid Earth*, *101*(B5), 11305–11315. doi:10.1029/96JB00532

Shestakov, N. V., Gerasimenko, M. D., Takahashi, H., Kasahara, M., Bormotov, V. A., Bykov, V. G., Kolomiets, A. G., Gerasimov, G. N., Vasilenko, N. F., Prytkov, A. S., Timofeev, V. Yu., Ardyukov, D. G., & Kato, T. (2011a). Present tectonics of the southeast of Russia as seen from GPS observations: Present tectonics of the southeast of Russia. *Geophysical Journal International*, *184*(2), 529–540. doi:10.1111/j.1365-246X.2010.04871.x

Shestakov, N. V., Gerasimenko, M. D., Takahashi, H., Kasahara, M., Bormotov, V. A., Bykov, V. G., Kolomiets, A. G., Gerasimov, G. N., Vasilenko, N. F., Prytkov, A. S., Timofeev, V. Yu., Ardyukov, D. G., & Kato, T. (2011b). Present tectonics of the southeast of Russia as seen from GPS observations: Present tectonics of the southeast of Russia. *Geophysical Journal International*, *184*(2), 529–540. doi:10.1111/j.1365-246X.2010.04871.x

Shi, F., Li, S., & Moreno, M. (2020). Megathrust Locking and Viscous Mantle Flow Induce Continental Shortening in Central Andes. *Pure and Applied Geophysics*, *177*(6), 2841–2852. doi:10.1007/s00024-019-02403-0

Shi, X., Kirby, J., Yu, C., Jiménez-Díaz, A., & Zhao, J. (2017). Spatial variations in the effective elastic thickness of the lithosphere in Southeast Asia. *Gondwana Research*, *42*, 49–62. doi:10.1016/j.gr.2016.10.005

Sibson, R. (1981). A brief description of natural neighbour interpolation. *Interpreting Multivariate Data*. Retrieved from https://ci.nii.ac.jp/naid/10022185042/

Simons, M., Minson, S. E., Sladen, A., Ortega, F., Jiang, J., Owen, S. E., Meng, L., Ampuero, J.-P., Wei, S., Chu, R., Helmberger, D. V., Kanamori, H., Hetland, E., Moore, A. W., &

Webb, F. H. (2011). The 2011 Magnitude 9.0 Tohoku-Oki Earthquake: Mosaicking the Megathrust from Seconds to Centuries. *Science*, *332*(6036), 1421–1425. doi:10.1126/science.1206731

Simons, W. J. F., Socquet, A., Vigny, C., Ambrosius, B. a. C., Abu, S. H., Promthong, C., Subarya, C., Sarsito, D. A., Matheussen, S., Morgan, P., & Spakman, W. (2007). A decade of GPS in Southeast Asia: Resolving Sundaland motion and boundaries. *Journal of Geophysical Research: Solid Earth*, *112*(B6). doi:https://doi.org/10.1029/2005JB003868

Sladen, A., & Trevisan, J. (2018). Shallow megathrust earthquake ruptures betrayed by their outer-trench aftershocks signature. *Earth and Planetary Science Letters*, *483*, 105–113. doi:10.1016/j.epsl.2017.12.006

Stewart, J., & Watts, A. B. (1997). Gravity anomalies and spatial variations of flexural rigidity at mountain ranges. *Journal of Geophysical Research: Solid Earth*, *102*(B3), 5327–5352. doi:10.1029/96JB03664

Styron, R., & Pagani, M. (2020). The GEM Global Active Faults Database. *Earthquake Spectra*, *36*(1_suppl), 160–180. doi:10.1177/8755293020944182

Sun, T., Wang, K., Iinuma, T., Hino, R., He, J., Fujimoto, H., Kido, M., Osada, Y., Miura, S., Ohta, Y., & Hu, Y. (2014). Prevalence of viscoelastic relaxation after the 2011 Tohoku-oki earthquake. *Nature*, *514*(7520), 84–87. doi:10.1038/nature13778

Suwa, Y., Miura, S., Hasegawa, A., Sato, T., & Tachibana, K. (2006). Interplate coupling beneath NE Japan inferred from three-dimensional displacement field. *Journal of Geophysical Research: Solid Earth*, *111*(B4). doi:10.1029/2004JB003203

Tanaka, A., Yamano, M., Yano, Y., & Sasada, M. (2004). Geothermal gradient and heat flow data in and around Japan (I): Appraisal of heat flow from geothermal gradient data. *Earth, Planets and Space*, *56*(12), 1191–1194. doi:10.1186/BF03353339

Tanioka, Y., Satake, K., & Ruff, L. (1995). Total analysis of the 1993 Hokkaido Nansei-Oki Earthquake using seismic wave, tsunami, and geodetic data. *Geophysical Research Letters*, *22*(1), 9–12. doi:https://doi.org/10.1029/94GL02787

Tatsumi, Y., Otofuji, Y.-I., Matsuda, T., & Nohda, S. (1989). Opening of the Sea of Japan back-arc basin by asthenospheric injection. *Tectonophysics*, *166*(4), 317–329. doi:10.1016/0040-1951(89)90283-7

Tichelaar, B. W., & Ruff, L. J. (1993). Depth of seismic coupling along subduction zones. *Journal of Geophysical Research: Solid Earth*, *98*(B2), 2017–2037. doi:10.1029/92JB02045

Tong, X., Sandwell, D., Luttrell, K., Brooks, B., Bevis, M., Shimada, M., Foster, J., Smalley Jr., R., Parra, H., Báez Soto, J. C., Blanco, M., Kendrick, E., Genrich, J., & Caccamise II, D. J. (2010). The 2010 Maule, Chile earthquake: Downdip rupture limit revealed by space geodesy. *Geophysical Research Letters*, *37*(24). doi:10.1029/2010GL045805

Trubienko, O., Fleitout, L., Garaud, J.-D., & Vigny, C. (2013). Interpretation of interseismic deformations and the seismic cycle associated with large subduction earthquakes. *Tectonophysics*, *589*, 126–141. doi:10.1016/j.tecto.2012.12.027

Ueda, H., Ohtake, M., & Sato, H. (2003). Postseismic crustal deformation following the 1993 Hokkaido Nansei-oki earthquake, northern Japan: Evidence for a low-viscosity zone in the uppermost mantle: POSTSEISMIC CRUSTAL DEFORMATION. *Journal of Geophysical Research: Solid Earth*, *108*(B3). doi:10.1029/2002JB002067

Van Veen, B. A. D., Vatvani, D., & Zijl, F. (2014). Tsunami flood modelling for Aceh & west Sumatra and its application for an early warning system. *Continental Shelf Research*, *79*, 46–53. doi:10.1016/j.csr.2012.08.020

Veloza, G., Styron, R., Taylor, M., & Mora, A. (2012). Open-source archive of active faults for northwest South America. *GSA Today*, *22*(10), 4–10. doi:10.1130/GSAT-G156A.1

Verfürth, R. (1994). A posteriori error estimation and adaptive mesh-refinement techniques. *Journal of Computational and Applied Mathematics*, *50*(1), 67–83. doi:10.1016/0377-0427(94)90290-9

Vigny, C., Simons, W. J. F., Abu, S., Bamphenyu, R., Satirapod, C., Choosakul, N., Subarya, C., Socquet, A., Omar, K., Abidin, H. Z., & Ambrosius, B. a. C. (2005). Insight into the 2004 Sumatra–Andaman earthquake from GPS measurements in southeast Asia. *Nature*, *436*(7048), 201–206. doi:10.1038/nature03937

Vigny, C., Socquet, A., Peyrat, S., Ruegg, J.-C., Métois, M., Madariaga, R., Morvan, S., Lancieri, M., Lacassin, R., Campos, J., Carrizo, D., Bejar-Pizarro, M., Barrientos, S., Armijo, R., Aranda, C., Valderas-Bermejo, M.-C., Ortega, I., Bondoux, F., Baize, S., Lyon-Caen, H., Pavez, A., Vilotte, J. P., Bevis, M., Brooks, B., Smalley, R., Parra, H., Baez, J.-C., Blanco, M., Cimbaro, S., & Kendrick, E. (2011). The 2010 Mw 8.8 Maule Megathrust Earthquake of Central Chile, Monitored by GPS. *Science*, *332*(6036), 1417–1421. doi:10.1126/science.1204132

Villegas-Lanza, J. C., Chlieh, M., Cavalié, O., Tavera, H., Baby, P., Chire-Chira, J., & Nocquet, J.-M. (2016). Active tectonics of Peru: Heterogeneous interseismic coupling along the Nazca megathrust, rigid motion of the Peruvian Sliver, and Subandean shortening accommodation. *Journal of Geophysical Research: Solid Earth*, *121*(10), 7371–7394. doi:10.1002/2016JB013080

Wackernagel, H. (2003). Ordinary Kriging. In H. Wackernagel (Ed.), *Multivariate Geostatistics: An Introduction with Applications* (pp. 79–88). Berlin, Heidelberg: Springer. doi:10.1007/978-3-662-05294-5_11

Wada, I., & Wang, K. (2009). Common depth of slab-mantle decoupling: Reconciling diversity and uniformity of subduction zones. *Geochemistry, Geophysics, Geosystems*, *10*(10). doi:10.1029/2009GC002570

Wang, K., Hu, Y., Bevis, M., Kendrick, E., Smalley, R., Vargas, R. B., & Lauría, E. (2007). Crustal motion in the zone of the 1960 Chile earthquake: Detangling earthquake-cycle deformation and forearc-sliver translation: CHILE EARTHQUAKE CRUSTAL MOTION. *Geochemistry, Geophysics, Geosystems*, *8*(10). doi:10.1029/2007GC001721

Wang, K., Hu, Y., & He, J. (2012). Deformation cycles of subduction earthquakes in a viscoelastic Earth. *Nature*, *484*(7394), 327–332. doi:10.1038/nature11032

Wang, K., Zhu, Y., Nissen, E., & Shen, Z.-K. (2021). On the Relevance of Geodetic Deformation Rates to Earthquake Potential. *Geophysical Research Letters*, *48*(11), e2021GL093231. doi:10.1029/2021GL093231

Wang, M., Li, Q., Wang, F., Zhang, R., Wang, Y., Shi, H., Zhang, P., & Shen, Z. (2011). Far-field coseismic displacements associated with the 2011 Tohoku-oki earthquake in Japan observed by Global Positioning System. *Chinese Science Bulletin*, *56*(23), 2419–2424. doi:10.1007/s11434-011-4588-7

Wang, Z., & Zhao, D. (2005). Seismic imaging of the entire arc of Tohoku and Hokkaido in Japan using P-wave, S-wave and sP depth-phase data. *Physics of the Earth and Planetary Interiors*, *152*(3), 144–162. doi:10.1016/j.pepi.2005.06.010

Watts, A. B. (2015). 6.01 - Crustal and Lithosphere Dynamics: An Introduction and Overview. In G. Schubert (Ed.), *Treatise on Geophysics (Second Edition)* (pp. 1–44). Oxford: Elsevier. doi:10.1016/B978-0-444-53802-4.00110-X

Watts, A. B., Lamb, S. H., Fairhead, J. D., & Dewey, J. F. (1995). Lithospheric flexure and bending of the Central Andes. *Earth and Planetary Science Letters*, *134*(1), 9–21. doi:10.1016/0012-821X(95)00095-T

Weaver, R., Roberts, A. P., Flecker, R., Macdonald, D. I. M., & Fot'yanova, L. M. (2003). Geodynamic implications of paleomagnetic data from Tertiary sediments in Sakhalin, Russia (NW Pacific). *Journal of Geophysical Research: Solid Earth*, *108*(B2). doi:10.1029/2001JB001226

Weiss, J. R., Brooks, B. A., Foster, J. H., Bevis, M., Echalar, A., Caccamise, D., Heck, J., Kendrick, E., Ahlgren, K., Raleigh, D., Smalley, R., & Vergani, G. (2016). Isolating active orogenic wedge deformation in the southern Subandes of Bolivia. *Journal of Geophysical Research: Solid Earth*, *121*(8), 6192–6218. doi:https://doi.org/10.1002/2016JB013145

Wessel, P., Luis, J. F., Uieda, L., Scharroo, R., Wobbe, F., Smith, W. H. F., & Tian, D. (2019). The Generic Mapping Tools Version 6. *Geochemistry, Geophysics, Geosystems*, *20*(11), 5556–5564. doi:10.1029/2019GC008515

White, S. M., Trenkamp, R., & Kellogg, J. N. (2003). Recent crustal deformation and the earthquake cycle along the Ecuador–Colombia subduction zone. *Earth and Planetary Science Letters*, *216*(3), 231–242. doi:10.1016/S0012-821X(03)00535-1

Williams, T. B., Kelsey, H. M., & Freymueller, J. T. (2006). GPS-derived strain in northwestern California: Termination of the San Andreas fault system and convergence of the Sierra Nevada–Great Valley block contribute to southern Cascadia forearc contraction. *Tectonophysics*, *413*(3), 171–184. doi:10.1016/j.tecto.2005.10.047

Wimpenny, S., Copley, A., Benavente, C., & Aguirre, E. (2018). Extension and Dynamics of the Andes Inferred From the 2016 Parina (Huarichancara) Earthquake. *Journal of Geophysical Research: Solid Earth*, *123*(9), 8198–8228. doi:10.1029/2018JB015588

Yamagiwa, S., Miyazaki, S., Hirahara, K., & Fukahata, Y. (2015). Afterslip and viscoelastic relaxation following the 2011 Tohoku-oki earthquake (M_w 9.0) inferred from inland GPS and seafloor GPS/Acoustic data. *Geophysical Research Letters*, *42*(1), 66–73. doi:10.1002/2014GL061735

Yoshioka, S. (2013). Interplate coupling along the Nankai Trough, southwest Japan, inferred from inversion analyses of GPS data: Effects of subducting plate geometry and spacing of hypothetical ocean-bottom GPS stations, 10.

Yoshioka, S., & Matsuoka, Y. (2013). Interplate coupling along the Nankai Trough, southwest Japan, inferred from inversion analyses of GPS data: Effects of subducting plate geometry and spacing of hypothetical ocean-bottom GPS stations. *Tectonophysics*, *600*, 165–174. doi:10.1016/j.tecto.2013.01.023

Zhu, Y., Wang, K., & He, J. (2020). Effects of Earthquake Recurrence on Localization of Interseismic Deformation Around Locked Strike-Slip Faults. *Journal of Geophysical Research: Solid Earth*, *125*(8). doi:10.1029/2020JB019817